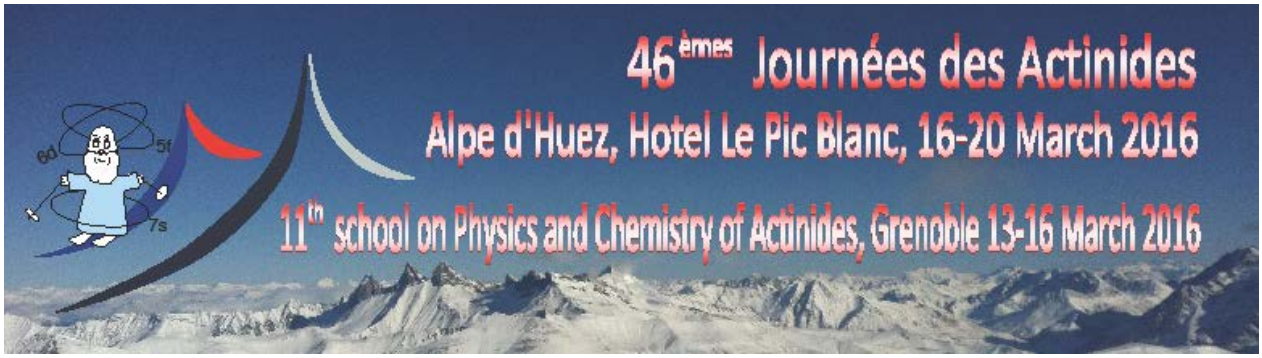

11th School on the Physics and Chemistry of the Actinides (11th SPCA)

13-16 March 2016 - EPN Campus, Grenoble, France

46èmes Journées des Actinides (46th JdA)

16-20 March 2016 - Hotel Pic Blanc, Alpe d'Huez, France

SPCA & JdA Programmes

JdA Oral and Poster Abstracts

List of Participants

Website:http://www.jda2016.org/index.php Info: jda2016@esrf.fr

Thanks to ILL and ESRF for supporting the 11th SPCA!!!

EPN SCIENCE CAMPUS – 71 AVENUE DES MARTYRS – 38000 GRENOBLE

1 **SHUTTLE FROM LYON AIRPORT**
SHUTTLE FROM & TO GENEVA AIRPORT

2 **SHUTTLE TO LYON AIRPORT**

3 **TRAM B – Stop « Presqu'île »**
From Grenoble (direction « Presqu'île »)
To Grenoble (direction « Plaine des sports »)

Contents

11th School on the Physics and Chemistry of the Actinides (11th SPCA)

46èmes Journées des Actinides (46th JdA):

11th School on the Physics and Chemistry of the Actinides (11th SPCA)

11th School on the Physics and Chemistry of the Actinides (13 - 16 March)
EPN Campus, Grenoble

Dear Actinide Researcher,

Welcome to the 11th School on the Physics and Chemistry of the Actinides. The school (SPCA) will take place on the European Photon and Neutron (EPN) Science Campus, which hosts two of the largest User Facilities in Europe, as well as the European Molecular Biology Laboratory (EMBL) and the Institut de Biologie Structurale (IBS), and is a short tram ride from the Grenoble train station. The SPCA is organised every second year so that graduate students can attend at least one school during their graduate years.

The *Institut Laue-Langevin* (ILL) runs the world's most productive neutron source based on a 60 MW reactor, with nearly 40 different instruments dedicated to experiments and a budget of ~ €80 M/year. About 1500/year scientists visit the ILL to perform experiments. Interestingly, the ILL started to operate in 1972, the year of the 1ère Journée des Actinides in the same place, Grenoble, and less than a kilometer away at the CEN-G (as it was then called) site.

The *European Synchrotron Radiation Facility* (ESRF) is the world's most intense source of synchrotron-generated light. More than 40 beamlines of bright X-ray light are used by more than 6000 scientists/year. The budget is ~ €100 M/year. The first experiments were done in 1994.

Both these facilities carry out many experiments in actinide science, chemistry, physics, and materials science. The major object of the school will be to give those attending an idea of the types of experiments that can be performed at these sources. There will be organized visits to both facilities.

Thanks to the ILL and ESRF for providing financial and secretarial assistance.

The programme for the school is on the next two pages.

ESRF

NEUTRONS FOR SCIENCE

11th School on the Physics and Chemistry of the Actinides

Venue: ILL Chadwick Amphitheatre, EPN Campus

PROGRAMME

Sunday 13 March 2016		
18:30 - 21:30	*Registration and Welcome Buffet at the ESRF/ILL cafeteria*	

Monday 14 March 2016		
08:00 - 08:15	Registration continues	
08:15 - 08:30	Welcome by W. G. Stirling, ILL	
08:30 - 10:00	Introduction I - Scattering with neutrons and X-rays	**L. Paolasini** ESRF & Grenoble University
10:00 - 10:30	*Coffee break*	
10:30 - 12:00	Introduction II - Absorption processes and spectroscopies with X-rays	**A. Rogalev & F. Wilhelm** ESRF
12:00 - 13:15	*Lunch at the ESRF/ILL onsite restaurant*	
13:15 - 15:00	**Tour (½ to ILL and ½ to ESRF)**	
15:00 - 16:00	High-energy resolution X-ray absorption and emission spectroscopy	**K. Kvashnina** ROBL & HZDR
16:00 - 16:30	*Tea break*	
16:30 - 17:30	Neutrons in soft matter	**G. Fragneto** ILL
17:30 - 18:30	Neutron inelastic scattering from single crystals	**A. Hiess** European Spallation Source
19:00 - 20:30	*Dinner onsite*	

Tuesday 15 March 2016		
08:30 - 09:30	Thermodynamic and transport measurements in conjunction with large instruments	**D. Braithwaite** CEA Grenoble
09:30 - 10:30	Neutron powder diffraction and PDF-analysis	**H. Fischer** ILL
10:30 - 11:00	*Coffee break*	
11:00 - 12:00	Application of EXAFS spectroscopy to actinide research	**A. Scheinost** ROBL & HZDR
12:00 - 13:15	*Lunch at the ESRF/ILL onsite restaurant*	
13:15 - 15:00	**Tour (½ to ILL and ½ to ESRF)**	
15:00 - 16:00	High-pressure experiments at ESRF	**G. Garbarino** ESRF
16:00 - 16:30	*Tea break*	
16:30 - 17:30	Materials science measurements with X-rays and neutrons	**T. Buslaps** ESRF
17:30 - 18:30	Neutron inelastic scattering at spallation sources	**G. Lander** ITU & ILL
19:00 - 21:30	*Wine & Cheese Party at the ESRF/ILL cafeteria*	

Wednesday 16 March 2016		
09:00 - 10:00	Studies of thin films of actinides at synchrotrons	**R. Springell** Bristol University
10:00 - 11:00	Application of small-angle X-ray scattering to actinide research	**S. Shaw** Manchester University
11:00 - 11:30	*Coffee break*	
11:30 - 12:30	The physics of actinide dioxides: 50 years of neutrons and X-rays	**R. Caciuffo** JRC-ITU
12:30 - 13:30	*Lunch at the ESRF/ILL onsite restaurant*	
14:00 - 16:30	**Bus from EPN Campus to 46th JdA at Alpe d'Huez**	

46èmes Journées des Actinides
(46th JdA)

46èmes Journées des Actinides (16 - 20 March)
Hotel Pic Blanc, Alpe d'Huez

Welcome to the 46èmes Journées des Actinides (46th JdA). Alpe d'Huez is one of the most famous winter resorts in the French Alps, and with its altitude extending to 3000 m, so you can be guaranteed snow - at least up high. Alpe d'Huez is also a prominent fixture of the Tour de France bicycle race, and you will see that the 21 hairpin bends on the way up to the ski station are named for famous winners of the Tour. Biking up to Alpe d'Huez is not part our plan!

The first meeting of the JdA was in 1972 in Grenoble, and a further meeting, the 22nd in 1992, took place at another ski resort close to Grenoble, Meribel. So we seem to have fixed a frequency of ~ 23 years for the JdA near Grenoble, implying the next one will be in ~ 2039. The present local Committee will have retired by then!

The five previous meetings were: 2015 - Pruhonice, near Prague (Czech Republic); 2014 - Ein Gedi (Israel); 2013 - Sestri-Levant (Italy); 2012 - Bristol (UK); 2011 - Stara Lesna (Slovakia).

This conference is a traditional forum for informal discussion encompassing numerous different aspects related to the chemistry and physics of the actinides. It regularly brings together experts from all the fields involved, emphasizing exchanges and lively discussions on current issues in actinide science and stimulating new collaborative projects. Moreover, a strong emphasis is given on presentations of on-going research projects by young scientists and PhD students.

We have 42 oral talks at this JdA, and about 20 posters (the poster session starts at 18 hrs on Friday evening), so that the programme is full. In addition, on Saturday just before lunch we have a "Summary and Perspective" session lasting one hour, where we have asked 4 senior scientists to give their impressions of the Conference.

The programme and short abstracts follow. You can find the list of long abstracts (after the login) on the web:http://jda2016.org/index.php/abstract/list-long-abstracts. However, since the long abstracts could be posted anytime up to the Conference this list may not be complete. Please consult the website.

The Hotel Le Pic Blanc in Alpe d'Huez is a newly renovated 4* hotel. Participants will be lodged in the same hotel, and the registration fee covers *lunch, dinners, coffee breaks etc*, at the hotel.

The Conference Banquet, held at the Restaurant Chantebise at 2100 meters, is on Saturday evening 19th March and is covered in the registration fee. Transport to (and back from!) the restaurant will be by snowcat, so it is important to be *on time* for the departure - otherwise it is a long walk!

There will be no session on Sunday 20th March - this is the day of departure.

At the moment there are two afternoons free, Friday and Saturday, to enjoy the surroundings (there are many other things to do in addition to skiing!). If the weather suggests we should be outside at another time, the schedule may be changed, so please be attentive for announcements!

International Advisory Committee

Jean Aupiais (Arpajon, France)

Eric Colineau (Karlsruhe, Germany)

Nicolas Dacheux (Montpellier, France)

David Geeson (Reading, UK)

Antonio Pereira Gonçalves (Sacavém, Portugal)

Ladislav Havela (Prague, Czech Republic)

Itzhak Halevy (Be'er Sheva, Israel)

Dariusz Kaczorowski (Wroclaw, Poland)

Local Organizing Committee

Kristina Kvashnina (ESRF CRG ROBL, France)

Gerry Lander, co-chairman (ILL, France)

Luigi Paolasini (ESRF, France)

Andrei Rogalev (ESRF, France)

Claudine Roméro (ESRF, France)

André Rossberg (ESRF CRG ROBL, France)

Andreas Scheinost (ESRF CRG ROBL, France)

Stepan Sechovsky (Charles University, Czech Republic)

Laurence Tellier (ILL, France)

Fabrice Wilhelm, co-chairman (ESRF, France)

Programme

46èmes Journées des Actinides

Venue: Hotel Pic Blanc, Alpe d'Huez

PROGRAMME

Wednesday 16 March 2016	
18:00 - 22:00	*Registration and Welcome Reception*

Thursday 17 March 2016		
A - Condensed Matter & Electronic Structure (Chair: R. Caciuffo)		
08:30 - 08:50	Welcome	
08:50 - 09:10	**A1** - Role of atomic multiplets in intermediate valence PuB_6	**A. B. Shick** Czech Republic
09:10 - 09:30	**A2** - New binary uranium and thorium platinides with the Pu_3Pd_4 structure type	**N. Brisset** France
09:30 - 09:50	**A3** - Spin-fluctuation effects near the quantum phase transition of the itinerant ising-type ferromagnet URhAl	**D. Braithwaite** France
09:50 - 10:10	**A4** - How to recognize a dual character of 5*f* electrons in some uranium systems from electronic structure data	**M. Samsel-Czekala** Poland
10:10 - 10:30	**A5** - Complex magnetic behavior in single-crystalline $UCuBi_2$	**D. Kaczorowski** Poland
10:30 - 11:00	*Coffee break*	
B - Actinide Handling & Materials Science (Chair: E. Colineau)		
11:00 - 11:20	**B1** - Computational investigations of SANEX ligand selectivity	**I. Fryer-Kanssen** UK
11:20 - 11:40	**B2** - First-principles molecular dynamics study of water dissociation on the γ-U(100) surface	**Y. Yang** China
11:40 - 12:00	**B3** - Physical properties of a new $U_3Fe_{3-y}Sb_4$ system	**M. Reiffers** Slovakia
12:00 - 12:20	**B4** - Multi-step excitation schemes in laser spectroscopy and detection of actinides and lanthanides in solutions	**I. Izosimov** Russia

12:20 - 12:40	**B5** - Laser remote analysis for MOX fuel and its application for rapid and in-situ analysis in decommissioning of "Fukushima Daiich" nuclear power station	**I. Wakaida** Japan
12:40 - 13:00	**B6** - Thermal expansion and thermodynamical properties of Ce-based compounds $CeCuAl_3$, $CePt_3Si$, and $CePt_3B$ theory and experiment	**D. Legut** Czech Republic
13:00 - 14:30	*Lunch*	
C - Electronic Structure & Physical Properties (Chair: I. Halevy)		
14:30 - 14:50	**C1** - First-principles studies on the charge density wave in uranium	**R. Qiu** China
14:50 - 15:10	**C2** - The valence-fluctuating ground state of plutonium	**G. H. Lander** Germany
15:10 - 15:30	**C3** - Structure and magnetism of uranium hydrides	**L. Havela** Czech Republic
15:30 - 15:50	**C4** - The interaction between hydrogen and uranium thin films studied by synchrotron X-ray radiation	**J. E. Darnbrough** UK
15:50 - 16:10	**C5** - Electronic structure of U-Si binary intermetallic compounds by hybrid functional calculations	**X. Wang** China
16:10 - 16:30	**C6** - Dynamic magnetic response across the pressure-induced structural phase transition in CeNi	**A. Mirmelstein** Russia
16:30 - 17:00	*Tea break*	
D - Superconductivity (Chair: L. Havela)		
17:00 - 17:20	**D1** - Upper critical field and pairing mechanism in the ferromagnetic superconductor UCoGe	**J.-P. Brison** France
17:20 - 17:40	**D2** - Post-transition metal, metalloid and isotopic doping in $PuCoGa_5$	**E. Colineau** Germany
17:40 - 18:00	**D3** - Thermal expansion of the heavy-fermion superconductor $PuCoGa_5$	**R. Eloirdi** Germany
18:00 - 18:20	**D4** - X-ray circular magnetic dichroism of the superconductor $PuCoGa_5$	**F. Wilhelm** France
19:00 - 20:30	*Dinner*	

Friday 18 March 2016

E - Novel Methods for Actinide Materials (Chair: D. Geeson)		
08:30 - 08:50	**E1** - A new approach for radiation damage studies by incorporation of dilute self-irradiating defects in thin films	**E. Yahel** Israel
08:50 - 09:10	**E2** - Using diffraction tomography to chemically characterise and spatially locate the corrosion products of uranium metal encapsulated in cement grout under different storage conditions	**N. Harker** UK
09:10 - 09:30	**E3** - Purification of uranium hexafluoride by magnesium fluoride	**J.-M. Hiltbrunner** France
09:30 - 09:50	**E4** - Evaluating laser driven x-ray sources for analytical scanning of nuclear waste	**C. P. Jones** UK
09:50 - 10:10	**E5** - A new X-ray emission spectrometer at the Rossendorf beamline for studying nuclear materials	**K. Kvashnina** France
10:10 - 10:30	**E6** - Inelastic X-ray scattering studies of actinides	**A. Walters** UK
10:30 - 11:00	*Coffee break*	
F - Chemistry & Materials Properties (Chair: A. P. Goncalves)		
11:00 - 11:20	**F1** - Uranium sorption on mixtures based on alumina nanoparticles and smectite clay colloids	**N. Mayordomo** Spain
11:20 - 11:40	**F2** - Unraveling the structure and the excited state dynamics of the aqueous cerium(III) ion by combined experimental and theoretical approaches	**F. Réal** France
11:40 - 12:00	**F3** - Sorption of trivalent actinides onto montmorillonite: Macroscopic, thermodynamic and structural evidence for ternary hydroxo and carbonato surface complexes on multiple sorption sites	**M. Marques Fernandes** Switzerland
12:00 - 12:20	**F4** - Structural characterization of Pa(IV) in aqueous solution and quantum chemical investigations of the tetravalent actinides up to Bk(IV): the evidence of a curium break	**V. Vallet** France
12:20 - 12:40	**F5** - The U-Nb-Al phase-diagram : a thermodynamic investigation and some characterizations of the intermediate phases	**O. Tougait** France
13:00 - 14:30	*Lunch*	

14:30 - 18:00	***Social Afternoon***
18:00 - 19:00	**Poster Session with refreshments**
19:00 - 20:30	*Dinner*
20:30 - 21:30	**Poster Session continues**

Saturday 19 March 2016

G - Oxides: Theory & Experiment (Chair: J.-P. Brison)		
08:30 - 08:50	**G1** - Density functional theory studies of actinide oxides	**P. Zhang** China
08:50 - 09:10	**G2** - Crystal dynamics of neptunium dioxide	**L. Paolasini** France
09:10 - 09:30	**G3** - Ab-initio calculation of oxygen self-diffusion coefficient in uranium dioxide UO_2	**B. Dorado** France
09:30 - 09:50	**G4** - Measurements of acoustic phonons in irradiated UO_2 epitaxial films	**S. Rennie** UK
09:50 - 10:10	**G5** - Thermodynamic stability of the UO_2 surfaces: Interplay between over-stoichiometry and polarity compensation	**F. Bottin** France
10:10 - 10:30	**G6** - Trends in rare gases incorporation into uranium dioxide	**H. Lu** China
10:30 - 11:00	*Coffee break*	
H - Oxides: Theory & Experiment (cont.) (Chair: G. H. Lander)		
11:00 - 11:20	**H1** - First-principles DFT+U investigation of actinide oxides including point defects and fission gases	**L. Shi** France
11:20 - 11:40	**H2** - XRD and XAS investigations of $(U,Am)O_2$ compounds with high Am-content	**E. Epifano** France
11:40 - 12:00	**H3** - On the influence of Np incorporation on the redox of UO_2	**M. Chollet** Switzerland

12:00 - 13:00	**<u>Summary & Perspectives</u>** **Oxides: B. Dorado** **Chemistry & Actinide Handling: A.Scheinost** **Materials Science and Physics: A. B. Shick and D. Kaczorowski**
13:00 - 14:30	*Lunch*
14:30 - 18:00	***Social Afternoon***
19:00-22:00	*Conference Dinner at the Altitude Restaurant Le Chantebise 2100*

Oral abstracts

A1

Role of atomic multiplets in intermediate valence PuB_6

A. B. Shick[1], L. Havela[2] , A. I. Lichtenstein[3] , and M. I. Katsnelson[4]

[1]*Institute of Physics, ASCR, Prague, Czech Republic*
[2]*Charles University, Prague, Czech Republic*
[3] *University of Hamburg, Germany*
[4] *Radboud University Nijmegen, The Netherlands*

The electronic structure of PuB_6, an actinide analog of SmB_6 , was investigated making use of a combination of the density functional theory in a local density approximation (LDA), and the exact diagonalization (ED) of an effective discrete Anderson impurity model [1]. Intermediate valence ground state with the f-shell occupation n_{4f}=5.5 for the Pu atom in PuB_6 is calculated. This ground state is a non-magnetic singlet with all angular momenta of the 5f-bath cluster equal to zero. The 5f-shell magnetic moment is completely compensated by the moment carried by the electrons in the conduction band.

Already in DFT, PuB_6 is an insulator with a small amount of holes near the X-point, and the indirect band gap of ~60 meV (see Fig. 1). This band gap becomes direct in DFT+ED calculations supporting the idea of "topological Kondo insulator" in PuB_6.

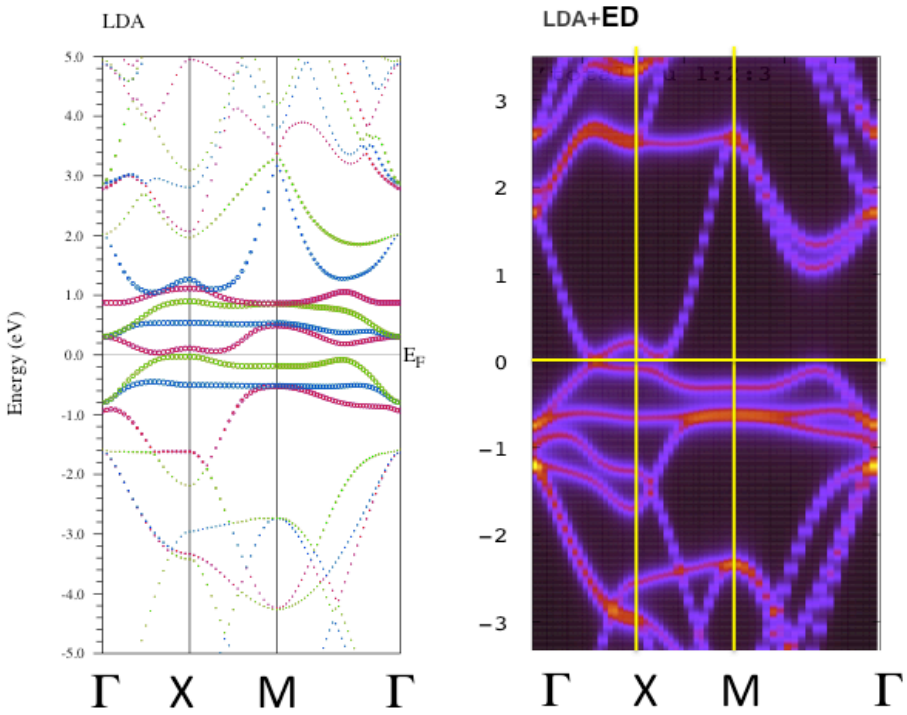

Fig. 1. PuB_6 LDA and LDA+ED band structure.

The f-orbital density of states (fDOS) obtained from LDA+ED for the Pu atom PuB_6 is shown in Fig. 2 in comparison with the fDOS for $PuCoGa_5$.The many-body resonances near the Fermi energy are produced by f^6-to-f^5 multiplet transitions are in a way analogues to the *Racah* peaks, specific transitions between *Racah* multiplets [2] of f^n-to-$f^{n-1,n+1}$. Three peak structure: f^6-to-f^5 multiplet transitions are better resolved than f^5-to-f^4 transitions. This suggests partial delocalization of f^5 multiplet, and illustrates the "dual" nature of the f states in Pu compounds.

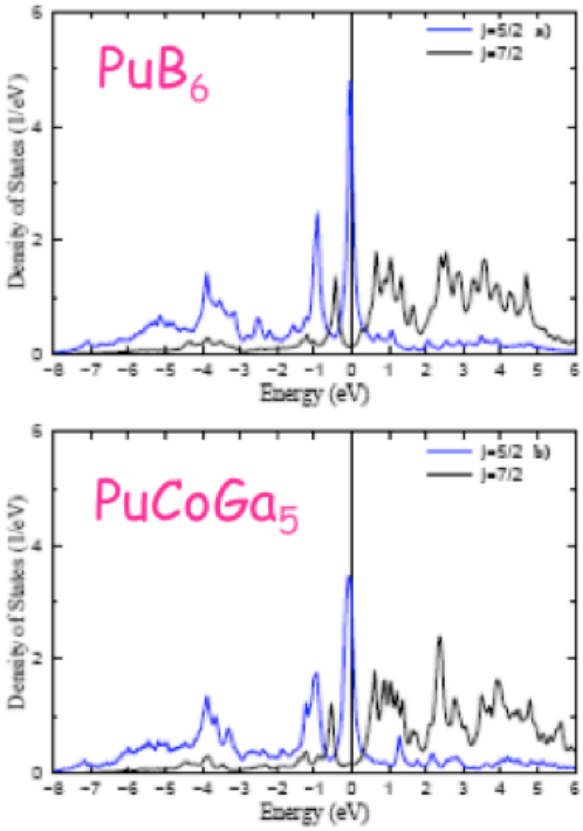

Fig. 2. f-electron density of states (j = 5/2, 7/2 projected) for the Pu atom in PuB_6 and $PuCoGa_5$.

The non-magnetic character of PuB_6 , as well as δ-Pu and $PuCoGa_5$ is associated with the valence fluctuations due to Coulomb interaction between f- and d-states. When there is a mixing of magnetic [f^5] and non-magnetic [f^6] multiplets the resulting state is non-magnetic. Our calculations show that hybridization between f-shell and other non-f electrons plays a role and leads to formation of the multi-orbital Kondo-like singlet ground state.

References

[1] A. B. Shick, L. Havela, A. I. Lichtenstein, M. I. Katsnelson, Scientific Reports 5, 15429 (2015).
[2] G. Racah, Phys. Rev. 76, 1352 (1949)

A2

New binary uranium and thorium platinides with the Pu_3Pd_4 structure type.

N.Brisset[1], G. Chajewski[2], A. Berche[1], A. Novikova[1], V. Dorcet[1], M. Pasturel[1], A.Pikul[2], O. Tougait[3]

[1] *Institut des Sciences Chimiques de Rennes, UMR CNRS 6226, Université Rennes 1, Campus de Beaulieu, 35042 Rennes, France Cedex. email : nicolas.brisset@univ-rennes1.fr*
[2] *Institute of Low Temperature and Structure Research, ul. Okólna 2, 50-422 Wrocław, Poland*
[3] *Unité de Catalyse et de Chimie du Solide, UMR CNRS 8181, Université de Lille, Campus Scientifique, 59655 Villeneuve d'Ascq, France.*

The Pu_3Pd_4 (*1*) structural type (*R-3* space group, n°148) is adopted by numerous binaries of rare earth (40 known compounds with the general formula RE_3T_4, T = Pd (*2*), Pt (*3*), Au (*4-7*), RE = *4f* elements but Pm and Eu) and thorium (Th_3Pd_4 (*2*), Th_3Au_4 (*8*)) . However, former investigations of the U-T (T=Pd, Pt and Au) binary phase diagrams do not show any phase with this structural type. A phase with rough composition "Th_3Pt_4", although hinted in the past (*9*), was never fully characterized. As a part of our reinvestigation of the U-Pt binary system, we tried to obtain the isostructural compound.

Synthesis in the composition range from 50 at.% to 65 at.% Pt lead to the discovery of a new phase in as cast samples. SEM-EDS analyses indicate an U_3Pt_4 stoichiometry while Rietveld refinements performed on powder x-ray diffraction patterns confirm the Pu_3Pd_4 structural type with cell parameters a = 13.237(2) Å and c = 5.680(1) Å (fig. 1). Despite long (one week at 1173 K in sealed silica tubes) or high temperature (6 h at 1723 K in a HF furnace) annealings, we were not able to obtain suitable single crystals for X-ray diffraction (XRD). Additional transmission electron diffraction experiments have thus been performed to confirm the absence of superstructure.

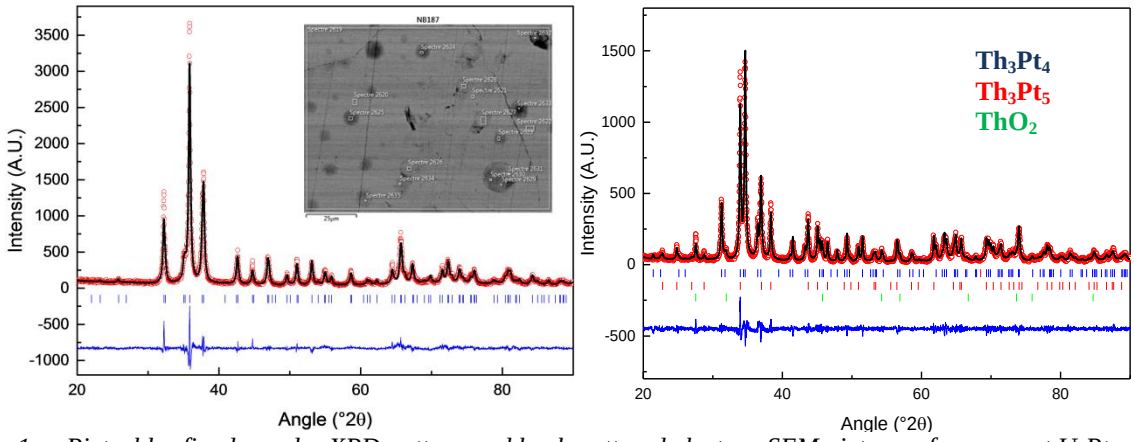

Figure 1 a :Rietveld refined powder XRD pattern and backscattered electron SEM picture of an as-cast U_3Pt_4 sample .b: Full pattern matched powder XRD pattern of an as-cast Th_3Pt_4 sample

Using the same protocol, the previously suspected Th_3Pt_4 phase was also obtained in as cast samples, despite a moderate oxidation inducing the appearance of Th_3Pt_5 and ThO_2 as impurities. From powder XRD, we were able to confirm the Pu_3Pd_4 structure-type and to obtain the cell parameters a = 13.685(6) Å and c = 5. 797(4) Å (fig. 2) for this phase.

Susceptibility measurements (fig 2(a)) performed on U_3Pt_4 show a ferromagnetic ordering below Tc = 8.0(6) K, the poor crystallinity of the samples being probably responsible for the very smooth transition. The high temperature region of $\chi(T)^{-1}$ follows a modified Curie-Weiss law with μ_{eff} = 2.18 μ_B, θ_p = 3.5 K and χ_0 = 1.8*10^{-3} emu mol_U^{-1}. These values are typical of highly delocalized *5f* electron uranium based intermetallics

Specific heat measurements confirmed the Curie temperature for U_3Pt_4 (fig. 2(b)). Removing the phonon contribution of Th_3Pt_4 to U_3Pt_4 allowed to extrapolate the Sommerfeld coefficient $\gamma \approx 240$ mJ mol_U^{-1} K^{-2} from the $Cp/T = f(T^2)$ difference curve. This value is characteristic of a rather enhanced heavy fermion behavior and is in line with the occurrence of strong electronic correlations in this compound responsible for the pronounced delocalization of the *5f* electrons observed by magnetic measurements. No superconductivity was observed down to 2 K on either of these samples.

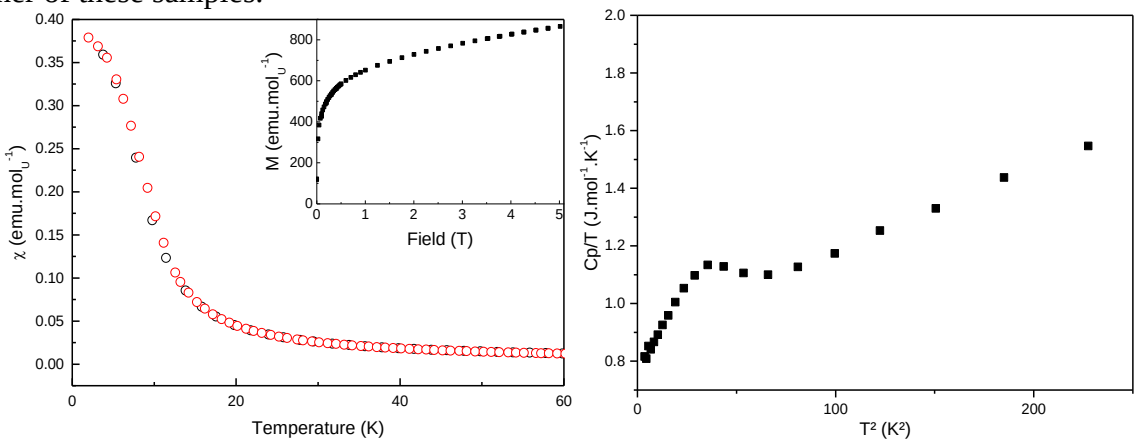

Figure 2 a: Dependence of the magnetic susceptibility versus temperature at 5000 Oe and of the magnetic moment versus field at 2K of an as cast U_3Pt_4 sample .b: dependence of the heat capacity divided by the temperature versus the square of the temperature for the same sample

The chemical, crystallographic, magnetic and specific heat characterizations of these new A_3Pt_4 (A = Th, U) compounds will be presented.

References

1. D. T. Cromer, A. C. Larson, R. B. J. Roof, The crystal structure of Pu3Pd4. *Acta Crystallographica Section B* **29**, 564-567 (1973).
2. A. Palenzona, A. Iandelli, The crystal structure and lattice constants of RE3Pd4, Y3Pd4 and Th3Pd4 compounds. *Journal of the Less Common Metals* **34**, 121-124 (1974).
3. A. Palenzona, The crystal structure and lattice constants of R3Pt4 compounds. *Journal of the Less Common Metals* **53**, 133-136 (1977).
4. A. Saccone, M. L. Fornasini, D. Maccio, S. Delfino, Phase equilibria in the Gd-Au system. *Intermetallics* **4**, 111-119 (1996).
5. A. Saccone, D. Maccio, M. Giovannini, S. Delfino, The praseodymium-gold system. *Journal of Alloys and Compounds* **247**, 134-140 (1997).
6. A. Saccone, D. Maccio, S. Delfino, R. Ferro, The neodymium-gold phase diagram. *Metallurgical and Materials Transactions a-Physical Metallurgy and Materials Science* **30**, 1169-1176 (1999).
7. A. Saccone, D. Maccio, S. Delfino, R. Ferro, The phase diagram of the terbium-gold alloy system. *Intermetallics* **8**, 229-237 (2000).
8. A. Palenzona, S. Cirafici, THE TH-AU PHASE-DIAGRAM. *Journal of the Less-Common Metals* **124**, 245-249 (1986).
9. J. R. Thomson, ALLOYS OF THORIUM WITH CERTAIN TRANSITION METALS .2. THE SYSTEMS THORIUM OSMIUM, THORIUM IRIDIUM AND THORIUM PLATINUM. *Journal of the Less-Common Metals* **6**, 3-10 (1964).
10. A. De Visser, A. Menovsky, J. J. M. Franse, UPt3, heavy fermions and superconductivity. *Physica B+C* **147**, 81-160 (1987).

A3

Spin-Fluctuation Effects near the Quantum Phase Transition of the Itinerant Ising-Type Ferromagnet URhAl

D. Braithwaite, Y. Shimizu, B. Salce, T. Combier, D. Aoki, and J. Flouquet
Univ. Grenoble Alpes and CEA, INAC, F-38000 Grenoble, France

Itinerant ferromagnets often show a first-order transition rather than a quantum critical point (QCP) when the Curie temperature is tuned to low values. An interesting case is UCoAl where the tricritical point occurs at negative pressure, but with the application of magnetic field describes a wing shaped structure which terminates in a quantum critical end point. We focus here on URhAl, which has the same crystal structure and is similar to UCoAl at a negative pressure.

We find the critical pressure Pc ~5.2 GPa. The Curie temperature disappears as a first-order phase transition. However, near Pc, we observed an enhancement of the Fermi-liquid resistivity term, and the resistivity is described rather by a non-Fermi-liquid regime, similar to that expected for a ferromagnetic QCP. The first-order nature of the phase transition is probably weak, and the system is dominated by strong spin-fluctuations. A full theoretical description of ferromagnetic quantum criticality is still lacking.

Email of presenting author: daniel.braithwaite@cea.fr

Long abstract: was not submitted

A4

How to recognize a dual character of 5*f* electrons in some uranium systems from electronic structure data

Małgorzata Samsel-Czekała

Institute of Low Temperature and Structure Research, Polish Academy of Sciences, P.O. Box 1410, 50-950 Wrocław 2, Poland, e-mail: M.Samsel@int.pan.wroc.pl

Generally, it is significant in explaining electronic and physical properties of any actinide compound to consider first of all the nature and role of the An 5*f* electrons. Usually, owing to their complex behavior, in such exemplary uranium systems as UGe_2, UFe_2Al_{10} and UN, that problem even now remains a great challenge. In recent years the *dual* character of the U 5*f* states in the above and other compounds has been proposed. It means that both their localized and itinerant behaviors are treated on equal footing. Therefore, in this presentation, some way of reinterpreting earlier band-structure calculations and photoemission XPS/ARPES data will be discussed.

A5

Complex magnetic behavior in single-crystalline $UCuBi_2$

Dariusz Kaczorowski
Institute of Low Temperature and Structure Research, Polish Academy of Sciences

The novel compound $UCuBi_2$ crystallizes with a primitive tetragonal structure of the ZrCuSiS-type. In contrast to its isostructural counterparts $UCuAs_2$ and $UCuSb_2$, which are ferromagnetic Kondo lattices, the bismuthide orders antiferromagnetically at low temperatures and exhibits fairly intricate magnetic behavior in applied magnetic fields. The thermodynamic and electrical transport properties of $UCuBi_2$ will be discussed in comparison with those of the other $UCuX_2$ (X = P, As, Sb) pnictides as well as a few rare-earth - based $RCuBi_2$ compounds. It will be argued that due to its non-symmorphic symmetry, square network of Bi atoms and intrinsic time-reversal symmetry breaking, $UCuBi_2$ may host Weyl states with a behavior of Dirac fermions distinct from that in graphene and in 3D Dirac semimetals, yet similar to that in the related material $YbMnBi_2$.

Email of presenting author: d.kaczorowski@int.pan.wroc.pl

Long abstract: was not submitted

1

Computational investigations of SANEX ligand selectivity

Izaak Fryer-Kanssen,[1] Dr. Andrew Kerridge[1]

[1] *Lancaster University, Department of Chemistry, LA1 4YW, Bailrigg, Lancaster, United Kingdom, e-mail: i.fryer-kanssen@lancaster.ac.uk*

An important problem in the nuclear power industry is associated with the separation of two radioactive components of spent nuclear fuel. These components are characterised as long-lived minor actinides (Np, Am, Cm) and short-lived lanthanide species (e.g. Gd, Eu). Our work aims to improve our understanding of the basic underlying processes which govern the successful separation of trivalent actinides and lanthanides, such as in the Selective Actinide Extraction (SANEX) process. The chemical bonding in actinide systems is believed to be subtly different to that of their lanthanide counterparts due to the greater spatial extent of the 5f orbitals in the former. This leads to greater covalent character in An-ligand bonds and allows carefully selected ligands (e.g. BTP, BTPhen, Fig. 1) to preferentially bind the An(III) ion [1,2,3].

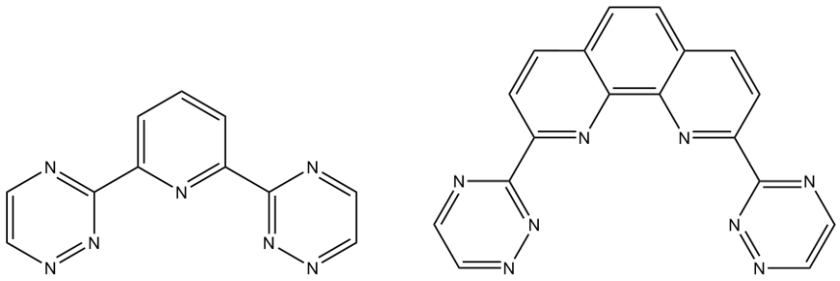

Fig. 1. left: BTP, 2,6-di(1,2,4-triazin-3-yl)pyridine; right: BTPhen, 2,9-bis(1,2,4-triazin-3-yl)-1,10-phenanthroline

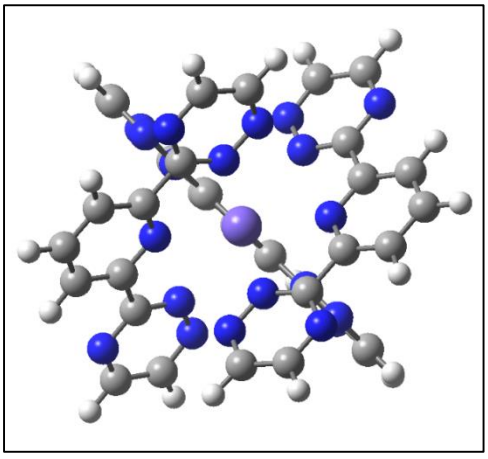

Fig. 2. A sample optimised $[Gd(BTP_3)]^{3+}$ complex

This study focuses on N-donor ligands such as terpyridine, BTP, BTBP and BTPhen, due to their relative softness and adherence to the CHON principle. However, in order to properly investigate the separation process, initial investigations have also concerned the trinitrate Ln/An complexes, as the waste radionuclides are stored in nitric acid. Reaction energies for the formation of the tris-BTP complexes of several Ln and An complexes (Ln = La, Lu, Gd, Eu, An = Cm, Am) from their trinitrates have been calculated, indicating a slight energetic preference for the formation of the An complexes over their Ln analogues.

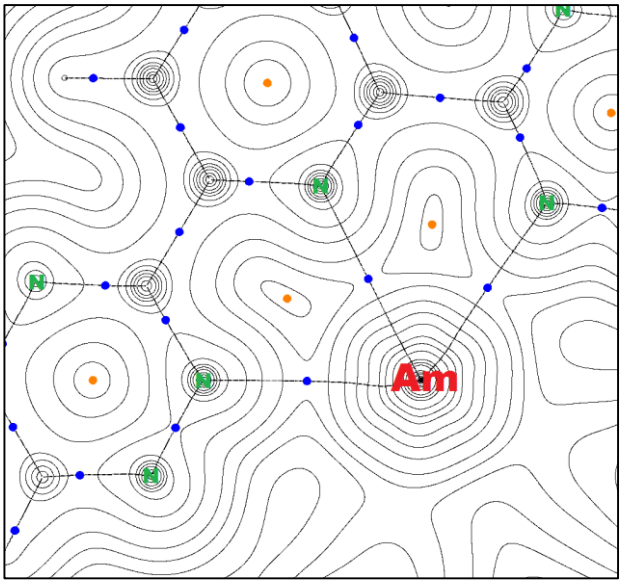

Fig. 3. An example AIM electron density plot for $[Cm(BTP)_3]^{3+}$ generated with MultiWFN

As a complement to this energetic study, the nature of the M-N bonding in the tris-BTP complexes has been investigated using QTAIM (Quantum Theory of Atoms in Molecules) methods. The value of the electron density (ρ) at a bond critical point - where the electron density between atomic basins reaches a minimum (blue dots, Fig. 3) - can be taken as a measure of the covalent character of the bond. A greater electron density (ρ) at the An-L bond critical points and higher delocalisation indexes (δ) in the An complexes may indicate enhanced covalency between the actinide ion and the ligands.

References

[1] W. Verboom, *Chem. Soc. Rev.*, **36**, 367-377 (2007).
[2] L.M. Harwood, *Synlett*, **18**, 2609-2632 (2011).
[3] J.-H Lan, *Coord. Chem. Rev.*, **256**, 1406-1417 (2012).

2

First-principles molecular dynamics study of water dissociation on the γ-U(100) surface

Yu Yang,[1] Ping Zhang[1,2]

[1] *Institute of Applied Physics and Computational Mathematics, PO Box 8009, Beijing 100088, People's Republic of China, e-mail: yang_yu@iapcm.ac.cn*
[2] *Center for Applied Physics and Technology, Peking University, Beijing 100871, People's Republic of China*

By performing systematical first-principles molecular dynamics (FPMD) simulations, we reveal that water molecules dissociate spontaneously when approaching the native γ-U(100) surface. The products of the dissociative adsorption are one hydrogen atom and one hydroxy group. The dissociation is because of the weakening of the two O-H bonds upon adsorption. Once there exists a surface substitutional Nb atom, adsorbing water molecules also dissociate easily around it. It is also found that after water dissociations, the hydrogen atoms move very fast away from the hydroxy group, both on the γ-U(100) and UNb surfaces. This phenomenon is quite similar to the 'Hot-Atom' dissociation of oxygen molecules on the Al(111) surface, where the dissociated oxygen atoms also move away from each other fast. We have also performed consecutive FPMD simulations for 1~4 water molecules adsorbing. It is found that on the γ-U surface, after adsorption of 0.44 ML water molecules, hydrogen atoms start to desorb and form diatomic molecules, while at the same time oxygen atoms begin to penetrate the surface forming U-O-U structures, which can be seen as a start for oxide nucleus formation. Comparatively on the UNb surface, we see no desorption of hydrogen atoms although oxygen atoms also begin to penetrate at the coverage of 0.44 ML water molecules. Instead, hydrogen atoms are more inclined to distribute around the surface Nb atom or around its surrounding U atoms.

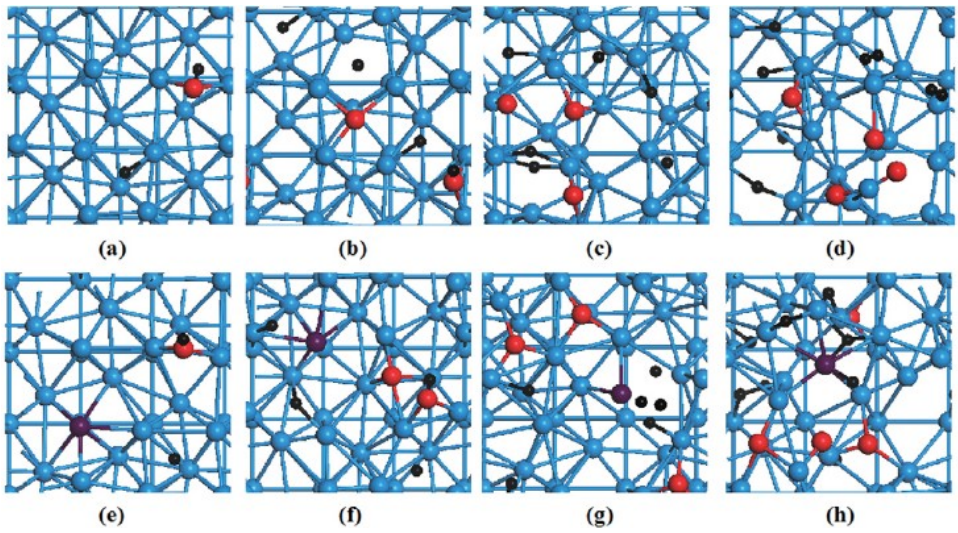

Fig. 1. Snapshots after 1~4 water molecules dissociatively adsorb on the γ-U(100) surface ((a)–(d)) and that with a surface substitutional Nb atom ((e)–(h)). Red, black, purple, and blue balls represent oxygen, hydrogen, niobium, and uranium atoms, respectively. The temperatures of the two adsorption systems are both 100K before the adsorption of the first water molecule.

References

[1] Yu Yang and Ping Zhang, *J. Phys.: Condens. Matter* **Vol. 27**, 175005 (2015).

3

Physical properties of a new $U_3Fe_{3-y}Sb_4$ system

Antonio P. Goncalves,[1] Margarida S. Henriques,[1,2] João C. Waerenborgh,[1] Martin Kupčík,[3] Natália Zahuráková,[3] Andrea Džubinská,[3] Ivan Čurlik,[3] Sergej Iľkovič,[3] Marian Reiffers[3]

[1] *Centro de Ciências e Tecnologias Nucleares (C2TN), Instituto Superior Técnico, Universidade de Lisboa, Estrada Nacional 10, 2695-066 Bobadela LRS, Portugal*
[2] *Institute of Physics, ASCR, Na Slovance 2, 182 21 Prague, Czech Republic*
[3] *Faculty of Humanities and Natural Sciences, Prešov University, 081 16 Prešov, Slovakia, e-mail: marian.reiffers@unipo.sk*

In the present work the crystal structure and electronic properties of $U_3Fe_{3-y}Sb_4$ were studied in a polycrystalline sample. $U_3Fe_{3-y}Sb_4$ crystallizes in the $Y_3Au_3Sb_4$-type structure, with lattice parameter a = 9.3 Å. Magnetization, AC susceptibility, specific heat, and electrical transport data indicate a ferromagnetic-type transition, with T_C = 110 K. The magnetization isotherms show a linear grow with the field, hinting for further splitting of the spin-up and spin-down subbands. The electrical resistivity, ρ(T), seems to be dominated at high temperatures by phonon contributions. Upon decreasing temperature ρ(T) also decreases, and at T_C there is a small anomaly. For T < 30 K, the resistivity slightly increases with decreasing temperature in zero field, but when applying fields the magnetoresistivity curves have a broad minimum, which shifts towards lower temperatures upon increasing the magnetic field. The applied magnetic field yields to a resistivity decrease at low temperatures.

4

Multi-Step Excitation Schemes in Laser Spectroscopy and Detection of Actinides and Lanthanides in Solutions

Igor Izosimov

Joint Institute for Nuclear Research, Joliot Curie 6, 141980 Dubna, Russia, e-mail: izosimov@jinr.ru

Development of laser spectroscopy with tunable lasers gives rise to new procedures for detection of trace amounts of various substances in various media. A possibility to tune a wavelength of laser radiation allows selective action on certain atoms and molecules and, hence, selective detection of these species [1-3]. The practical application of laser spectroscopy to analysis of different samples is confronted with one essential difficulty, namely the element to be detected must be permanently located in the area of interaction with laser radiation. Therefore the use of solutions of the substances to be analyzed is the most attractive from the practical standpoint. When the pulse (1ns) UV radiation produced by nitrogen laser is used for lanthanide and actinide excitation in solutions the UV radiation is absorbed with different molecules and as a consequence the background radiation is increased. Using short laser pulses for excitation of molecules and ions in liquids and time resolution for registration of luminescence and chemiluminescence produced by actinide and lanthanide ions we can efficiently separate target signals from short-lived background luminescence [1-3]. Currently, chemiluminescence methods [4] are widely used in biology and medicine for detection of various substances with limit of detection (*LOD)* of 10^{-6} M–10^{-13} M and determination of valence states. Selective excitation of detectable molecules can additionally decrease the intensity of background radiation. In addition, UV radiation is absorbed with chemiluminogen (luminol in our experiments) molecules, which makes difficult interpretation of the results of chemiluminescence registration. Therefore a key problem of chemiluminescence application to detection of lanthanides and actinides in solutions is an increase in the selectivity of detection. Appropriate selectivity of lanthanide or actinide molecules excitation can be reached by initiation of transitions within 4f- or 5f-electron shell, which correspond to visible spectral range of absorbed laser radiation. Since the energy of one-quantum excitation in visible range may be insufficient for initiation of chemiluminescence it was proposed to excite lanthanide or actinide ion by multi-quantum absorption of visible light [1-3]. The use of laser radiation with tunable wavelength allows selective excitation of actinide or lanthanide species with subsequent registration of luminescence or chemiluminescence. The scheme [1-3] *two step-one color*, i.e. in irradiation of actinide-containing solution by one laser (two photons absorbed from one laser pulse) and the scheme *two step-two color*, when a solution is irradiated by two lasers operating at different wavelengths (two photons absorbed from two synchronized laser pulses) were used for excitation of actinide ions in the range of 5f electron transitions.

Data on luminol chemiluminescence in solutions containing Sm(III), U(IV), and Pu(IV) are presented. The details of multi-step excitation of luminescence/chemiluminescence in solutions are considered. It is shown that a multi-step scheme of luminescence/chemiluminescence excitation increase both the sensitivity and selectivity of detection of substances.

References

[1] I.N. Izosimov, *Phys. Part. Nucl.* **38**, 177 (2007). DOI: 10.1134/s1063779607020025

[2] I.N. Izosimov, N.G. Firsin, N.G. Gorshkov, S.N. Nekhoroshkov, *Hyperfine Interact.* **227**, 271(2014). DOI: 10.1007/s10751-013-0990-7

[3] I.N. Izosimov, *Journal of Radioanalytical and Nucl. Chem.* **304**, 207 (2015). DOI: 10.1007/s10967-014-3601-4

[4] C. Dodeigne, L. Thunus, R. Lejeune, *Talanta*, **51**, 415 (2000).

5

Laser remote analysis for MOX fuel and its application for rapid and in-situ analysis in decommissioning of "Fukushima Daiich" nuclear power station

Ikuo Wakaida, Katsuaki Akaoka, Masabumi Miyabe, Hironori Ohba,
Morihisa Saeki, Masaki Oba, Chikara Ito, Masaaki Kato

Collaborative Laboratories for Advanced Decommissioning Science,
Japan Atomic Energy Agency, 2-4 Shirakata, Tokai-mura, Naka-gun, IBARAKI, 319-1195, JAPAN
e-mail: wakaida.ikuo@jaea.go.jp

In the next generation nuclear fuel cycle system, the development and utilization of the Low-decontaminated MOX fuel with fissionable Miner Actinide elements (MA) such as Plutonium, Neptunium and Curium, is strongly required from the viewpoint of simplification of the reprocessing process, reduction of the environmental burden by conversion of long-lived nuclide into short-lived one, sustainable use of nuclear fuel resources and resistance to nuclear proliferation. In order to promote the use of MOX with MA, it will be indispensable to develop the analytical techniques for the manufacturing process of the fuel and for the safeguards by continuous monitoring and quick surveillance of the U and Pu mass flow. The conventional chemical analysis, however, has some problems such as high radiation exposure during the analytical work, generation of radioactive analysis waste, long and tedious chemical separation and the results high analysis cost. For the safeguard analysis, Non Destructive Assay (NDA) of Pu using by ^{3}He neutron detector, which is successful developing in highly de-contaminated fuel cycle, cannot be applicable in MOX with MA fuel because the spontaneous neutron emission rate from Cm is about 10,000 times greater than that from Pu and the γ-ray from FP will strongly interfere the analysis of Pu isotopes. And more, by the under supply of ^{3}He, the price come to be several times, and it will become difficult to obtain ^{3}He itself. So, the development of remote analysis based on a new technology without neutron and/or γ-ray emission spectroscopy is strongly required.

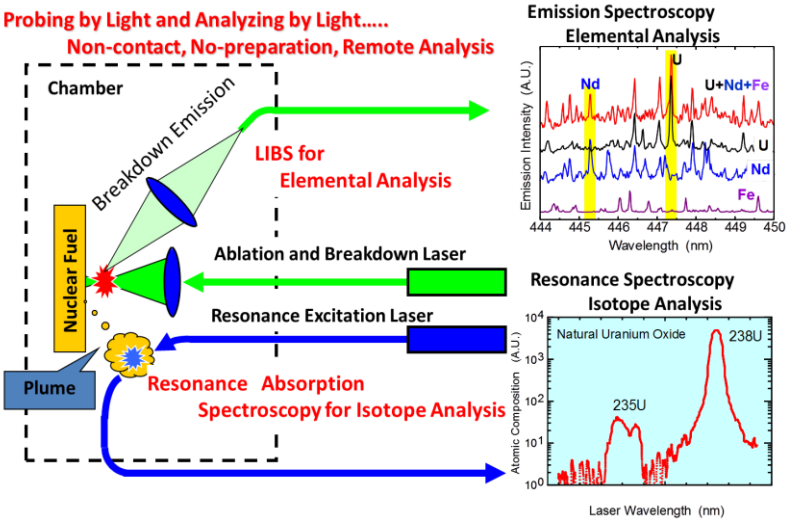

Fig.1 Basic Concept of Laser Remote Analysis

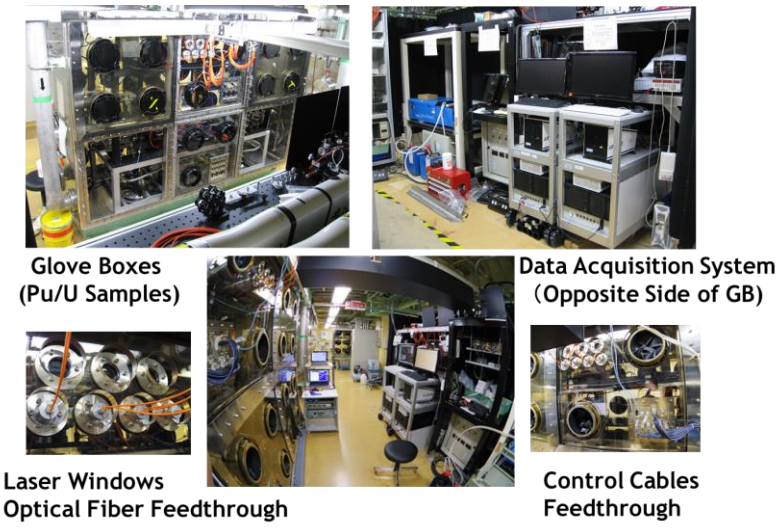

Fig.2 Glove Boxes for Laser Spectroscopy and DAQ

And more, as the special case in recent Japan, development of onsite and in-situ remote diagnostic/analysis techniques under the severe environments such as high radiation activity condition, will be strongly required for decommissioning of "Fukushima Daiich" nuclear power station which contained damaged or melt downed core by the "Tsunami" accident in the large earthquake.

As shown in Fig.1, the concept of probing by light and diagnostic by light will be one of the powerful choices to accomplish these requirements, so we are now developing the remote diagnostic technique for simultaneous analysis of element and isotope ratio by the combination of Laser Induced Breakdown Spectroscopy (LIBS)[1] and Laser Ablation Resonance Absorption Spectroscopy (LARAS)[2].

To obtain emission spectra, especially for MOX sample, we had constructed specialized glove box with auto and remote arraignment system for LIBS and ARAS (Fig.2). Basic LIBS technique was applied to elemental analysis under the reduced pressure of Ar gas and the high resolution Echelle spectrometer with ICCD camera was used for the time resolved spectroscopy. The detection lower limit of several 100 ppm for simulated Actinide in U oxide, and several 1,000 ppm of Pu in U oxide have been achieved. The relative error, which is important performance for quantitative analysis, under 5% has been also successfully obtained within 5 min. diagnostic operation. For isotope analysis, LARAS by use of handmade tunable single mode semiconductor laser was applied to ablated plume. U and Pu isotopes (^{235}U in ^{238}U, ^{240}Pu in ^{239}Pu) have been observed separately and also Hyper Fine Structure of ^{239}Pu has been clearly demonstrated (Fig.3). Detection lower limit of several ten ppm for specified isotope and quantitative error under 1% have been accomplished within 5 min. operation.

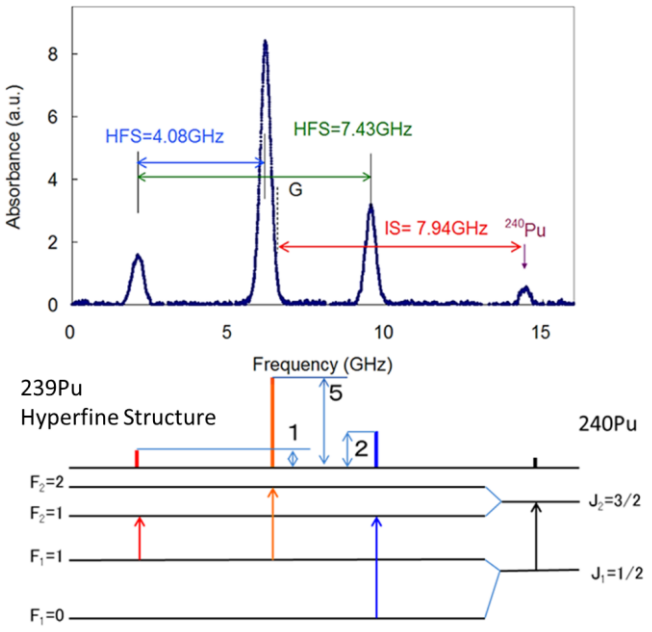

Fig.3 Hyperfine Spectrum of ^{239}Pu by LARAS

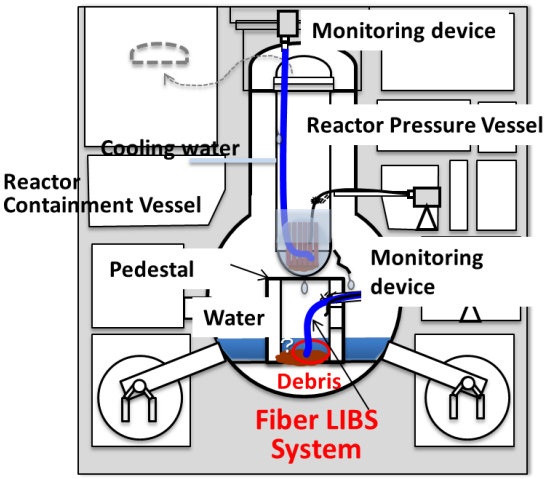

Schematics of In-Vessel Monitoring

Fig.4 For "Fukushima" Sever Accident

For the decommissioning of "Fukushima Daiich" nuclear power station, rapid, easy, simple, onsite and in-situ remote monitoring/diagnostic/analysis techniques under the severe environments will be also indispensable (Fig.4). Optical fiber based LIBS Probe[1][3] made by radiation resistant optical fiber will be one of the choice for the monitoring, and is now under construction as a portable prototype[4] (Fig.5). For the use under cooling water condition, gas bubbling mechanism will be installed in this probe. And just this time, we have successfully observed some specific spectra from the simulated sample of molten debris made by sintered oxide of Zr (fuel assembly material) and U under water condition or radioactive field of 10kGy/h (total dose of 2MGy).

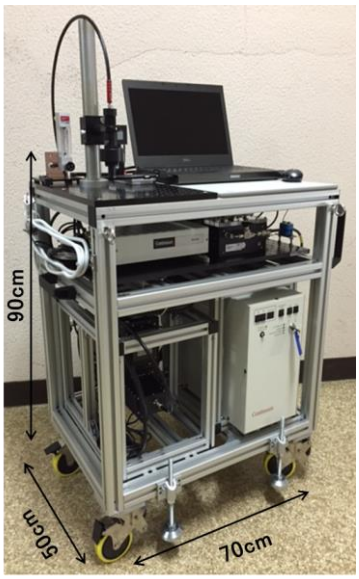

Fig.5 Portable Fiber LIBS

References

[1] Francisco J. et. al., Anal. Chem. 85 (2013) 640−669
[2]M. Miyabe, et. al., Hyperfine interact 216, (2013) 71-77
[3] A.I. Whitehouse, et al., Spectrochimica Acta Part B 56 (2001) 821-830
[4] M. Saeki, et al., J Nucl Sci Tech, 51 7-8 (2014) 930-938

B6

Thermal expansion and thermodynamical properties of Ce-based compounds $CeCuAl_3$, $CePt_3Si$, and $CePt_3B$ theory and experiment

D. Legut, R. Sykora, G. Rogl, H. Müller, E. Bauer, S. Puchegger, M. Zehetbauer, P. Rogl, M. Klicpera, P. Javorsky

IT4Innovations Center, VSB TUO, CZ

We report theoretical investigations of the lattice dynamics of the Ce-based systems using first-principle calculations based on the density functional theory. Vibrations of the Ce compounds are studied within the quasi-harmonic approximation. This allows us to analyse quantities like thermal expansion coefficient, specific heat at constant pressure, etc. We determine the Debye temperatures of $CePt_3Si$ and $CePt_3B$ by calculating the phonon density of states in equilibrium and by calculating the single crystal elastic constants. Resonant ultrasound spectroscopy was used to determine Young's elastic modulus E and Poissons ratio v and from them the bulk and shear moduli were calculated from E and v and using Anderson's equation the Debye temperatures were estimated in accord with theoretical predictions. For the $CeCuAl_3$ the specific heat shows also very good agreement with measurements in the energy range of 0-300K.

Email of presenting author: dominik.legut@vsb.cz

Long abstract: was not submitted

First-principles studies on the charge density wave in uranium

Ruizhi Qiu[1], Haiyan Lu[1], Bingyun Ao[1], Tao Tang[1], Piheng Chen[1]

[1] *Institute of Materials, China Academy of Engineering Physics, Mianyang 621907, China*

The charge density wave (CDW) state of α-U (called α_1-U) [1] was studied through a first-principles total-energy minimization using the conjugate gradient algorithm. The optimized crystal structure of α_1-U is found to have the space group *Pbnm*, which was proposed in the earlier Landau-type theory [2] and isostructural with α-Np structure (see Fig. 1). This result is different from the previous first-principles studies [3-5]. In particular, the changes in the lattice parameters of *Pbnm*-U with respect to α-U agree with the experimental observations. In addition, the energetics stability of *Pbnm*-U with respect to α-U is confirmed by the enthalpy calculations and the value of critical pressure in the pressure-induced quantum transition from *Pbnm*-U to α-U is in good agreement with the experimental result. Moreover, the phonon calculation verified the dynamical unstability of α-U and stability of *Pbnm*-U. Finally the calculated electronic structures display the feature of the CDW state.

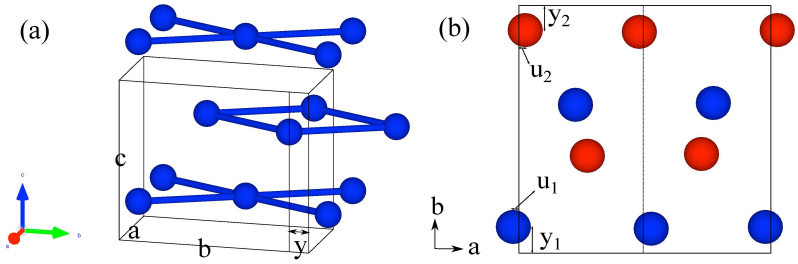

Fig. 1. The crystal structure of α-U (a) and *Pbnm*-U (b). *Pbnm*-U is shown in on the *ab* plane. The atoms situated in z = 1/4 and z = 3/4 layer are marked with red and blue, respectively. The arrows label the distorted direction with respect to the doubling α-U unit cell.

References

[1] G. L. Lander, E. Fisher and S. Bader, *Advances in Physics* **43**, 1 (1994).
[2] M. B. Walker, Phys. Rev. B **34**, 6830 (1986).
[3] L. Fast, O. Eriksson, B. Johansson, J. M. Wills, G. Straub, H. Roeder, and L. Nordström, Phys. Rev. Lett. **81**, 2978 (1998).
[4] S. Raymond, J. Bouchet, G. H. Lander, M. Le Tacon, G. Garbarino, M. Hoesch, J.-P. Rueff, M. Krisch, J. C. Lashley, R. K. Schulze, and R. C. Albers, Phys. Rev. Lett. **107**, 136401 (2011).
[5] A. Dewaele, J. Bouchet, F. Occelli, M. Hanfland, and G. Garbarino, Phys. Rev. B **88**, 134202 (2013).

The valence-fluctuating ground state of plutonium

M. Janoschek1, P. Das1, B. Chakrabarti2, D. L. Abernathy3, M. D. Lumsden3, J. M. Lawrence1, J. D. Thompson1, G. H. Lander4, J. N. Mitchell1, S. Richmond1, M. Ramos1, F. Trouw1, J-X. Zhu1, K. Haule2, G. Kotliar2, E. D. Bauer1

LANL, Rutgers, ORNL, ITU

We have used neutron spectroscopy to investigate plutonium metal, which is a prototypical material at the brink between bonding and nonbonding configurations. Our study [1] reveals that the ground state of plutonium is governed by valence fluctuations, that is, a quantum mechanical superposition of localized and itinerant electronic configurations as recently predicted by dynamical mean field theory. Our results not only resolve the long-standing controversy between experiment and theory on plutonium's magnetism but also suggest an improved understanding of the effects of such electronic dichotomy in complex materials.

[1] Science Advances **1**, e1500188 (2015).

Email of presenting author: lander@ill.fr

Long abstract: was not submitted

C3

Structure and Magnetism of Uranium Hydrides

Ladislav Havela,[1] Mykhaylo Paukov,[1] Miroslav Cieslar,[1] Zdenek Matej,[1] Milan Dopita,[1] Daria Drozdenko,[1] Peter Minarik,[1] Ilja Turek,[1] Martin Divis,[1] Thomas Gouder,[2] Frank Huber,[2] Oliver Dieste,[2] Thierry Wiss[2]

[1] *Charles University, Faculty of Mathematics and Physics, Ke Karlovu 5, 21216 Prague 2, Czech Rep.*
e-mail: havela@mag.mff.cuni.cz
[2] *European Commission, JRC, Institute for Transuranium Elements, Karlsruhe, Germany*

Uranium metal interacts with hydrogen gas readily at low (several mbar) pressure, producing ferromagnetic β-UH_3 with $T_C \approx 165$ K. The ferromagnetism is certainly related to the volume expansion, but such high T_C-value for relatively small shortest $d_{U\text{-}U} = 330$ pm remains quite surprizing. Mutatis mutandis, we explored whether the structure and composition can be varied while preserving the single-phase character. Essentially two routes were identified, one is the hydrogen exposure of the U_6T compounds, which yield the β-UH_3 structure with T atom residing on one of the two U positions [1,2]. The other route is to start from U alloys, which form in the γ-U (*bcc*) structure. We found that such precursors need much higher H_2 pressures (at least 4.5 bar) to yield hydrides, and such hydrides are not of the β-UH_3 type. One type of structure modification happens for U-Mo alloys, giving hydrides $(UH_3)_{1-x}Mo_x$, at which X-ray diffraction pointed to lost crystallinity [3]. However, the total scattering study (PDF) performed at ESRF (ID 22) with 80 keV photon energy revealed the β-UH_3 structure type but with grains size of merely 1-2 nm. Trying to exclude that there is a Mo segregation on the nano-scale, high-resolution TEM was employed. Some grains with atomic structure were observed, but there size looks somewhat larger than given by PDF (see the enclosed micrograph). This work indicated no Mo segregation. Such Mo-stabilized nano-granular hydrides can tolerate also many other metals, provided they were embedded into the *bcc* precursor.

Alloying with Zr leads to a crystalline hydride, but the structure corresponds to the α-UH_3 type, which is known as a transient species and was never obtained in a pure form. It represents the *bcc* phase with interstices filled by hydrogen, with volume expanded by 75% ($d_{U\text{-}U} = 360$ pm).

It was quite unexpected, but alloying by a principally non-magnetic element as Mo or Zr can enhance T_C of ferromagnetic UH_3 by 20-40 K, exceeding thus 200 K (Fig.1). Low Mo concentrations yield normal β-UH_3, but T_C is enhanced even in this case (180 K). Irrespective of composition and structure, magnetic properties are quite similar. One has to conclude that at least in this case the U-H interaction is modulating magnetic properties more than the U-U spacing, being the source for the 5*f* delocalization. What can be so important in the U-H interaction? Hydrogen in a compound with strongly electropositive elements behaves rather as an acceptor of electrons. Therefore one could expect certain reduction of the 5*f* occupancy. Calculations using the FPLO method [4] revealed that the 5*f* occupancy may even somewhat increase, but the 6*d* and 7*s* states are depleted. This suggests that the important hybridization of the 5*f* and 6*d* states is reduced in the hydrides. The 5*f*-states may remain practically alone at the Fermi level, which contributes to the 5*f* band narrowing (incipient localization), and electrical conductivity is reduced.

Acknowledgements: This work was supported by the Czech Science Foundation under the grant No. 15–01100S. The work at ITU were supported by the European FP7 TALISMAN project, under contract with the European Commission.

References

[1] H. Drulis, F. G. Vagizov, M. Drulis, and T. Mydlarz, Phys.Rev. B**52** (1995) 9500.
[2] A.V. Andreev, M.I. Bartashevich, A.V. Deryagin, L. Havela, V. Sechovsky, Phys.Stat.Sol. A **98** (1986) K47.
[3] I. Tkach, S. Mašková, Z. Matěj, N.-T.H. Kim-Ngan, A.V. Andreev, L. Havela, Phys.Rev. B **88** (2013) 060407(R).
[4] I. Tkach, M. Paukov, D. Drozdenko, M. Cieslar, B. Vondráčková, Z. Matěj, D. Kriegner, A.V. Andreev, N.-T.H. Kim-Ngan, I. Turek, M. Diviš, and L. Havela, Phys.Rev. B 91 (2015) 115116.
[5] L. Havela, I. Tkach, M. Paukov, Z. Matej, D. Drozdenko, A.V. Andreev, N.-T.H. Kim-Ngan, J. Alloys Comp. 645 (2015) S190.

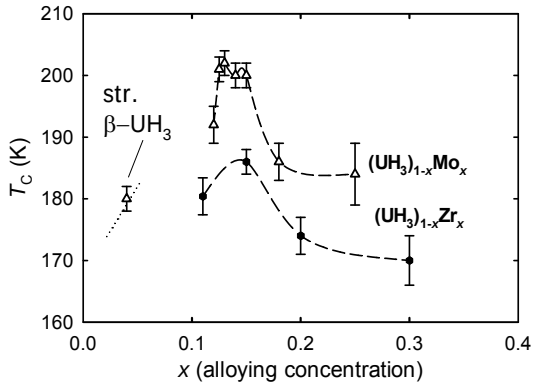

Fig. 1. Variations of the Curie temperature in the two types of hydrides [5].

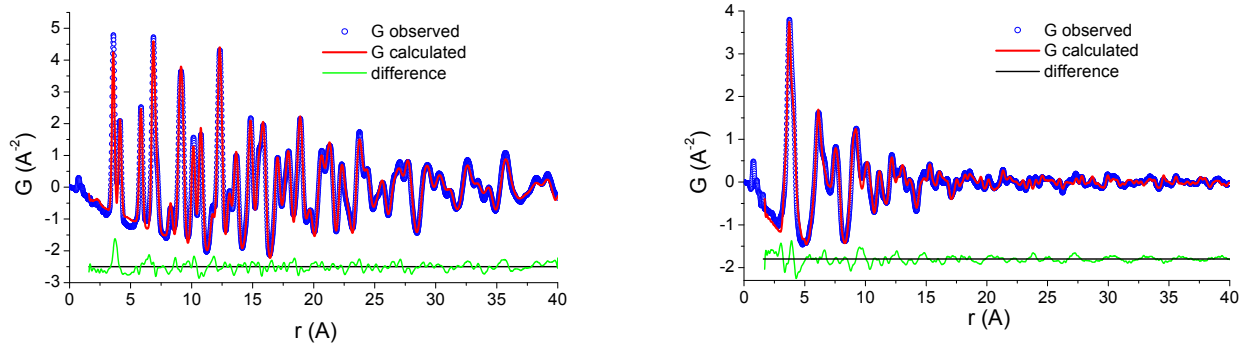

Fig. 2. Comparison of partial distribution function for $(UH_3)_{0.80}Zr_{0.20}$ (left) and $(UH_3)_{0.88}Mo_{0.12}$ (right). Please notice the fast decay of the envelope of the function for the Mo-alloyed hydride between 1-2 nm. Small fluctuations for high distances in this case are due to a small amount of spurious crystalline phases in this case. Experimental points in blue, red line represents the model data. The difference curve is green.

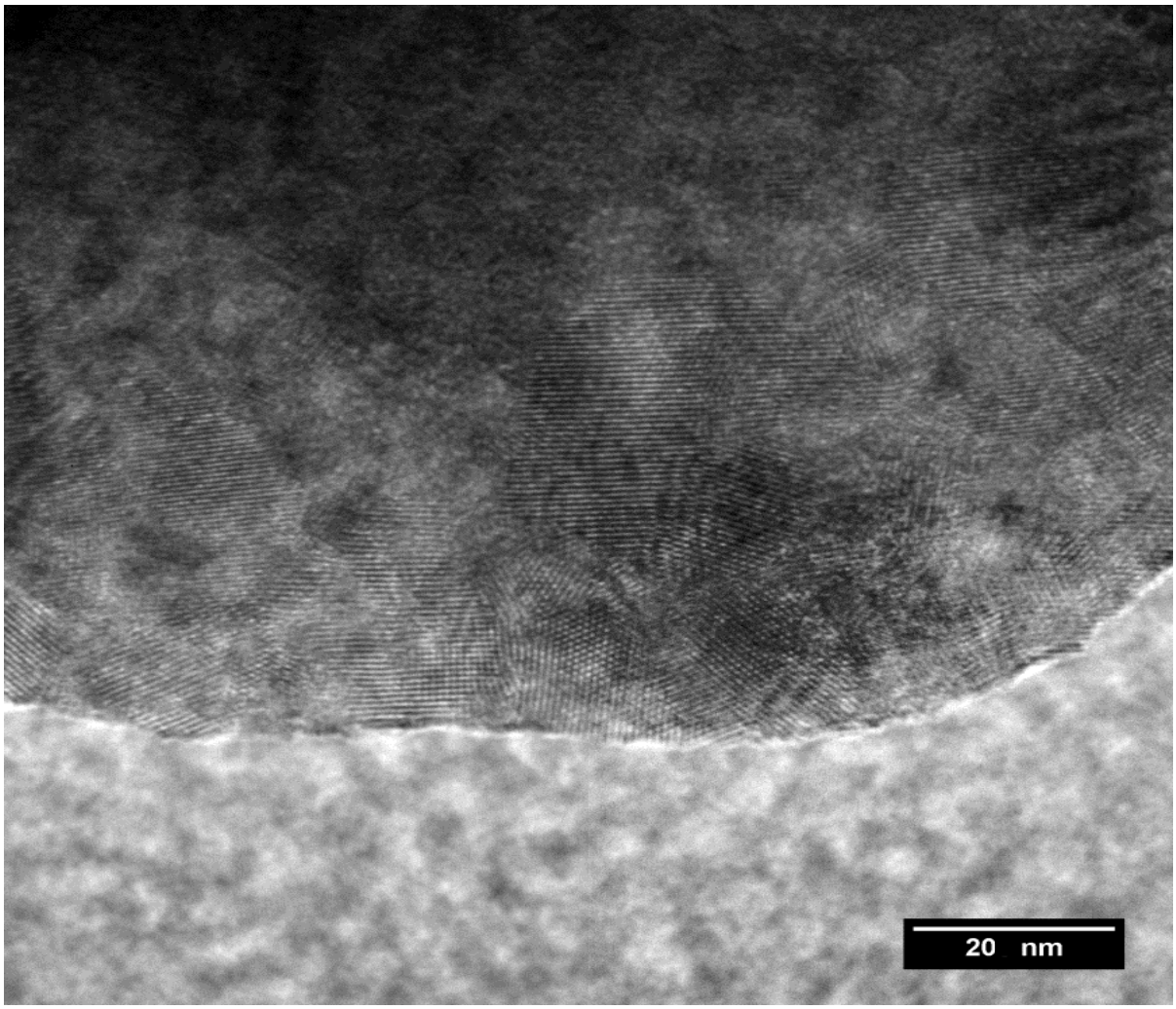

Fig. 3: HR-TEM micrograph of $(UH_3)_{0.88}Mo_{0.12}$ shows the grain size bigger than other techniques for this material. Important fact is that there is no sign of Mo segregation. EELS proved that U and Mo (and O) belong to the same phase. The scale is only approximate.

C4

The interaction between hydrogen and uranium thin films studied by synchrotron X-ray radiation

J. E. Darnbrough, R. M. Harker, D. Wermeille, G. H. Lander and R. Springell
UoB, AWE, ESRF, EC

The safe storage of uranium metal requires a thorough understanding of its corrosion reactions and in particular with hydrogen. We have studied the interaction between various epitaxial uranium films (covered by ~30 nm films of textured UO_2) with small partial pressures of hydrogen at the XMaS beamline at the ESRF synchrotron in Grenoble, France. The films were produced, at the University of Bristol, using either Nb or W buffer layers deposited on a-plane sapphire with U-thicknesses between 30 and 60 nm. Hydrogen exposure was attained in steps up to 500 mbar of 4% H_2/Ar at temperatures of 80, 140 and 200°C. Both X-ray reflectivity and X-ray diffraction were recorded as a function of time for different exposures and temperatures. Dramatic changes were observed, showing preferential reaction with the (110) U planes. In addition, the β-UH_3 (210) reflection was observed under certain experimental conditions, indicating the formation of crystalline uranium hydride.

Email of presenting author: j.e.darnbrough@bristol.ac.uk

Long abstract: was not submitted

C5

Electronic structure of U-Si binary intermetallic compounds by hybrid functional calculations

Xin Wang[1] ,Ruizhi Qiu[1], Li Huang[1], Pengcheng Zhang[1]

[1] *Institute of Materials, CAEP, No.9 Huafengxincun, Jiangyou City,Sichuan Province,621908 Jiangyou, China, e-mail: wangxin@alum.imr.ac.cn*

U–Si binary intermetallic compounds have received varying degrees of interest on the basic understanding of the structural, magnetic and electronic structures. They show diversified magnetic properties, *e.g.*, U_3Si_5 is a heavy fermion but both USi_3 and U_3Si exhibit Pauli paramagnetism. To date there is no universal picture on the interaction of U and Si due to the fact that it is hardly to describe the behavior of *5f* electrons within conventional DFT. Here through first-principles calculation within the hybrid functional (HSE) framework, we have investigated the electronic structure of U-Si binary intermetallic compounds, *i.e.*, P6/mmm U_3Si_5, Pm-3m USi_3 and U_3Si, and compared with the previous XPS experiments. Electronic structure derived within the HSE framework is in agreement with the experimental valence band spectrum. Local bonding analysis reveals that U-6s and 6p electrons do not participate in any bonding process. There are three hybridization zones for U-Si bonding. Present calculations provide a further insight on the role of U-5f electrons.

C6

Dynamic Magnetic Response Across the Pressure-Induced Structural Phase Transition in CeNi

A. Mirmelstein[1], A. Podlesnyak[2], A.I. Kolesnikov[3], G. Ehlers[2], D.L. Abernathy[2], V. Matvienko[1], G. J. Halder[4], Antonio M. dos Santos[2]

[1] *Russian Federal Nuclear Center-E.I. Zababakhin Research Institute of Technical Physics, 13 Vasiliev str., 456770 Snezhinsk, Russia, email: mirmelstein@mail.ru*
[2] *Quantum Condensed Matter Science Division, Oak Ridge National Laboratory, Oak Ridge, TN 37831, USA*
[3] *Chemical and Engineering Materials Division, Oak Ridge National Laboratory, Oak Ridge, TN 37831, USA*
[4] *X-Ray Science Division, Argonne National Laboratory, Argonne, IL 60439, USA*

Intermediate-valence compound CeNi experiences a pressure-induced first-order structural phase transition with volume jump and as such constitutes an attractive system to study pressure-driven *f*-electron delocalization behavior in the systems with an unstable *f*-electron shell. By means of x-ray and neutron powder diffraction techniques the structure of high-pressure CeNi phase is determined and the inelastic neutron scattering (INS) technique is employed to study the dynamic magnetic susceptibility of CeNi before and after the structural transition. The INS experiments reveal enhanced Ce 4f─Ni 3d hybridization due to the phase transition while the inelastic 4f magnetic form factor remains unchanged.

INTRODUCTION

Studying the mechanisms underlining the pressure-induced first-order structural phase transition with volume jump in f-electron systems is an important and interesting problem, which is closely related to understanding crossover between the localized and itinerant f electron behavior. The most famous and most studied example of such transformations is the isostructural $\gamma \rightarrow \alpha$ volume collapse transition in cerium metal, first reported in 1927 by Bridgman [1]. Since 1949, when the isostructural nature of $\gamma \rightarrow \alpha$ transition was established [2], it stimulated a lot of experimental and theoretical work aimed to explain the large isostructural volume change of ~ 15% as well as the replacement of the normal Curie-Weiss temperature dependence in the magnetic susceptibility of the γ phase, which is indicative of a local moment behavior, by a practically temperature independent susceptibility in α-Ce [3], suggesting a quenched moment state. The nature of this transition is still actively discussed [4-6]. Even more staggering example of the volume-collapse transitions in the f-electron systems is given by $\delta \rightarrow \alpha$ transformation in plutonium metal [7]. Many features of this transition still have no explanation, including stabilization of the fcc phase by alloying different elements, influence of defects and strains on the transformation. Details of the Pu electronic structure variation due to transition, especially f-electron configuration, are also unknown.

The intermediate-valence compound CeNi represents another exciting example of f-electron systems experiencing a pressure-induced structural instability. Study of CeNi looks attractive because of the following reasons. First, CeNi has the CrB-type orthorhombic crystal structure (space group *Cmcm*) repeatedly appearing in rare-earth and actinide metals under pressure such as α'-Ce, Pa, Nd, and Pr. The α-U metal has also this type of structure which is usually stable up to very high pressures. CeNi shows different behavior. Already at ambient pressure CeNi displays clear signatures of lattice instability upon cooling [8]. However structural transformation with abrupt volume change occurs only under relatively low pressure, easily accessible experimentally [9-11]. The structure of CeNi high pressure phase remained unknown for a long time, so that investigation

of the structural transition in this compound can be useful for better understanding of similar structures under pressure. Second, as soon as Ce valence in intermediate-valence CeNi differs significantly form integer value [12], one can expect the volume-collapse structural phase transition to shift the system towards the itinerant (bonding) f electron behavior (in this sense structural transition in CeNi can be considered as an analog of $\delta \rightarrow \alpha$ transformation in plutonium).

Our previous specific heat and magnetic susceptibility measurements showed that the behavior CeNi under chemical pressure is dominated by Kondo physics [11], i.e., by magnetic fluctuations. Inelastic neutron scattering (INS) technique is a powerful tool to study magnetic dynamic of intermediate valence systems. Thus, the aim of this work is to determine the crystal structure of CeNi high pressure phase using x-ray and neutron powder diffraction and to study the variation of magnetic excitation spectrum in CeNi due to structural transition by means of INS technique.

EXPERIMENTAL

To study pressure-induced structural variations in CeNi we performed x-ray diffraction experiments at room temperature and neutron diffraction experiments at 100 K. In-situ room temperature high-pressure Synchrotron X-ray measurements were carried out at beamline 17-BM-B at the Advanced Photon Source, Argonne National Laboratory. Time-of-flight neutron diffraction measurements at 100 K were performed at the Spallation Neutrons and Pressure (SNAP) beamline of the Spallation Neutron Source at Oak Ridge National Laboratory. The sample for these experiments was prepared using natural mixture of Ni isotopes. Detailed description of the sample preparation technology and experimental procedures are given in ref. [13] and in the presentation by V. Mativienko et al., at this Conference.

The CeNi sample of ~3 g in mass for INS experiments was prepared by the same technology as for the structural investigations, using ^{60}Ni isotope (enrichment ~99%). This isotope has nuclear cross section σ_S = 1.0 b, as compared to σ_S = 18.5 b for the natural isotopic composition. The reduction of nuclear scattering from Ni atoms by almost a factor of 20 makes it possible to extract the weak magnetic contribution from Ce atoms (magnetic cross section of Ce^{3+} ions is $\sigma_M \approx 3.7$ b [14]) with sufficient reliability and accuracy.

To generate pressure in the INS experiments we used the pressure cell from the Al alloy with He gas as a pressure transmitting medium. Measurements of the INS spectra of CeNi were performed using fine-resolution Fermi chopper spectrometer SEQUOIA (Spallation Neutron Source at Oak Ridge National Laboratory) [15] at temperature 20 K. Incident neutron energy was E_i = 150 meV. To measure inelastic magnetic form factor of CeNi we used the ARCS [16] (wide angular-range chopper spectrometer) instrument (Spallation Neutron Source at Oak Ridge National Laboratory). ARCS allows to measure the inelastic spectra at the same incident neutron energy E_i = 150 meV up to the high momentum transfer ~ 12 $Å^{-1}$ within the energy transfer region 50 -80 meV.

To evolve the magnetic contribution from the full measured inelastic signal, the experimental data were carefully treated taking into account all possible contributions to the total inelastic cross section. While measuring the INS spectrum without pressure cell there are contributions from CeNi phonons including multi-phonon processes as well as the Al background due to the materials surrounding the sample. While measuring under pressure the background situation becomes much more complicated due to the enhanced Al contribution (the material of pressure cell) and scattering from helium served as a pressure transmitting medium. The latter contribution is especially strong under increased pressure because already at the pressure of 0.4-0.45 GPa (the pressure values of our measurements) helium solidifies and gives huge inelastic signal. Nevertheless, we succeeded to evolve the magnetic contribution from CeNi exposed to the structural phase transition. Details of magnetic spectrum evaluation procedure will be reported elsewhere.

Note that we used He gas as a pressure transmitting medium with possibility of pressure adjustment on cooling because of high thermal contraction of CeNi and volume jump at the

transition. The cell pressure would essentially fall under cooling the assembly down to ~ 20 K in case of clamped pressure cell.

STRUCTURE OF CeNi HIGH PRESSURE PHASE

In this Section we will discuss only the main results of CeNi structural investigation under pressure. Details are published in ref. [13] and presented by V. Matvienko et al. at this Conference. The main result of our x-ray and neutron powder structural study consists in the determination for the first time of the CeNi high pressure phase structure which remained unknown since 1985, when this pressure-induced first-order phase transformation was discovered by Gignoux and Vioron [9]. From privete communications we know about a few attempts to identify this structure. We also try to do the same, but in vain. Now we can state that CeNi high pressure phase is described by the P*nma* space group, closely related to the CrB-type of ambient pressure CeNi structure (C*mcm* space group).

At room temperature the low pressure (LP) CeNi structure remains stable from ambient pressure up to $P \sim 0.7$ GPa. Between 0.7 and 2.1 GPa the x-ray diffraction (XRD) patterns of CeNi exhibit remarkable changes. Above 2.1 GPa only subtle variations of peak positions and intensities are observed (the high pressure (HP) domain), however upon further increase in pressure a new diffraction pattern develops suggesting one more structural transformation staring at $P \sim 4.9$ GPa (HP′phase), see Fig. 1.

The HP phase ($2.1 < P < 4.9$ GPa) has the orthorhombic crystal structure of the FeB-type (*Pnma* space group, Fig. 2). Both the FeB and CrB type structures contain a common structural unit, the trigonal prism, which is stacked differently to form either structure [18,19] (Fig. 3). If the *z* value of the 4c sites in the *Pnma* structure goes to zero, one obtains the higher-symmetry *Cmcm* structure [20] (Fig.4). Similarity of these structures is seen in the fact that the FeB structure is typical for the RNi compounds where R is the rare-earth metal from the second half of the lanthanide series, while light lanthanides, including cerium, form the crystal lattice of the CrB type [19]. Therefore, the *Pnma* symmetry is more favorable for the small rare earth ionic volume than *Cmcm*, so that the pressure-induced conversion from a CrB to a FeB type structure is not surprising.

Moreover, Hohnke и Parthé [21] established the set of transformation equations between the crystal lattice parameters of these two structures, according to which in the "ideal" case the volumes of FeB and CrB structures are equal. As demonstrated in ref. [13], the experimental values of FeB crystal lattice parameters are very close to the "ideal" values, while some subtle deviations are caused by the ~1.3% volume jump at the transition at temperature $T = 298$ K.

At $T = 100$ K a slightly different picture is observed. The initial CrB-type structure is conserved at low pressures. In the vicinity of 1 GPa of pressure the CeNi diffraction pattern suffers essential modifications compatible with the expected *Cmcm* → *Pnma* symmetry change. At the higher pressure XRD varies again as compared to that observed at the lower pressures. In addition to the reflections of *Pnma* FeB phase, new Bragg peaks appear, the most noticeable at $d \geq 5$ Å. At $P = 5.05$ ГПа the XRD pattern is described by a new orthorhombic cell with crystal lattice parameters close to those found for the quenched modification of the TbNi compound (*Pnma* space group) [18]. This structure is closely related to the FeB type structure with transformation equations $a_{TbNi}=3\times a_{FeB}$; $b_{TbNi}=b_{FeB}$; $c_{TbNi}=c_{FeB}$ (Fig. 5). We will call it $3\times a_{FeB}$*Pnma* for a convenience. Moreover, we were able to describe the experimental data at $P = 0.96$ GPa, assuming this state to be a mixture of low-pressure *Cmcm* and high-pressure $3\times a_{FeB}$ *Pnma* structures. According to the FullProf analysis, the volume fraction of low-pressure phase is 37±1%, and the high-pressure phase occupies 63±1% of the sample volume. The volume jump at lower temperature ($T = 100$ K, $P = 0.96$ GPa) is about 7.9%, i.e., as expected, much higher than at room temperature.

We did not observe the pure FeB structure at 100 K. Thus, we cannot say whether or not there is a pressure window for the FeB structure between the transition line established in [9] and confirmed

in [11] by magnetic measurements, and the transition to the $3\times a_{FeB}$ *Pnma* at around 1 GPa (see Fig. 1). We believe that the FeB structure *may* appear here and then transforms, almost immediately, under increase in pressure into the observed $3\times a_{FeB}$ *Pnma* structure. Such a behavior cannot be excluded since one of these structures (CrB and FeB) can transform to the other directly or via a sequence of polymorphous transformations [18,21]

Figure 1 shows that at room temperature a second structure modification takes place at pressure above 4.9 GPa. The X-ray diffraction patterns of CeNi above this pressure can no longer be described by a single phase, neither pure FeB nor its polymorphous modifications of the $n\times a_{FeB}$*Pnma* type (n = 2,3 etc.). Therefore, it seems quite reasonable to assume that at $P > 4.9$ GPa and at room temperature the CeNi sample consists of a mixture of HP FeB phase and $n\times a_{FeB}$*Pnma* structures, which can be called "*Pnma*-based mixed phase structure". If this is true, then the approximate CeNi *P*-*T* phase diagram takes the form shown in Fig. 1 with the second transition line separating the FeB and *Pnma*-based mixed phase structural states. Note, that an extrapolation of this transition line to $T = 0$ goes to a critical pressure value $P = \sim 0.4$ GPa, close to that obtained by specific heat measurements under pressure in ref. [17]. Besides, the results of [17], as well as our previous data describing the thermopower vs. pressure measurements for CeNi at 300 K [23] (Fig. 6) confirm the existence of two transitions at approximately the same pressure values as shown in Fig. 1 for both low and room temperatures.

Having obtained the structural data we derived the equations of states for CeNi at $T = 100$ K and 298 K [13]. Besides, using the density functional theory approach (Vienna ab initio simulation package (VASP), we calculated the total energy of CeNi for both CrB (C*mcm*) and FrB (P*nma*) phases under varying crystal lattice parameters imitating pressure variation. Figure 7 shows that under increase of pressure, i.e., under decrease in crystal lattice parameters as follows from the x-ray diffraction data at room temperature, the energies of LP and HP phases cross at about 0.94 GPa of pressure. This result confirms the stability of the *Cmcm* CeNi crystal structure at ambient pressure down to the lowest temperature and, at the same time, provides an explanation for the *Cmcm* $\rightarrow$ *Pnma* structural phase transition at ~1 GPa. The computed primitive cell volumes and bulk moduli are found to be in a reasonable agreement with the experimental values [13]. Note, that the calculated bulk modulus of the *Cmcm* structure turns out to be lower than that of the *Pnma* structure, as it was found in the experiment.

In conclusion, by means of X-ray and neutron powder diffraction measurements we have shown that pressure induces in CeNi structural phase transitions from a low-pressure CrB-type of structure (*Cmcm* space group) to high-pressure phases belonging to the *Pnma* space group. The experimental results allow us to draw an approximate *P*-*T* phase diagram of CeNi according to which CeNi undergoes two successive phase transitions within the *P*-*T* domain $P < 8$ GPa, $T \leq 300$ K. The first transition converts the LP structure into the FeB (*Pnma*) structure (which was not, however, observed experimentally at $T = 100$ K), while the second transition separates the FeB structure (HP phase) and *Pnma*-based mixed phase H′ state.

MAGNETIC EXCITATION SPECTRUM OF CeNi

As mentioned above, CeNi is an intermediate-valence (IV) system. According to the XAS data, the Ce valence increases from ~3.11 to 3.14 under cooling from 300 K down to ~ 20 K [12]. The CeNi magnetic susceptibility χ displays strong anisotropy [9]. However, for powder sample, as well as along the ***c*** axis of a single crystal, it shows the shape typical of IV systems with a broad maximum around 150 K (Fig. 8). At $T > 300$ K χ follows the Curie-Weiss law with the free Ce^{3+} ion effective moment value $p = g[(J(J+1)]^2 = 2.53$. At low temperatures χ becomes temperature independent, while anomalous upturn of $\chi(T)$ below 20 K has, most probably, an intrinsic origin connected presumably with coherent f-d hybridization [24,25].

In the intermediate-valence state the hybridization of 4*f* wave functions with conducting-band

states is large, causing the suppression of sharp crystal-field excitations and the appearance of a strongly damped, featureless magnetic response. The low-temperature dynamic magnetic response of intermetallic Ce-based IV compounds is typically dominated by one broad inelastic peak centered at an energy of several tens to some hundreds of meV (see [26] and references therein). The energy of magnetic response maximum is related to the characteristic energy scale (i.e. Kondo temperature). When temperature is increased, the spectral weight is gradually transferred to a quasielastic line, corresponding to the regime of local magnetic moments.

In CeNi, however, the dynamic magnetic response is of more complicated nature [14]. At low temperature ~ 10 K no magnetic intensity was found up to energy E ~ 15 meV, indicating a spin-gap-like response. This is a clear evidence for the formation of a singlet ground state due to electron correlations. At higher energies the magnetic response consist of (i) a broad structureless contribution, extending beyond 60 meV, which is a characteristic feature of valence-fluctuating materials, and (ii) two extra narrow peaks at about 18 and 34 meV, which exist for practically all **Q** vectors investigated, and whose intensities vary as function of both the reduced q vectors and the direction in the reciprocal space. It implies that the IV state in CeNi cannot be described by a single-ion Anderson model, and that magnetic correlations should be taken into account. The extra peaks were tentatively related to crystal-field interactions, which are of the same order of magnitude in CeNi as the Kondo temperature [14].

Figure 9 shows the magnetic scattering function $S_{mag}(E,T=20\ K)$ for CeNi measured at 20 K and ambient pressure without pressure cell using the spectrometer SEQUOIA. Bottom-loading close cycle refrigerator (CCR) was used to cool the sample. After nuclear background subtraction, the magnetic inelastic signal was averaged over all scattering vector Q directions and then summed up within the |Q| interval 1.5 to 4 Å^{-1}. For higher |Q| the magnetic signal is suppressed by a sharp decrease of the magnetic form-factor $|F(Q)|^2$.

To describe $S_{mag}(E,T=20\ K)$ the standard expression was used:

$$S_{mag}(Q,E,T) \sim |F(Q)|^2 \frac{E}{1-\exp(-E/k_B T)} \frac{\Gamma/2}{(\Gamma/2)^2+(E-E_0)^2}, \qquad (1)$$

where Γ is the full width at half maximum (FWHM) of Lorentzian spectral component. The energy E_0 determines the characteristic energy scale of the IV system, i.e., the Kondo temperature $T_K = E_0/k_B$.

As seen from Fig. 9, three Lorentzian functions are required to describe the measured $S_{mag}(E,T=20\ K)$, namely, two very narrow and one broad with the parameters: (1) E_0 = 15±0.2 meV, Γ/2 = 3.3±0.2 meV, (2) E_0 = 30±0.3 meV, Γ/2 = 3.3± 0.2 meV, (3) E_0 = 40± 2 meV, Γ/2 = 42± 3 meV.

These parameters are very close to those found for $CeNi^{60}$ single crystal in ref. [14]: (1) E_0 ~ 18 meV, Γ/2 = 4.5 ± 0.5 meV, (2) E_0 ~34 meV, Γ/2 = 4.5 ± 0.5 meV, (3) E_0 ~ 46 meV, Γ/2 = 24 meV.

Thus, our results agree with the data reported in [14]. According to Q-dependence of our data, spectral components (1) and (2) presumably have magnetic origin. However, the maxima of the Al phonon density of states (PDOS) have almost the same energies 16-17 and 31-32 meV (Fig. 9). Therefore, even negligible error in subtracting nuclear inelastic contribution from Al has a dramatic influence on the $S_{mag}(E)$ function. Hence, we cannot further discuss the narrow spectral components the nature of which remains unclear. To solve this problem requires careful INS investigations of single crystal as a function of pressure. Thus, we neglect the narrow peaks for further numerical evaluation and describe the experimental CeNi magnetic scattering function by a single "smooth" Lorentzian with the parameters E_0 = 33 meV and Γ/2 = 44 meV (solid brown curve in Fig. 9). These parameters coincide exactly with the data for the powder $CeNi^{60}$ sample in ref. [27].

To measure the dynamic magnetic response of CeNi after the structural transition, we performed the INS experiment at T = 20 K and P = 0.4 GPa using the top-loading He cryostat. In

this case the CeNi sample is surrounded by massive Al (material of the pressure cell) and He (pressure transmitting medium), so that the nuclear background increases dramatically as compared to the case of measurements at ambient pressure (note also, that helium cryostat has larger background compared to the CCR). As a result, nuclear scattering dominates the inelastic spectrum at low energies, so that the accurate separation of weak magnetic contribution becomes a very difficult task, unsolvable at the energy transfer below ~40 meV. Therefore, it is not possible to follow the behavior of two narrow peaks in the magnetic scattering function under pressure. Above the energy transfer E ~ 40 meV the magnetic scattering function $S_{mag}(E)$ of CeNi after the structural *Cmcm* → *Pnma* transition can be described by Lorentzian with the parameters E_0 = 50 meV and Γ/2 = 55 meV (Fig. 10). Therefore, the structural transition accompanied by volume jump (ΔV/V ~ 8% at low temperatures, see preceding section) results in the increase in characteristic energy scale of magnetic fluctuations (Kondo temperature) while their lifetime decreases, i.e., fluctuation damp faster than at ambient pressure.

The results obtained allow us to make some rough estimates. It was shown in ref. [28], that for Ce-based materials with an unstable 4f shell the effective 4f occupation $\langle n_f \rangle$ and the Kondo energy E_0 are connected by an empirical relation:

$$\langle n_f \rangle \approx 1 - 0.05(\text{meV}^{-1}) \times E_0 . \qquad (2)$$

At ambient pressure E_0 = 33 meV, and Eq. (2) gives $\langle n_f \rangle \approx 0.84$ (corresponding to the Ce ion valence 3.16). At *P* = 0.4 GPa (after the transition) E_0 = 50 meV and $\langle n_f \rangle \approx 0.75$ (the Ce ion valence is 3.25). As known, the electronic specific heat coefficient γ and the value of Pauli-like magnetic susceptibility of intermediate-valence systems at low temperatures are proportional to $\langle n_f \rangle$ and inverse proportional to E_0 ([29] and reference therein):

$$\gamma, \chi_0 \propto \langle n_f \rangle / E_0 . \qquad (3)$$

Therefore, our INS results give:

$$\gamma(P=0)/\gamma(P=0.4\Gamma\Pi a) \approx \chi_0(P=0)/\chi_0(P=0.4\Gamma\Pi a) \approx (\langle n_f \rangle / E_0)_{P=0} / (\langle n_f \rangle / E_0)_{P=0,4\Gamma\Pi a} \approx 1.7 \qquad (4)$$

This value can be compared with the experimental data obtained by bulk measurements. From ref. 11 (Fig. 11), the ratio χ_0(*T*= 30 K, ambient pressure)/χ_0(*T*= 30 K, *P* = 0.47 ГПа[1]) ≈ 1.33. Close value of the ratio γ(ambient pressure)/γ(*P*=0.4 GPa) ≈ 1.36 follows from the CeNi specific heat measurements under pressure [17]. Thus, three different experimental methods performed using three different CeNi samples give similar values characterizing the variation of CeNi electronic properties as a result of the structural *Cmcm*→*Pnma* transition with the volume jump. Note, that if one consider the value of E_0 = 40 meV (the energy of the broad peak (3) in Fig. 9) as a characterization of the initial CeNi state instead of "smooth" value E_0 = 33 meV, then the 4f occupation at ambient pressure decreases down to $\langle n_f \rangle \approx 0.8$ and the ratio (4) acquires the value $\chi_0(P=0)/\chi_0(P = 0.4\ \text{GPa}) = 1.33$, equal to those from bulk measurements. We cannot say which is more correct assessment, 1.7 or 1.33, since we don't understand the nature of narrow spectral components. Nevertheless, our INS experiments provide a consistent description of the electronic structure variation due to pressure-induced volume-collapse structural phase transition. Namely, the Kondo temperature increases as a result of the enhanced Ce4f-Ni3d hybridization while the

[1] This pressure value is the result of cooling the pressure cell with CeNi sample down to 30 K if the applied pressure at room temperature was as high as 0.8 GPa [11].

effective 4f shell occupation (4f count) decreases. Note that the enhanced 4f-3d hybridization after the transition follows also from our structural results and *ab initio* CeNi electronic structure calculations [13]. Therefore, as well as in the case of metallic cerium [4-6], the interaction between 4f electrons of Ce and the conduction band electrons plays a key role in the mechanism of the volume-collapse structural transition in CeNi.

MAGNETIC FORM FACTOR OF CeNi

The procedure to evolve the magnetic contribution from the measured INS spectrum showed that within the energy transfer range between ~ 55 and 85 meV, i.e. around the $S_{mag}(E)$ maxima, nuclear contributions becomes negligible. By the other words, independently on the experimental conditions (measurements without pressure cell at ambient pressure or under pressure P = 0.4 using the pressure cell) the measured inelastic signal is formed by the magnetic contribution plus some weak background almost independent of the momentum transfer Q. Experimental measurements of the CeNi magnetic form factor before and after the structural transition becomes possible because of this fortunate circumstance.

The INS measurements to determine the magnetic form factor were performed using ARCS instrument with the incident neutron energy E_i = 150 meV within the momentum transfer |Q| window up to ~ 12 $Å^{-1}$. To determine the form factor the measured spectra were first averaged over all the Q direction for each |Q| giving the functions $S_{mag}(E,|Q|)$. Then these $S_{mag}(E,|Q|)$ function were integrated within the energy window 60-80 meV providing the intensity vs. |Q| dependence (see Fig. 12). The results obtained demonstrates that the dynamic magnetic response of CeNi follows the free ion Ce^{3+} magnetic form factor before and after the structural transition in spite of essential variation of Kondo temperature and spectral response broadening. Therefore, as in the case of $\gamma \rightarrow \alpha$ transition in cerium [5, 30], 4f electrons remains localized, while strongly hybridized with conducting bands, in the CeNi P*nma* structure.

CONCLUSIONS

Pressure-induced volume-collapse structural phase transition in CeNi is investigated by means of x-ray and neutron diffraction as well as by using the neutron inelastic scattering technique. The pressure-induced crystal structure is shown to belong to the P*nma* space group. An approximate phase diagram is suggested. The experimental results clearly demonstrate the increase of the characteristic energy scale of magnetic fluctuations (Kondo temperature) and the decrease of effective occupation of the $4f^1$(J=5/2) ground state of the collapsed phase due to the enhanced Ce4f-Ni3d hybridization. The space distribution of magnetic density does not change under transition and remains the same as in the free Ce^{3+} ion.

Acknowledgments

Research at Oak Ridge National Laboratory's Spallation Neutron Source was supported by the Scientific User Facilities Division, Office of Basic Energy Sciences, U.S. Department of Energy. Part of this work was supported by the Materials Sciences and Engineering Division, U.S. Department of Energy, Basic Energy Sciences. This research used resources of the National Energy Research Scientific Computing Center, which is supported by the Office of Science of the U.S. Department of Energy under Contract No. DE-AC02-05CH11231. Work at RFNC-VNIITF was supported in part by Contract B601122 between LLNL and RFNC-VNIITF.

References

1. P.W. Bridgman, Proc. Am. Acad. Arts. Sci. **62**, 207 (1927).
2. A.W. Lawson and T.-Y. Tang, Phys. Rev. **76**, 301 (1949).
3. D.C. Koskenmaki and K.A. Gschneidner, in *Handbook on the Physics and Chemistry of Rare Earth*, edited by K.A. Gschneidner and L.R. Eyring (North-Holland, Amsterdam, 1978), Vol.1, Chap,4, pp. 337-377.
4. N. Lanata, Yong-Xin Yao, Cai-Zhuang Wang, Kai-Ming Ho, Jörg Schmalian, K. Haule, and G. Kotliar, Phys. Rev. Lett. **111**, 196801 (2013)
5. B. Chakrabarti, M.E. Pezzoli, G. Sordi, K. Haule, G. Kotliar, Phys. Rev. B **89**, 125113 (2014).
6. N. Lanata, Yong-Xin Yao, Cai-Zhuang Wang, Kai-Ming Ho, Jörg Schmalian, K. Haule, and G. Kotliar, Phys. Rev. B **90**, 161104(R) (2014).
7. S.S. Hecker, in Challenge in Plutonium Science (Los Alamos Science, 26, 2000), Vol.2, p.292.
8. E.S. Clementyev, P.A. Alekseev, M. Braden, J.-M. Mignot, G. Lapertot, V.N. Lazukiv, I.P. Sadikov, Phys. Rev. B **57**, R8099 (1998).
9. Gignoux and J. Voiron, Phys. Rev. B **32**, 4822 (1985).
10. D. Gignoux, C. Vettier and J. Voiron, JMMM **70**, 388 (1987).
11. A. Mirmelstein, E. Clementyev, O. Kerbel, D. Kozlenko et al., Nucl. Mater. **385**, 57 (2009).
12. V.N. Lazukov, E.N. Nefedova, V.V. Sikolenko, U. Staub, P.A. Alekseev et al., Appl. Phys. A **74** [Suppl.], S559-S561 (2002)
13. A. Mirmelstein, A. Podlesnyak, A.M. dos Santos, G. Ehlers et al., Phys. Rev. B **92**, 054102 (2015).
14. E.S. Clementyev, J.-M. Mignot, P.A. Alekseev, V.N.Lazukov et al., Phys. Rev. B **61** 6189 (2000).
15. G.E. Granroth, A.I. Kolesnikov, T.E. Sherline, J.P. Clancy, K.A. Ross, J.P. C. Ruff, B.D. Gaulin, and S.E. Nagler, J. Phys. Conf. Ser. **251**, 012058 (2010).
16. D.L. Abernathy, M.B. Stone, M.J. Loguillo, M.S. Lucas, O. Delaire, X. Tang, J.Y.Y. Lin, and B. Fultz, Rev. Sci. Instrum. **83**, 015114 (2012).
17. S. Takaynagi, S. Araki, R. Settai, Y. Onuki and N. Mori, J. Phys. Soc. Jap. **70**, 753 (2001).
18 R. Lemaire and D. Paccard, Journal of the Less-Common Metals **21**, 403(1970).
19. A.E. Dwight, R.A. Conner, Jr., J.W. Downey, Acta Cryst. **18**, 837 (1965).
20. S. Heatman, R.G. Haire, T. Le Bihan, A. Lindbaum, K. Litfin, Y. Méresse, and H. Libotte, Phys. Rev. Lett. **85**, 2961 (2000).
21. D. Hohnke and E. Parthé, Acta Cryst. **20**, 572 (1996).
22. J. Rodríguez-Carvajal, Physica B **192**, 55 (1993).
23. A. Mirmelstein et al., J. Alloys&Comp. **444-445**, 281 (2007).
24. V.R. Fanelli et al., J. Phys.: Condens. Matter **26**, 225602 (2014).
25. J. Aarts et al., Solid State Commun. **56**, 523 (1985).
26. E. Holland-Moritz and G.H. Lander, in *Handbook on the Phys. and Chem. of Rare Earths*, ed. by K.A. Gschneidner, Jr. and L. Eyring (North Holland, Amsterdam, 1994) Vol. 19, Ch. 130, 1.
27. V. Lazukov, P. Alekseev, E. Clementyev et al., Europhys. Lett. **33**, 141 (1996).
28. E.S. Ckementyev and A.V. Mirmelstein, JETP **109**, 128 (2009).
29. M. Loewenhaupt and K.H. Fischer, in *Handbook on the Phys. and Chem. of Rare Earths*, ed. by K.A. Gschneidner, Jr. and L. Eyring (North Holland, Amsterdam, 1993) Vol. 16, Ch. 105, 1.
30. A.P. Murani, S.J. Levett, and J.W. Taylor, Phys. Rev. Lett. **95**, 256403 (2005).

FIGURES

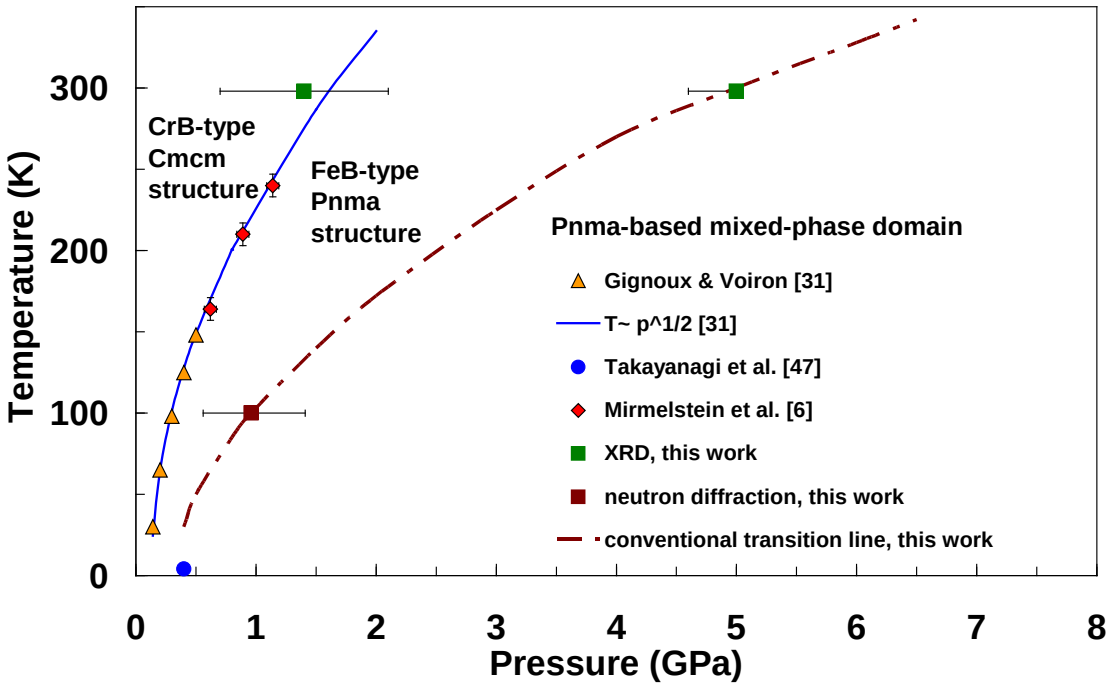

Figure 1. Approximate *P*-*T* phase diagram of CeNi as follows from the x-ray and neutron powder diffraction measurements. Green squares correspond to the room-temperature transitions from CrB (*Cmcm*) low-pressure to FeB (*Pnma*) high-pressure phase and the second transition to the *Pnma*-based mixed phase region (H′ phase). Yellow triangles and blue solid line represent the experimental data (magnetic measurements) and their approximation, respectively, from ref. 9. The results of magnetic measurements from ref. 11 and specific heat data from ref. 17 are shown by red rhombs and blue circle, respectively. Dashed-dotted line indicates the conventional transition line from the FeB-type of structure to the *Pnma*-based mixed phase state.

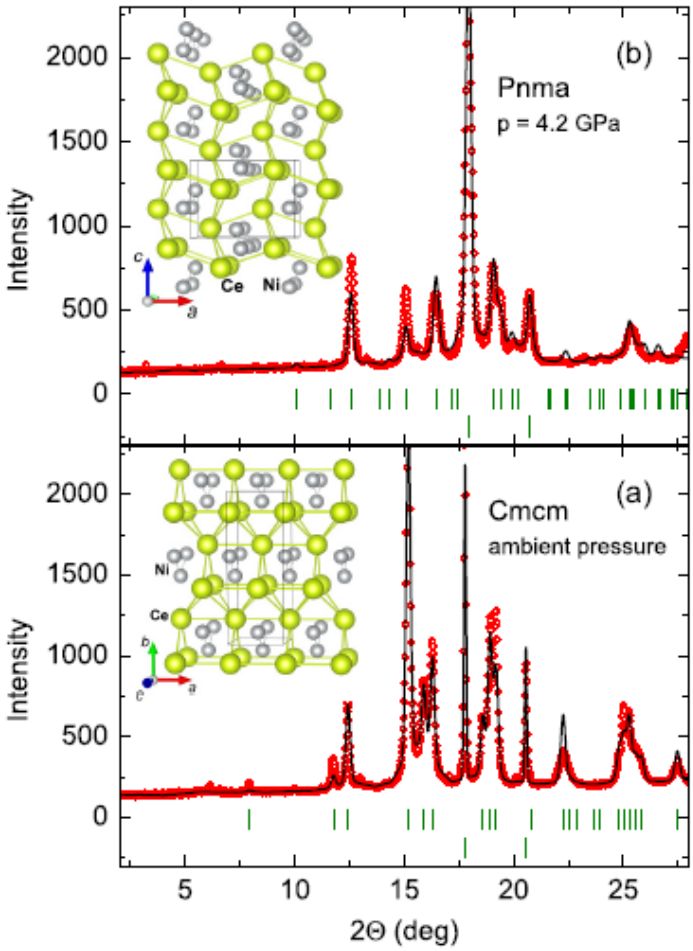

Figure 2. Powder diffraction data from CeNi at ambient pressure (a) and P = 4.2 GPa (b). The red circles are the measured scattering intensity, and the black solid line represents the Rietveld refinement fit to the data. The vertical bars indicate Bragg reflection positions of the main phase (top) and Au (bottom) used for pressure determination. The inserts show schematic view of the low pressure CrB-type (*Cmcm*) (a) and high pressure FeB-type (*Pnma*) (b) of the CeNi crystal structure.

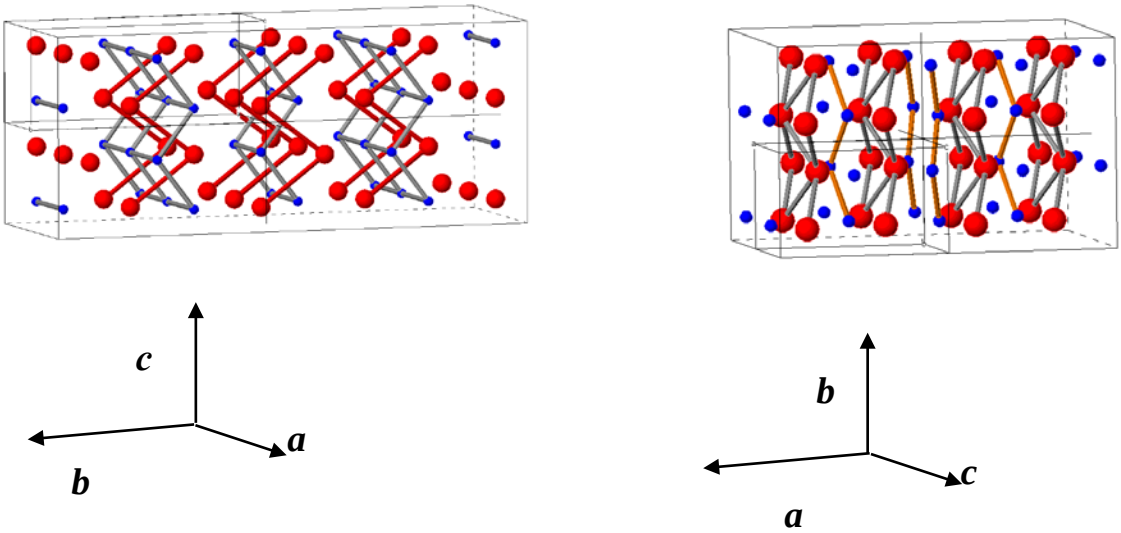

Figure 3. Left: CrB-type of the CeNi structure (C*mcm* space group); right: FeB-type of the CeNi structure (P*nma* space group). Ce ions are shown by red spheres and Ni ions by blue spheres. Arrows indicate the directions of crystal lattice axes.

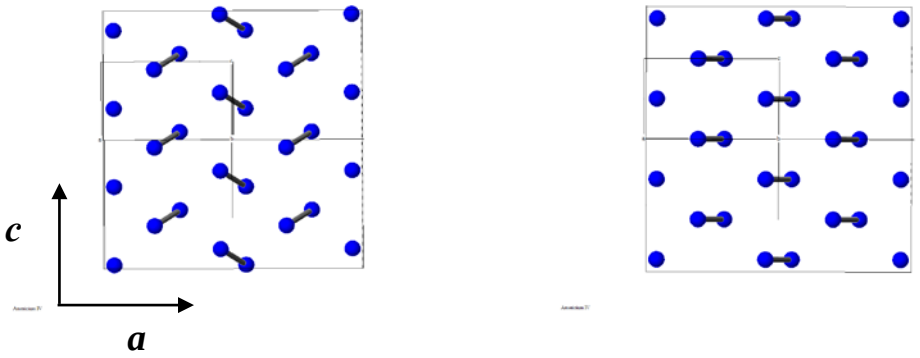

Figure 4. If the *z* value of the 4c sites in the *Pnma* structure (left) goes to zero, one obtains the higher-symmetry *Cmcm* structure (right) [20].

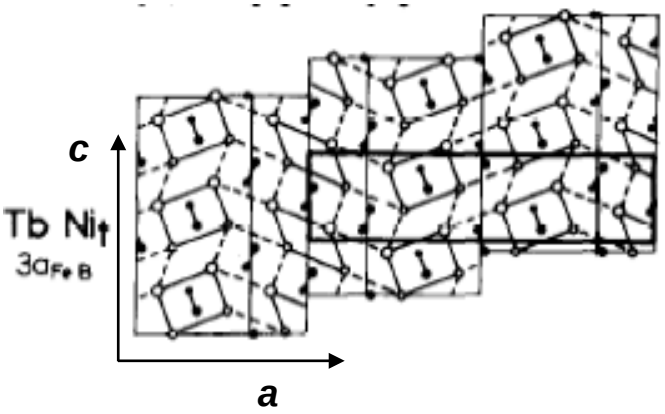

Figure 5. The (a,c) projection of the "3×a_{FeB}" structure with the crystal lattice parameters a_{TbNi}=3×a_{FeB}; b_{TbN}=b_{FeB}; c_{TbNi}=c_{FeB}. From ref. 18.

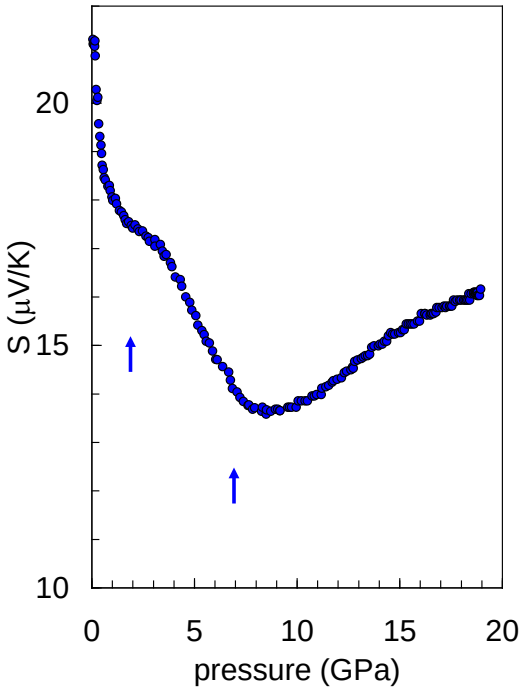

Figure 6. Thermopower of CeNi as a function of pressure at temperature 300 K (from ref. 23). Arrows indicate presumable locations of structural transitions.

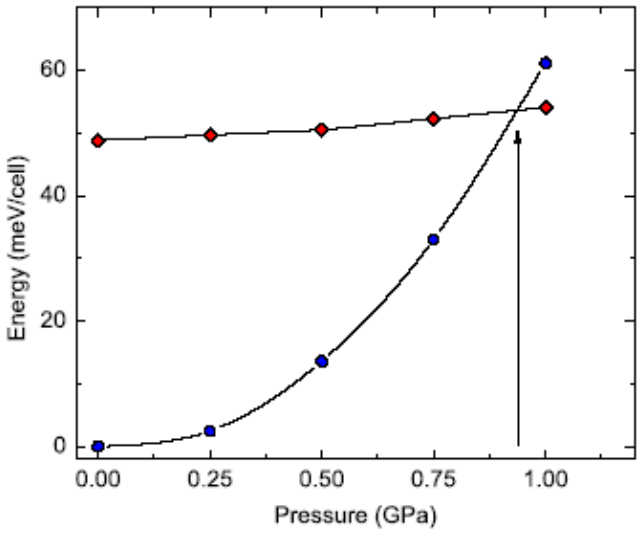

Figure 7. The relative energies as function of pressure for LP *Cmcm* (circles) and HP *Pnma* (diamonds) structure as obtained from DFT calculations. Arrow indicates the structural transition at pressure P =0.94 GPa.

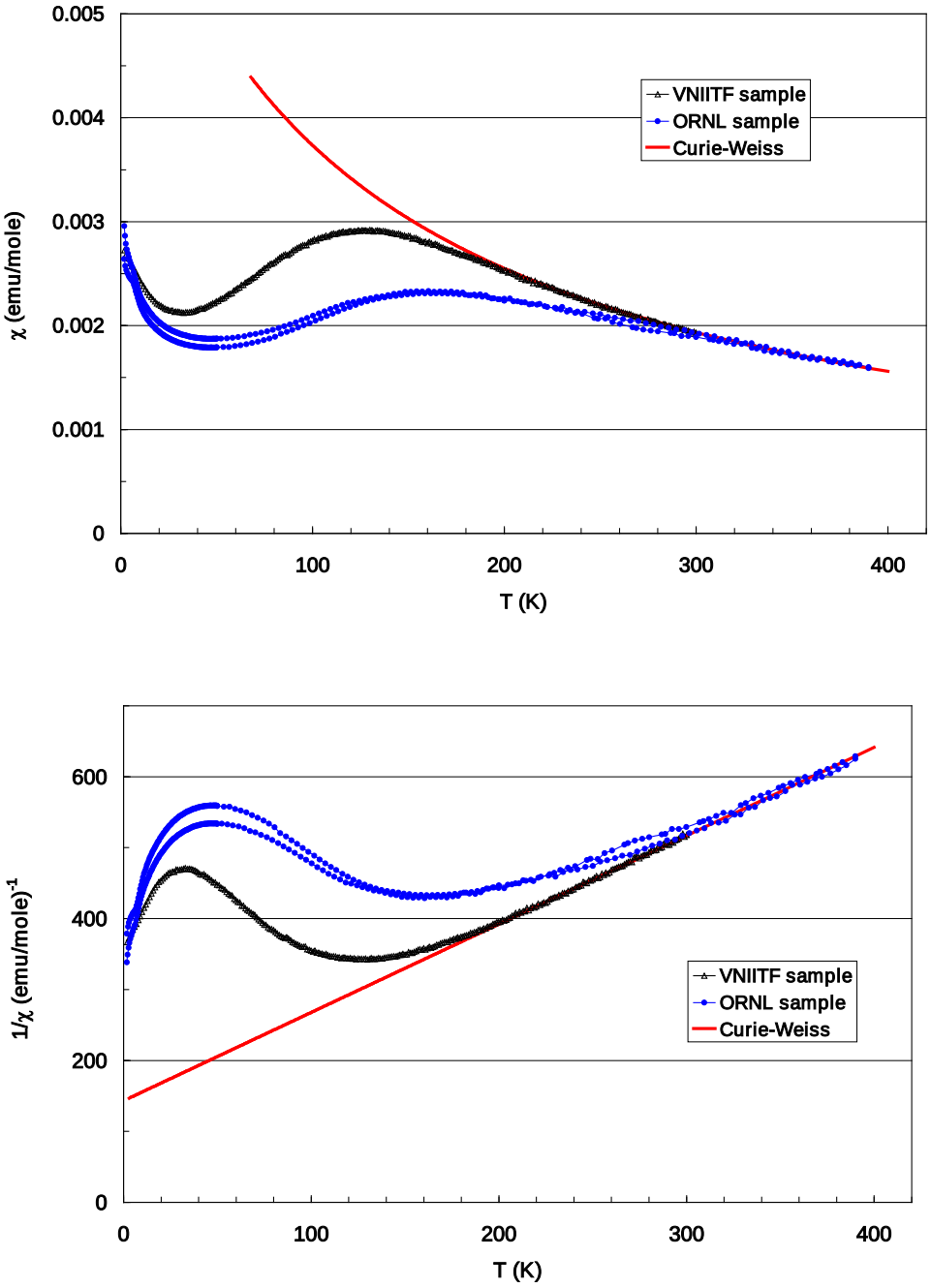

Figure 8. The magnetic susceptibility vs. temperature (top) and inverse magnetic susceptibility vs. temperature (bottom) for two powder samples of CeNi. Red curves correspond to the Curie-Weiss law with the effective magnetic moment of free Ce^{3+} ion $p = g[(J(J+1)]^2 = 2.53$. ORNL sample is prepared for the INS experiments using Ni^{60} isotope. VNIITF sample was prepared for magnetic measurements the results of which were published in ref. 11.

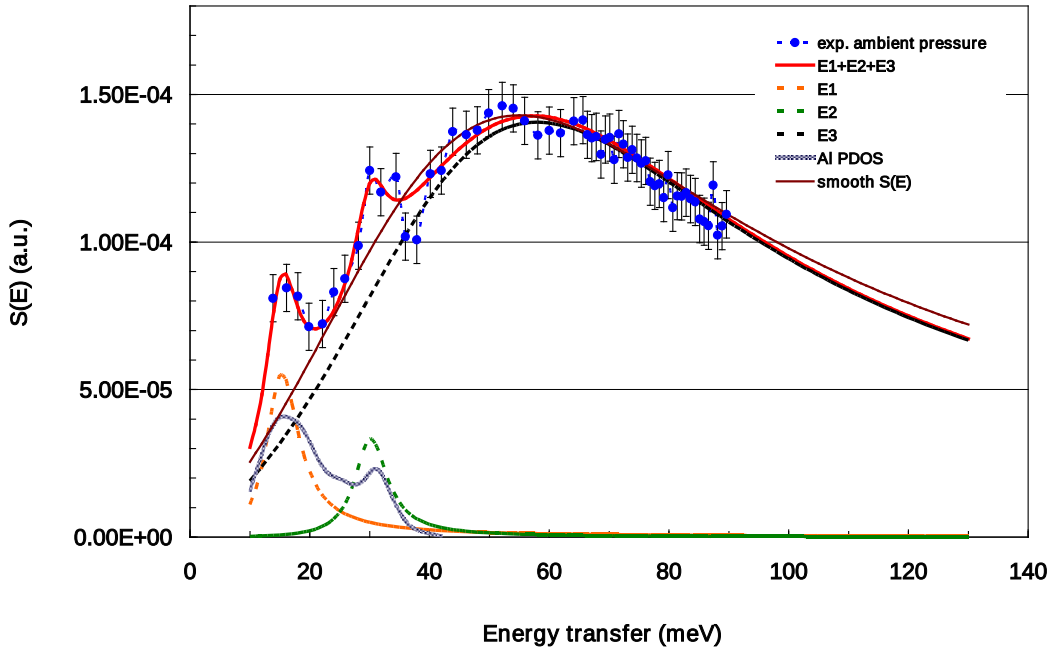

Figure 9. Magnetic scattering function $S_{mag}(E)$ for the $CeNi^{60}$ sample at T = 20 K and ambient pressure (blue circles). Dotted lines show a fit of the experimental magnetic spectrum by three inelastic Lorentz functions E_1, E_2, E_3 (see text). The sum of E_1, E_2, E_3 spectral contributions is shown by red curve. Solid brown curve demonstrates the "smooth" scattering function $S_{mag}(E)$ corresponding to a fit of the experimental points by a single Lorentzian neglecting the narrow spectral lines at 15 and 30 meV. Phonon density of states for aluminum (Al PDOS) is also shown.

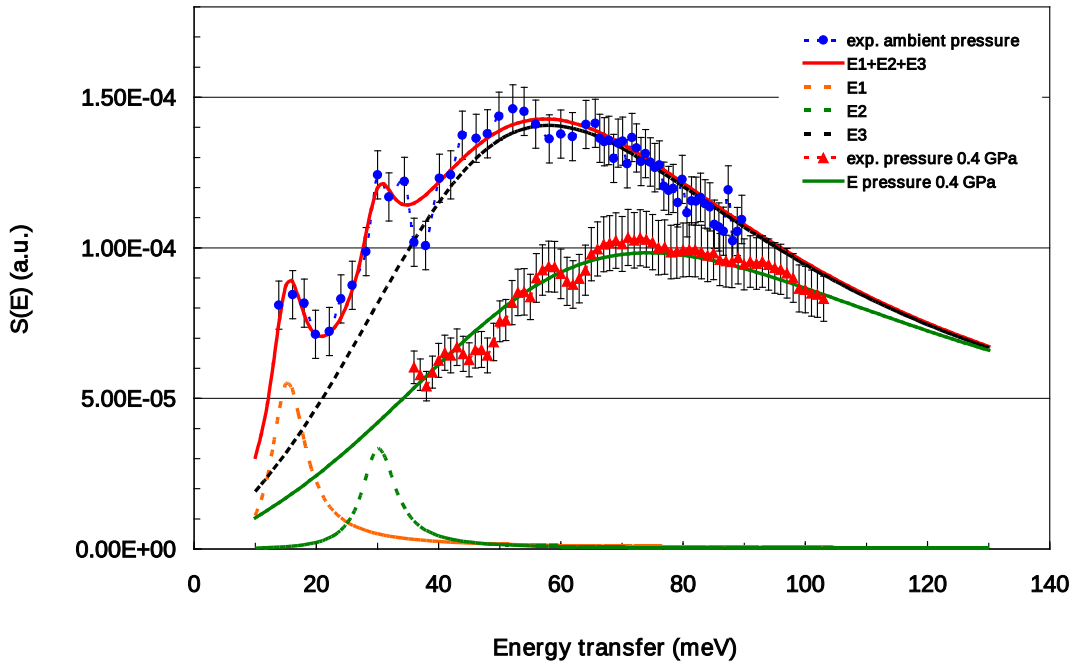

Figure 10. Magnetic scattering function of $CeNi^{60}$ при T = 20 K at ambient pressure (blue circles) and pressure of 0.4 GPa (red triangles), i.e. before and after the structural *Cmcm→Pnma* phase transition. Solid green line show a fit of the experimental magnetic spectrum by Lorentzian with the parameters given in the text.

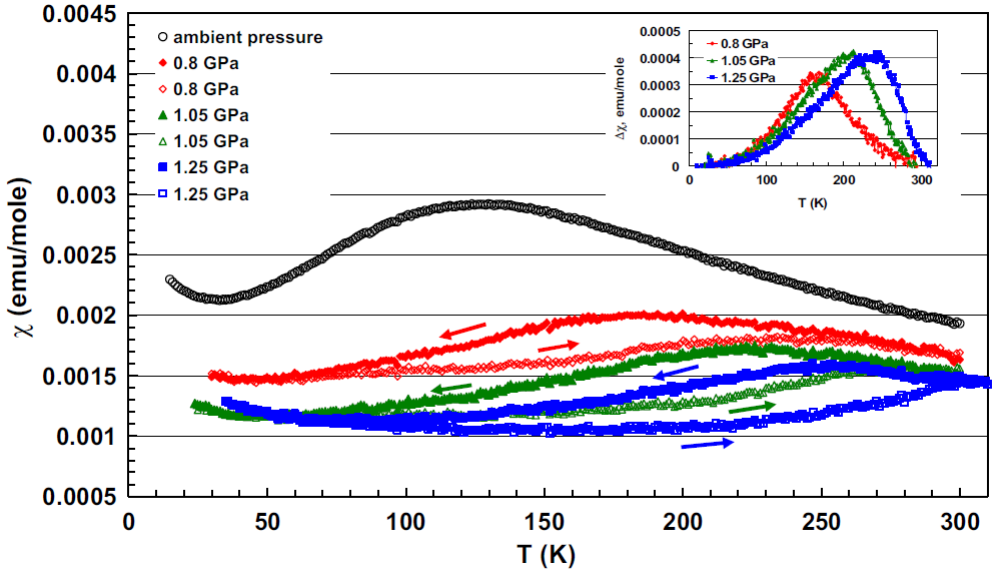

Figure 11. Temperature dependences of the CeNi magnetic susceptibility at ambient pressure and at the applied pressure P_{300K} = 0.8, 1.05, and 1.25 GPa [11]. Arrows indicate the temperature variation direction. Inset shows the difference curves $\Delta\chi(T) = \chi_{cooling}(T) - \chi_{heating}(T)$ as a function of temperature.

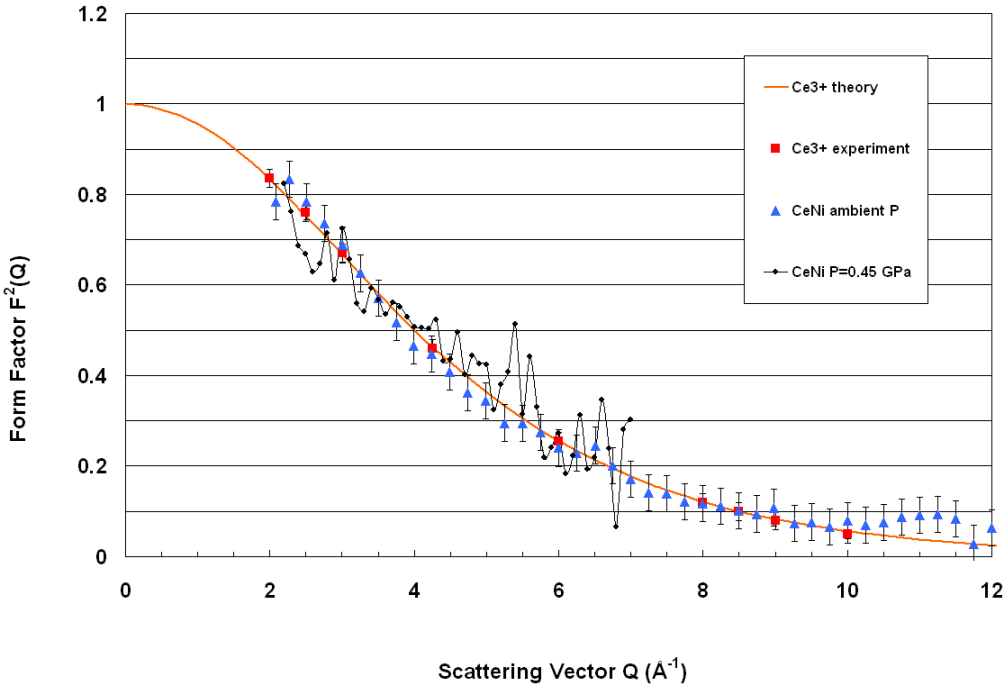

Figure 12. Magnetic form factor $F^2(Q)$ of CeNi before (blue triangles) and after (black circles) pressure-induced volume-collapse structural phase transition. The calculated form factor for the free Ce^{3+} and form factor measured experimentally for α-phase of metallic cerium [30] are shown for comparison.

D1

Upper critical field and pairing mechanism in the ferromagnetic superconductor UCoGe

B.WU[1], G.Bastien[1], D.Braithwaite[1], G. Knebel[1], M. Taupin[1,2], D. Aoki[1,3], J.Flouquet[1] and J.-P. Brison[1]

[1] Univ. Grenoble Alpes, INAC, Pheliqs, F-38000 Grenoble, France and CEA, INAC, Pheliqs, F-38000 Grenoble, France. E-mail: jean-pascal.brison@cea.fr
[2] TU Wien, Freihaus, Gelber Bereich, 8.OG Wiedner Hauptstraße 8-10 , 1040 Wien, Österreich
[3] Institute for Materials Research, Tohoku University, Oarai, Ibaraki 311-1313, Japan[1] Univ. Grenoble Alpes, INAC, Pheliqs, F-38000 Grenoble, France and CEA, INAC, Pheliqs, F-38000 Grenoble, France
[2] TU Wien, Freihaus, Gelber Bereich, 8.OG Wiedner Hauptstraße 8-10 , 1040 Wien, Österreich
[3] Institute for Materials Research, Tohoku University, Oarai, Ibaraki 311-1313, Japan

In the three uranium-based ferromagnetic superconductors (UGe_2, URhGe, UCoGe), which are all orthorhombic, the behavior of the upper critical field is anomalous, revealing notably a reinforcement of superconductivity under magnetic field (**H**), unusual upward curvatures, and a strong anisotropy.

We present here our study of the upper critical field (H_{c2}) of UCoGe. At ambient pressure, H_{c2} has been obtained by thermal conductivity measurements and by electrical transport, along the three crystallographic directions. Under pressure, it has been measured along the easy magnetization c-axis by electrical transport, up to 10.5GPa.

Reinforcement of superconductivity for **H**//**b** (S-shape) appears even more strongly on bulk (thermal transport) measurements than on resistivity measurements [1]: for fields above 8T along the b axis, bulk superconductivity appears at a higher temperature than observed on resistivity measurements? This is reminiscent of observations on cuprates High-Tc superconductors, where it was taken as a demonstration of the existence of a (resistive) vortex-liquid phase.

But the behavior of H_{c2} is also completely anomalous for fields along the c-axis: the quasi 2D anisotropy, the upward curvature of H_{c2} down to the lowest temperatures, the opposite evolution of the critical temperature and the initial slope of H_{c2} under pressure, cannot fit in the framework of an upper critical field controlled by orbital and paramagnetic limitations.

We show instead that, as suggested by various theoretical works on ferromagnetic superconductors, (see theory of V. Mineev [2], and model of Y. Tada [3]), these results strongly support a magnetic field dependence of the pairing mechanism: all anomalies are consistently understood with a simple field dependence of the pairing strength. The validity of the model is further checked by specific heat measurements under field. It points out the major role of ferromagnetic fluctuations in the pairing mechanism in UCoGe.

References

[1] D. Aoki, T.D. Matsuda, V. Taufour, E. Hassinger, G. Knebel, and J. Flouquet, *J. Phys. Soc. Jpn.* **78**, 113709 (2009).
[2] V. P. Mineev, *Phys. Rev. B* **83**, 064515 (2011)
[3] Y. Tada, S. Fujimoto, N. Kawakami, T. Hattori, Y. Ihara, K.Ishida, K. Deguchi, N. K. Sato, and I. Satoh, *Journal of Physics: Conference Series* **449,** 012029 (2013)

D2

Post-transition metal, metalloid and isotopic doping in $PuCoGa_5$

E. Colineau,[1] P. Boulet[2], J.-C. Griveau[1], R. Eloirdi[1], J. Rebizant[1], F. Wastin[1*], A.B. Shick[3], R. Caciuffo[1]

[1]*European Commission, Joint Research Centre (JRC), Institute for Transuranium Elements (ITU), Postfach 2340, 76125 Karlsruhe, Germany, email: eric.colineau@ec.europa.eu*
[*]*Present address: European Commission, Joint Research Centre, Institute for Energy and Transport, P.O. Box 2, 1755 ZG Petten, The Netherlands*
[2]*Institut Jean Lamour, UMR 7198 CNRS-Université de lorraine, Parc de Saurupt, 54011 Nancy cedex, France*
[3]*Institute of Physics, ASCR, Na Slovance 2, CZ-18221 Prague, Czech Republic*

In previous studies [1-5], the lattice parameters and electronic structure of the $PuCoGa_5$ superconductor have been tuned by applied pressure and chemical substitution. Under applied pressure, the critical temperature, T_c, is enhanced while any chemical substitution of plutonium in $Pu_{1-x}An_xCoGa_5$ (An = U, Np and Am) or of cobalt in $PuCo_{1-x}T_xGa_5$ (T = Rh, Fe, Ni), leads to a decrease of T_c. Gallium substitution effects have not been reported yet, except the unique case of the fully substituted $PuCoIn_5$, and is presented here.

Figure 1 shows the effect on the critical temperature T_c and the lattice parameters ratio c/a of applied pressure [1] and substitution of plutonium [2-4], cobalt [2] and gallium (this work). The figure also includes T_c and c/a values for fully substituted compounds such as $NpCoGa_5$ (not superconducting down to 0.4K) of $AmCoGa_5$ (T_c = 1.9K) [5].

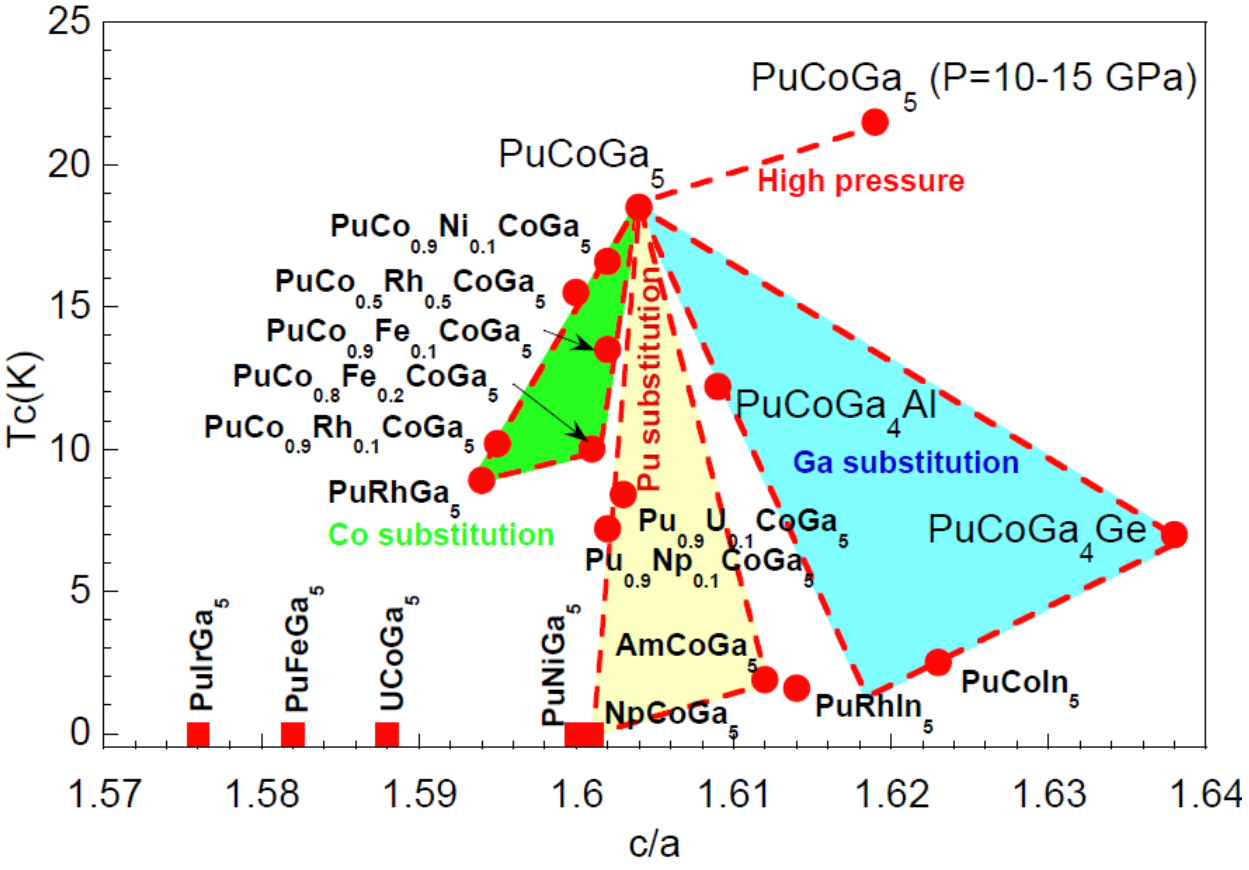

Fig. 1. critical temperature T_c and lattice parameters ratio c/a for different compounds related to $PuCoGa_5$: Co-substituted (green area), Pu-substituted (yellow area) and Ga-substituted (blue area). Circles indicate superconducting compounds, whereas squares denote compounds where no superconductivity was detected down to the lowest experimental temperature (typically 2K).

.

The figure clearly shows that plutonium substitution does not affect much the c/a ratio, but dramatically decreases the critical temperature. Cobalt substitution reduces both the c/a ratio and the critical temperature, the latter being less dramatically affected than by Pu-substitution. Finally, gallium substitution increases significantly the c/a ratio while significantly decreasing the critical temperature. We conclude that the c/a ratio - at least its fine tuning around its value for $PuCoGa_5$ - does not appear to be a key parameter for superconductivity in this system. On the contrary, electronic structure calculations (this work) suggest that the variation of the critical temperature in Co-substituted compounds is connected to the change of the Fermi surface.

In this presentation, we will report on gallium substitution by aluminum, germanium, and tin, as well as isotopic substitution (^{69}Ga by ^{71}Ga) and discuss the relation between the critical temperature and the c/a ratio (crystallographic structure), the molar mass (isotopic effect) and the Fermi surface (electronic structure), respectively.

References

[1] J.-C. Griveau, C. Pfleiderer, P. Boulet, J. Rebizant and F. Wastin, J. Magn. Magn. Mater**. 272-276**, 154 (2004).
[2] P. Boulet, E. Colineau, F. Wastin, J. Rebizant, P. Javorský, G. H. Lander and J.D. Thompson, Phys. Rev. **B 72**, 104508 (2005)
[3] J.-C. Griveau, J. Rebizant, F. Wastin, E. Colineau, F. Jutier and G.H. Lander, Materials Research Society Symp. Proc. **Vol. 893** (2006).
[4] P. Javorský, F. Jutier, P. Boulet, F. Wastin, E. Colineau, J. Rebizant, Physica **B 378-380**, 1007 (2006).
[5] J.-C. Griveau and E. Colineau, C.R. Physique **15**, 599-615 (2014).

D3

Thermal expansion of the heavy-fermion superconductor $PuCoGa_5$

R. Eloirdi[1], N. Magnani[1], C. Giacobbe[2], P. Amador[1], G. H. Lander[1], R. Caciuffo[1]

[1]*European Commission, Joint Research Centre (JRC), Institute for Transuranium Elements (ITU), Postfach 2340, 76125 Karlsruhe, Germany, email: rachel.eloirdi@ec.europa.eu*
[2]*European Synchrotron Radiation Facility, 38043 Grenoble, France*

$PuCoGa_5$ has the highest T_c (18.5 K) of any heavy-fermion superconductors. Twelve years after its discovery our understanding of this material remains at best confused. The presence of valence fluctuations has been recently suggested by resonant ultrasound spectroscopy [1]. To address this point, we have performed high-resolution x-ray diffraction measurements on an encapsulated powder sample [2] of $^{242}PuCoGa_5$ (right inset of Figure 1). The sample has been prepared as single crystal (left inset of Figure 1) by the self-flux method using a charge of 242-plutonium metal obtained by an amalgamation process [3].

The x-ray diffraction patterns measured from 300 K to 5 K (Figure 1) show that the tetragonal symmetry is preserved down to 5 K. The c/a ratio decreases with increasing T to become almost constant above ~150 K. The volume thermal expansion coefficient αV has a jump at Tc, a factor ~20 larger than the change predicted by the Ehrenfest relation. As a consequence, the volume expansion (Figure 2) deviates from the curve expected for the conventional anharmonic behaviour described by a simple Grüneisen-Einstein model (inset of Figure 2). The observed differences are about ten times larger than the statistical error bars.

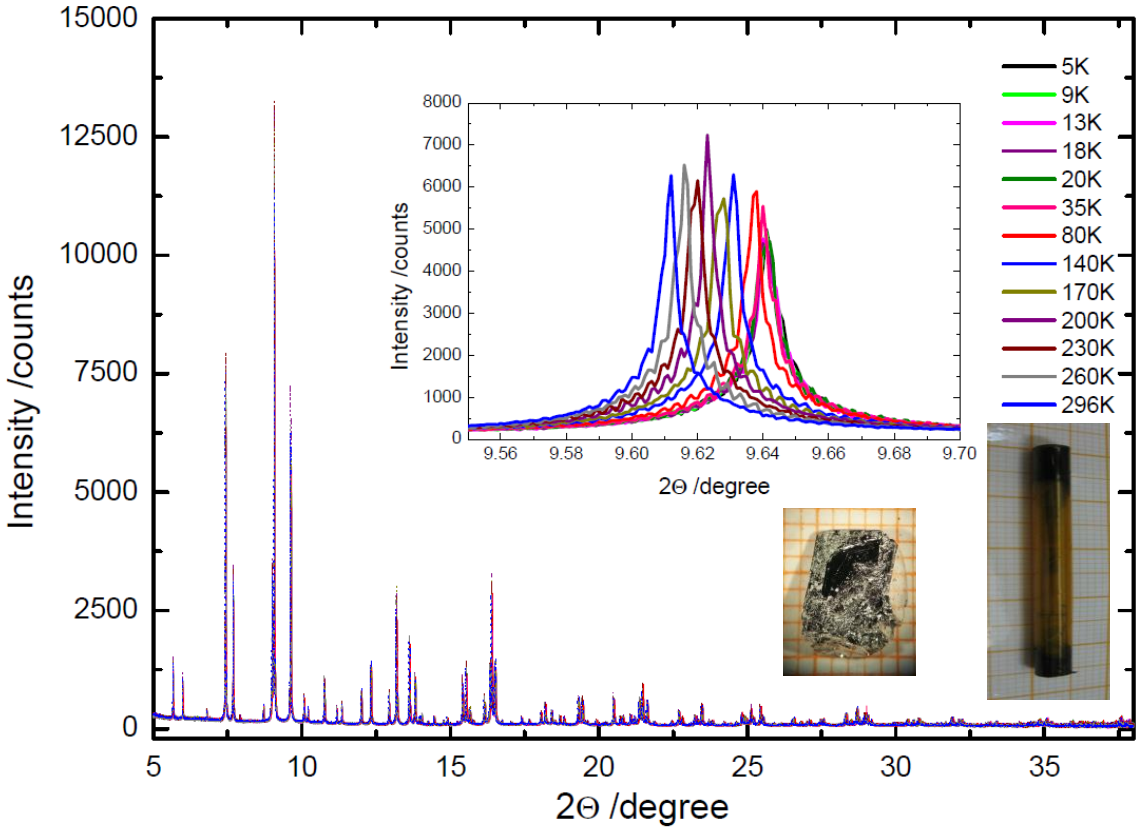

Fig. 1. X-ray diffraction patterns versus temperature of $^{242}PuCoGa_5$ powder sample. Inset: (left) photo of the $^{242}PuCoGa_5$ single crystal obtained by self-flux before being crushed: (right) picture of the encapsulated powder $^{242}PuCoGa_5$ sample embedded in resin.

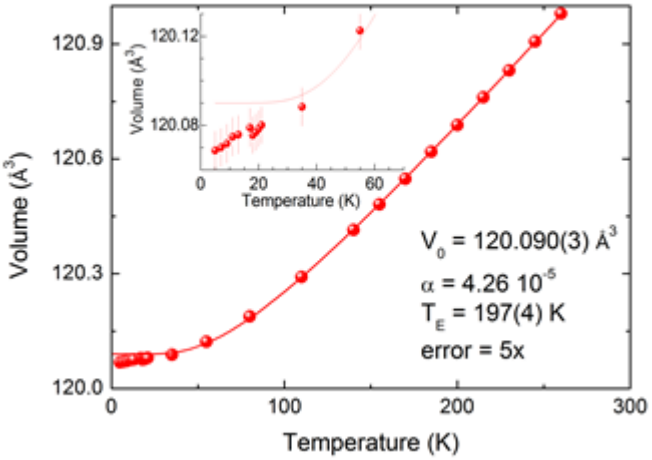

Fig. 2. Thermal volume expansion of $^{242}PuCoGa_5$. Experimental data are shown by symbols, whilst the solid line represent a fit to the Grüneisen-Einstein model. Inset: expansion of the low-temperature region highlighting the deviation of the measured data from the model curve.

References

[1] B. J. Ramshaw et al., PNAS **112**, 3285 (2015).
[2] A. H. Hill, T. Klimczuk, R. Springell and H. C. Walker, *J. Appl. Cryst.* **46**, 567-569 (2013).
[3] Y. Shiokawa, K. Hasegawa, K. Konashi, M. Takahashi, K. Suzuki, J. Alloys Comp. **255**, 98 (1996).

D4

X-ray circular magnetic dichroism of the superconductor $PuCoGa_5$

F. Wilhelm1, N. Magnani2, R. Caciuffo1, R. Eloirdi2, A. Rogalev1 and G. H. Lander
1ESRF, Grenoble, France, 2EU, JRC, Institute for Transuranium Elements, Germany

We have used XMCD at the ESRF ID12 beamline to examine PuCoGa5 (Tc = 18 K) between 2 and 30 K. The signal is small requiring the application of an applied field of 17 T to observe the induced moment of 0.03 μB. Because of the large penetration depth (~ 250 nm) and small superconducting coherence length (~ 2 nm) the XMCD probes the normal state even below Tc. The spectral form does not change as a function of temperature and the narrow linewidths show that the signal is similar to that observed in localized Pu materials. The ratio R = μL/μS is found to be –1.7(2), in good agreement with recent theory (–1.74), and different from the localized 5f5 value of –1.40. An interesting 25% rise of the local susceptibility appears below ~ 10 K, suggesting the presence of a local moment at the Pu site.

Email of presenting author: wilhelm@esrf.fr

Long abstract: was not submitted

E1

A New Approach for Radiation Damage Studies by Incorporation of Dilute Self-Irradiating Defects in Thin Films

Eyal Yahel, Tzvi Tempelman, Michael Shandalov, Michael Schmidr, Itzhak Kelson and uval Golan
NRCN

We present a model system for the study of radiation damage in non-radioactive materials. The method is based on homogeneous incorporation ^{228}Th ions in PbS thin films using a small volume chemical bath deposition (CBD) technique. Controlled doping of the thin films with minute amounts of radioactive elements such as thorium is expected to provide a unique path for studying radiation damage in materials.
The ^{228}Th-doped films were characterized using XRD, indicated a single phase material. EDS, XPS depth profiles and a-autoradiography indicated that the Th ions were homogeneously distributed throughout the films, suggesting Pb substitution by Th ions in the crystal lattice. The properties of the PbS(^{228}Th) film activity and isotope distribution were investigated by using a-spectroscopy and g-spectroscopy. The measurements were performed using PL spectroscopy, where band-to-band and defect states emissions were monitored.

Email of presenting author: eyalyahel@gmail.com

Long abstract: was not submitted

E2

Using diffraction tomography to chemically characterise and spatially locate the corrosion products of uranium metal encapsulated in cement grout under different storage conditions

N. Harker, J. Wright, T. Scott, & C. Stitt
ESRF

High energy x-rays provide an excellent means of characterising the heterogeneous nature of materials, allowing undestructive and in-situ observation of processes occurring in the subsurface. The high energy x-ray source of beamline ID11 at the European Synchrotron (ESRF) was used to characterise 2 uranium metal samples encapsulated in cement grout that had been keep under different storage conditions (under water, and under water after hydrogen exposure). The results allowed 3D reconstruction of the sample volume and 2d spatial location and phase determination of the resulting corrosion products.

Email of presenting author: harker@esrf.fr

Long abstract: was not submitted

E3

Purification of uranium hexafluoride by magnesium fluoride

Jean-Michel Hiltbrunner, Marc Dubois, Laurent Jouffret, Bertrand Morel, Ania Selmi
ICCF - Areva NC

Magnesium fluoride is well known as a catalyst in industrial applications [1]. However, this paper will present an original use for MgF_2 in nuclear fuel cycle [2]. Before its isotopic enrichment, uranium is chemically treated in order to produce uranium hexafluoride. This uranium contains some impurities which are fluorinated and needed to be removed. One of the fluorine pollutants which have to be removed is vanadium oxifluoride, a volatile compound.
High specific surface MgF_2 is produced by solvothermic methods [3]. Due to this way of synthesis, hydroxyls groups remain in the final product. A post-fluorination treatment is required in order to adjust the O/F ratio. Pellets are exposed to VOF_3 in a sealed bottle and characterizations (XRD, FTIR and NMR) are performed in order to determine the mechanism involved. These analyses conclude that OH groups are active sites during sorption process and that MgF_2 is an efficient material to remove VOF_3 from UF_6.

Email of presenting author: jean-michel.hiltbrunner@areva.com

Long abstract: was not submitted

E4

Evaluating laser-driven bremsstrahlung radiation sources for imaging and analysis of nuclear waste packages

Christopher P. Jones*[1], Ceri M. Brenner[2], Camilla A. Stitt[1], Chris Armstrong[2,3], Dean R. Rusby[2,3], Seyed R. Mirfayzi[4], Lucy A. Wilson[2], Aarón Alejo[4], Hamad Ahmed[4], Ric Allott[2], Nicholas M. H. Butler[3], Robert J. Clarke[2], David Haddock[2], Cristina Hernandez-Gomez[2], Adam Higginson[3], Christopher Murphy[5], Margaret Notley[2], Charilaos Paraskevoulakos[1], John Jowsey[6], Paul McKenna[3], David Neely[2], Satya Kar[4], Thomas B. Scott[1]

[1]*Interface Analysis Centre, HH Wills Physics Laboratory, Tyndall Avenue, Bristol, BS8 1TL, UK*
[2]*Central Laser Facility, STFC, Rutherford Appleton Laboratory, Didcot, Oxon, OX11 0QX, UK*
[3]*Department of Physics, SUPA, University of Strathclyde, Glasgow G4 0NG, UK*
[4]*Centre for Plasma Physics, Queen's University Belfast, Belfast BT7 1NN, UK*
[5]*Department of Physics, University of York, York YO10 5DD, UK*
[6]*Ground Floor North B582, Sellafield Ltd, Seascale, Cumbria CA20 1PG,*
[*]*email presenting author: cj0810@bristol.ac.uk*

A small scale sample nuclear waste package, consisting of a 28mm diameter uranium penny encased in grout, was imaged by absorption contrast radiography using a single pulse exposure from an x-ray source driven by a high-power laser. Radiography was carried out utilising x-ray pulses generated during laser-solid interactions with the Vulcan laser at the Rutherford Appleton Laboratory, Harwell Campus. P-polarised, 1054nm wavelength pulses[1] of 10 picoseconds duration delivered ~150J of laser energy onto 100µm thick tantalum foil targets at a 20° angle of incidence. In the current set-up, the Bremsstrahlung energy spectrum peaked at 200keV, above which the photon flux logarithmically decreased. During imaging, spectrometer measurements indicated an x-ray beam with a bulk temperature of ~600keV[2].

BAS-TR and BAS-SR image plates were used for image capture, alongside a newly developed Thallium doped Caesium Iodide scintillator-based detector coupled to CCD chips. The uranium penny was clearly resolved to sub-mm accuracy over a 30cm^2 scan area (Figure 1) from a single shot acquisition. In addition, neutron generation was demonstrated in situ with the x-ray beam, with a single shot, thus demonstrating the potential for multi-modal criticality testing of waste materials. This feasibility study successfully demonstrated non-destructive radiography of encapsulated, high density, nuclear material. With recent developments of high-power laser systems, to 10Hz operation, a laser-driven multi-modal beamline for waste monitoring applications is envisioned.

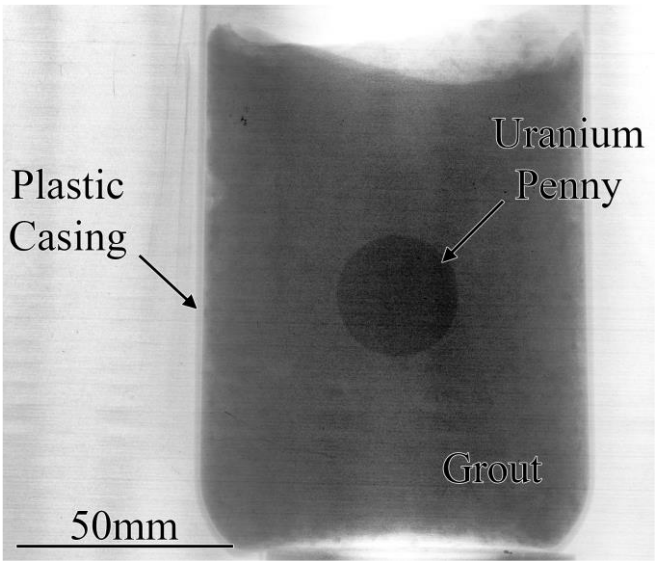

Fig. 1. Raw signal from a single pulse exposure radiograph of the whole sample using no filters in front of an image plate detector (IP). The outline of the plastic container, cement and uranium penny are clearly shown.

References

[1] C. Hernandez-Gomez, P. Brummitt, D. Canny, et al, Vulcan petawatt operation and development, J. Phys. IV France 133 (2006) 555-559

[2] C. M. Brenner, S. R. Mirfayzi, D. R. Rusby, et al, Laser-driven x-ray and neutron source development for industrial applications of plasma accelerators, Plasma Physics and Controlled Fusion 58 (1) (2016) 1

E5

A new X-ray emission spectrometer at the Rossendorf beamline for studying nuclear materials

Kristina O. Kvashnina[1,2] and Andreas C. Scheinost[1,2]

[1] *Rossendorf Beamline at ESRF - The European Synchrotron, CS40220, 38043 Grenoble Cedex 9, France.*
[2]*Helmholtz-Zentrum Dresden-Rossendorf (HZDR), Institute of Resource Ecology, P.O. Box 510119, 01314, Dresden, Germany. email:kristina.kvashnina@esrf.fr*

This contribution will give an overview of the new Johann-type X-ray emission spectrometer recently installed and tested at the Rossendorf Beamline (ROBL) of the European Synchrotron Radiations Facility (ESRF) [1]. The spectrometer is constructed for studying nuclear materials and environmental applications by high energy resolution fluorescence detection (HERFD) X-ray absorption spectroscopy (XAS) [2], X-ray emission spectroscopy (XES) [3] and resonant inelastic X-ray scattering (RIXS) techniques [4]. As an example we will show the studies of the electronic structure of several systems by means of XAS, XES and RIXS. The experimental results are analysed using theoretical approximation based on the ground state electronic density.

References

[1] K. O. Kvashnina and A. C. Scheinost, J. Synchrotron Radiat. **submitted**, (2016).
[2] K. O. Kvashnina, S. M. Butorin, P. Martin, and P. Glatzel, Phys. Rev. Lett. **111**, 253002 (2013).
[3] K. O. Kvashnina, Y. O. Kvashnin, and S. M. Butorin, J. Electron Spectros. Relat. Phenomena **194**, 27 (2014).
[4] K. O. Kvashnina, Y. O. Kvashnin, J. R. Vegelius, A. Bosak, P. M. Martin, and S. M. Butorin, Anal. Chem. **87**, 8772 (2015).

E6

Inelastic X-ray scattering studies of actinides

Andrew Walters[1], Helen Walker[2], Roberto Caciuffo[3], Tomasz Klimczuk[4] and Ke-Jin Zhou[1]

[1] *Diamond Light Source, Didcot, OX11 0DE, UK, e-mail: andrew.walters@diamond.ac.uk*
[2] *ISIS Facility, Harwell Campus, Didcot, OX11 0QX, UK*
[3] *Institute for Transuranium Elements, European Commission, D-76125 Karlsruhe, Germany*
[4] *Faculty of Applied Physics and Mathematics, Gdansk University of Technology, 80-233 Gdansk, Poland*

The huge improvement in the energy resolution of inelastic x-ray scattering (IXS) spectrometers in recent years has enabled novel science to be studied using this technique. Up to now the majority of resonant inelastic x-ray scattering (RIXS) studies have been devoted to cuprates and iridates, due in part to experimental limitations. With the advent of the next generation of RIXS beamlines, including ID32 at the ESRF, SIX at NSLS-II and I21 at Diamond Light Source (DLS), there will be both the capability and the capacity for many new avenues of condensed matter physics research. Here we present non-resonant IXS measurements of the phonon density of states of $NpFeAsO_xF_{1-x}$ [1]. This material is a structural analogue of a family of superconducting pnictides, but does not superconduct with fluorine doping, unlike its rare-earth counterparts (see Fig. 1). Our measurements found no phonon renormalisation upon F-doping, in contrast to previous IXS studies on NdFeAsO [2] and SmFeAsO [3], both of which become high-temperature superconductors with F-doping.

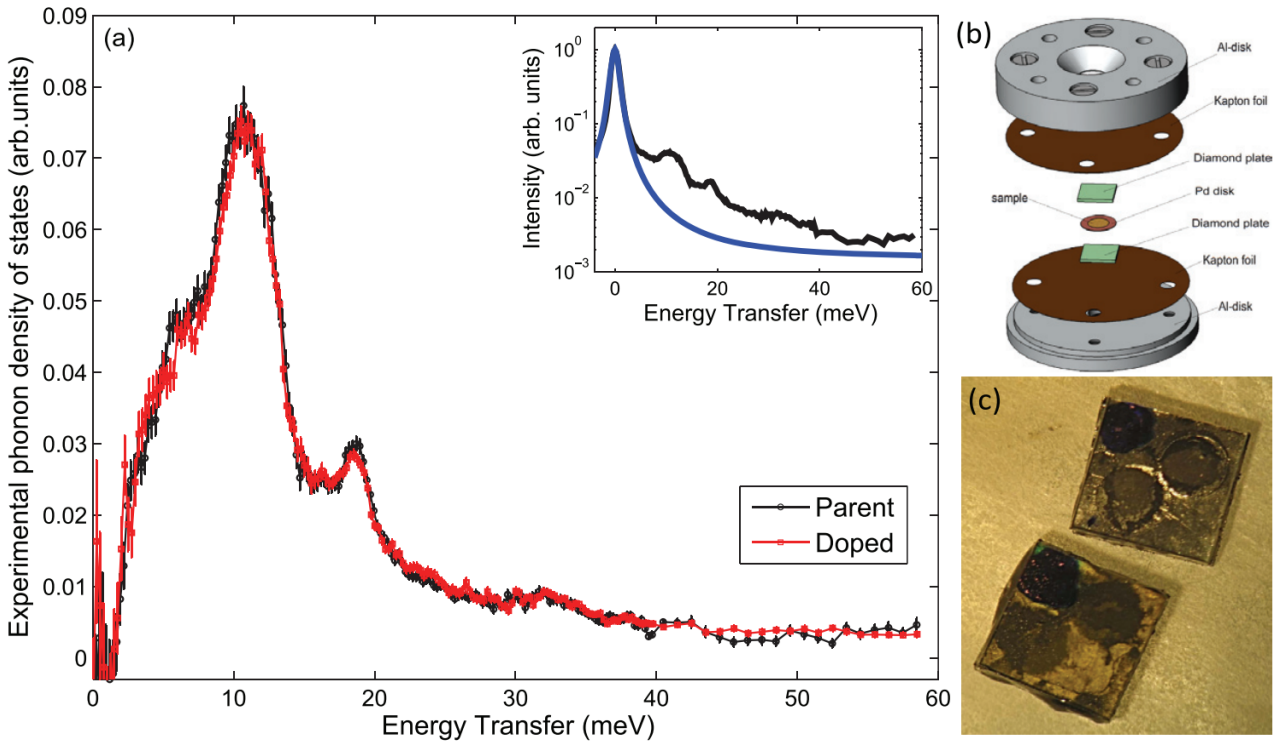

Fig. 1. (a) The experimental phonon density of states of NpFeAsO and F-doped NpFeAsO are shown in black and red respectively. (b) The sample holder used in the inelastic x-ray scattering measurements is presented in an exploded view. (c) A photo is shown of the powder samples, sandwiched inside the two single-crystal diamond plates.

The design and current status of the I21 soft x-ray RIXS beamline at DLS will also be described, and an overview of future applications of RIXS in the study of actinides will be discussed [4,5].

References

[1] A.C. Walters et al., *Journal of Physics: Condensed Matter* **27**, 325702 (2015).
[2] M. Le Tacon et al., *Physical Review B* **78** 140505 (2008).
[3] M. Le Tacon et al., *Journal of Physics and Chemistry of Solids* **72** 523 (2011).
[4] L. A. Wray et al., *Physical Review Letters* **114** 236401 (2015).
[5] K. O. Kvashina et al., *Journal of Electron Spectroscopy and Related Phenomena* **194** 27 (2014).

F1

Uranium sorption on mixtures based on alumina nanoparticles and smectite clay colloids

Natalia Mayordomo, Ursula Alonso and Tiziana Missana

CIEMAT, Av Complutense 40, 28040 Madrid, Spain e-mail: natalia.mayordomo@ciemat.es

Uranium is an actinide that can be found in natural environments, in mining and in nuclear waste. As hazardous specie, it is an issue of major concern to evaluate its immobilization on natural materials with sorbent capabilities, such as clays or oxides.

Bentonite clay fulfils the requirements to retard pollutants on its surface: it is a material with very low hydraulic conductivity with swelling and good sorbent properties; therefore it has been proposed as buffer material in nuclear waste repositories [1].

In this study we analysed if the addition of alumina nanoparticles may improve uranium retention in a bentonite barrier and under what conditions. Aluminium oxide has high surface area and amphoteric behaviour with high point of zero charge that could enhance uranium sorption in a wider range of pH conditions.

The retention of U(VI) has been studied under atmospheric conditions on Na-smectite colloids (FEBEX bentonite [2]) and alumina nanoparticles and mixtures of these sorbents in different weight proportions.

Figure 1a shows uranium sorption on independent Na-smectite and alumina (1g/L) systems in $NaClO_4$ 0.1 M at different pH. It can be seen that under these conditions above pH 4.5, alumina sorbs uranium more efficiently: at pH 6 uranium sorption in alumina is almost quantitative and in Na-smectite is about 90%. On the other hand below pH 4.5, possibly due to cationic exchange, the adsorption on smectite is higher.

Therefore the addition of alumina to Na-smectite is expected to improve uranium sorption in the range of neutral and alkaline pH.

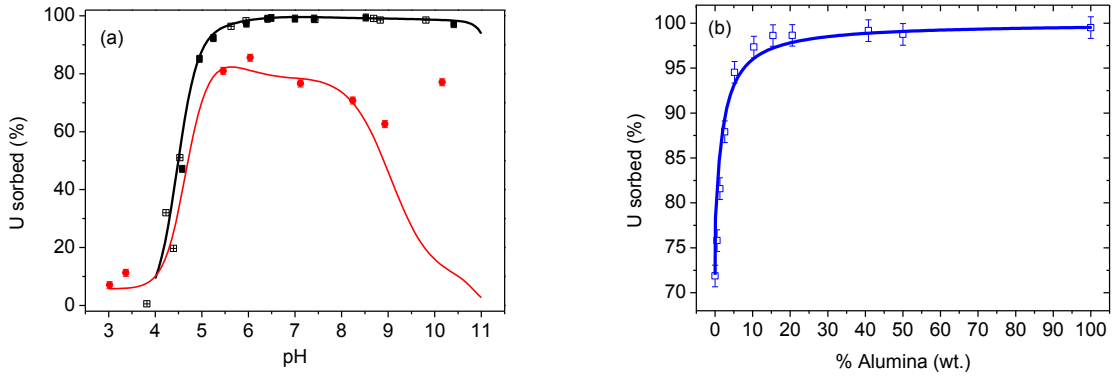

Figure 1. (a) Percentage of U(VI) sorbed in 0.1 M $NaClO_4$ under atmospheric conditions at different pH onto: (●)100% NaSmectite and (■)100% Alumina. (b) Percentage of uranium sorbed on Na-smectite and alumina mixtures at pH 7.5. [U]=$4 \cdot 10^{-7}$ M. Simulations are plotted as continuous lines.

Sorption experiments with varying mixture weight proportion were carried out at pH 7.5 and results are shown in Figure 1b. It is observed that sorption in mixtures increases with increasing the amount of alumina and it is noteworthy that only a 10 % of alumina is enough to reach 100 % of uranium sorption approximately.

To describe the uranium sorption on independent systems and to simulate the behaviour of mixed systems, non-electrostatic surface complexation model is proposed using the NEA thermodynamic database [3].

That model used for both alumina and Na-smectite was similar, including UO_2^{2+} and UO_2OH^+ complexation in surface SOH sites and for the Na-smectite cationic exchange was considered as well [4]. In presence of CO_2, the model underestimated the experimental sorption for pH > 6, therefore, the sorption of uranyl carbonate complexes was taken into account to explain the experimental behaviour under alkaline conditions.

The models developed for the independent systems were able to explain and predict uranium sorption in the mixed systems, indicating the systems are additive.

References

[1] R. Dohrmann, S. Kaufhold, B. Lundqvist, the role of clays for safe storage of nuclear waste, in: F. Bergala, G. Lagaly (Eds.), Handb. Clay Sci., Elsevier, Amsterdam, The Nederlands, 2013: pp. 667–710.

[2] F. Huertas, J.L. Fuentes-Santillana, F. Jullien, P. Rivas, J. Linares, P. Fariña, et al., FEBEX project final report. EUR 19147., Madrid (Spain), 2000.

[3] I. Grenthe, J. Fuger, R.J.M. Konings, R.J. Lemire, A.B. Muller, C. Nguyen-Trung Cregu, et al., Chemical thermodynamics of uranium, OECD, Issy-les-Moulineaux (France), 2004.

[4] T. Missana, U. Alonso, M. Garcia-Gutierrez, N. Albarran, T. Lopez, Experimental study and modeling of Uranium(VI) sorption onto a Spanish smectite, in: MRS Symp. Proceeding Vol1124, 2009: pp. 1124–Q07–05.

F2

Unraveling the structure and the excited state dynamics of the aqueous cerium(III) ion by combined experimental and theoretical approaches.

Florent Réal,[1] Valérie Vallet[1], Rafał Janicki[2] , Patric Lindqvist-Reis[3]

[1] *Univ. Lille, CNRS, UMR 8523 - PhLAM - Physique des Lasers Atomes et Molécules, F-59000 Lille, France, e-mail: florent.real@univ-lille1.fr*
[2] University of Wrocław, Faculty of Chemistry, F. Joliot-Curie 14, 50-383 Wrocław
[3]Institut für Nukleare Entsorgung, Karlsruhe Institute of Technology, P.O. Box 3640, 76021 Karlsruhe, Germany

Experimental techniques such as large-angle X-ray diffraction scattering X-ray absorption fine structure spectroscopy (EXAFS) have been successfully used to obtain data about coordination numbers and metal-oxygen bond distances of trivalent lanthanide and some of the trivalent actinide ions in aqueous solution. However, these techniques give a rather vague picture about the local symmetry of the ions and about information about the strength of the metal-ligand interactions in solution, which can be complemented by the UV-vis and luminescence spectroscopies, as the position and intensities of the spectral peaks reflect these properties.

Among the heavy ions, the trivalent cerium ion, considered as an homologue of trivalent actinide ions, has favorable spectroscopic properties (high sensitivity and quantum yield). In dilute aqueous solutions, the five *f-d* transitions of the $Ce^{3+}(aq)$ absorption spectrum[1] were well-attributed (200-260 nm) leading to the conclusion that the mean hydration number is nine in standard conditions; however the presence of a weak sixth band (295 nm) has been attributed to the admixture of transitions from the aqueous $[Ce(H_2O)_8]^{3+}$ ion species,[1–2] present in minor quantities. More striking feature concerns the origin of the large red-shift in the luminescence spectrum in solution (357 nm) but not observed in crystal(312-330 nm); The hypothesis is that a water molecule is photo-dissociated in solution upon excitation so that emission takes place exclusively from an octahydrated species..

In the present work, we tried to find out a correlation between structural and spectroscopic properties of different cerium(III) hydrates, such as $[Ce(H_2O)_n]^{3+}$ (n=8,9), $[Ce(H_2O)_7Cl_m]^{3-m+}$ (m=1,2) and $[Ce(H_2O)_6Cl_2]^{+}$. The experimental results were supported by highly accurate quantum chemical electronic structure calculations on representative cerium-hydrated cluster models, extending thus the work of Kotzian and Rösch.[3] This complementary approach enabled us to explore the potential energy landscape of the photo-dissociation reaction of a water molecule within the $[Ce(H_2O)_9]^{3+}$* cation in the excited electronic states.

References

[1] Okada, K *et al*, H. *J. Chem. Phys.* **1981**, *75*, 1577. Okada, K. *et al*, *Mol. Phys.* **1985**, *54*, 1293–1306.
[2] Kaizu, Y *et al*. *J. Am. Chem. Soc.* **1985**, *107*, 2622–2626.
[3] Kotzian, M.; Rösch, N. *J. Phys. Chem.* **1991**, *96*, 7288–7293.

F3

Sorption of trivalent actinides onto montmorillonite: Macroscopic, thermodynamic and structural evidence for ternary hydroxo and carbonato surface complexes on multiple sorption sites

Maria Marques Fernandes[1], Andreas C. Scheinost[2], Bart Baeyens[1]

[1] *Paul Scherrer Institut, Laboratory for Waste Management*, 5232 Villigen PSI, Switzerland,
e-mail: maria.marques@psi.ch
[2]*Inst. of Resource Ecology, HZDR, 01314 Dresden, Germany*

The credibility of long-term safety assessments of radioactive waste repositories may be greatly enhanced by a molecular level understanding of the sorption processes onto individual minerals present in the near- and far-fields. We couple here macroscopic sorption experiments to surface complexation modelling and spectroscopic investigations, including extended X-ray absorption fine structure (EXAFS) and time-resolved laser fluorescence spectroscopies (TRLFS), to elucidate the uptake mechanism of trivalent actinides, using ^{243}Am, ^{248}Cm or their lanthanide substitute Eu (Ln/An^{III}), by montmorillonite in the absence and presence of dissolved carbonate.

For the carbonate-free system, the previously developed 2 Site Protolysis Non Electrostatic Surface Complexation and Cation Exchange (2SPNE SC/CE) sorption model [1] needed to be complemented with an additional surface complexation reaction onto a weak amphotheric hydroxyl sites of montmorillonite to fit the concentration depended Eu sorption data. In the presence of carbonate, the previously published sorption model [2] required a reduction of the strong-site capacity and the addition of Ln/An^{III}-carbonato surface complexes both on strong and weak sites.

EXAFS spectra of selected ^{243}Am samples corroborate these model assumptions by showing the existence of different amphotheric surface sites and the formation of Ln/An^{III} carbonato surface complexes. In the absence of carbonate and at low surface loadings, Ln/An^{III} form strong inner-sphere complexes through binding to three $Al(O,OH)_6$ octahedra, most likely by occupying vacant sites in the octahedral layers of montmorillonite, which are exposed on {010} and {110} edge faces. At higher loadings, Ln/An^{III} binds to only one Al octahedron, forming a weaker, edge-sharing surface complex. In the presence of carbonate, we identified a ternary mono- or di-carbonato Ln/An^{III} complex binding directly to one $Al(O,OH)_6$ octahedron. This is in line with formation of a type-A ternary complex, where the one or two carbonate groups point away from the surface into the solution phase. These complexes form on weak sites only, within the observable concentration range, in line with the small strong-site capacity suggested by the sorption model. The formation of Ln/An^{III} surface species involving carbonate complexes is also supported by TRLFS. The differences in the fluorescence spectra obtained for samples in the presence and absence of carbonate i.e. red-shift of excitation and emission spectra, as well as the increase of fluorescence lifetimes, unambiguously showed the influence of carbonate. When the solubility of carbonates was exceeded, the formation of an Am carbonate hydroxide solid phase could be identified.

The good agreement between the thermodynamic model parameters developed by fitting the macroscopic data, and the spectroscopically identified mechanisms, demonstrates the mature state of the 2SPNE SC/CE model for predicting and quantifying the retention of Ln/An^{III} elements by montmorillonite-rich clay rocks.

[1] M.H. Bradbury, and B. Baeyens, *Radiochim. Acta* **94**, 619 (2006).
[2] M. Marques Fernandes, B. Baeyens, and M.H. Bradbury , *Radiochim. Acta* **96**, 691 (2007).

F4

Structural characterization of Pa(IV) in aqueous solution and quantum chemical investigations of the tetravalent actinides up to Bk(IV): the evidence of a curium break

Valérie Vallet, Florent Réal,[1] Nidhu lal Banik,[2] Réda Mohamed Belmecheri,[3] Bernd Schimmelpfennig,[2] Jörg Rothe,[2] Rémi Marsac,[3] Patric Lindqvist-Reis,[3] Clemens Walther,[4] Melissa A. Denecke[5] and Christian M. Marquardt[3]

1

[2]Laboratoire PhLAM, UMR-CNRS 8523, Université Lille 1 (Sciences et Technologies), F-59655 Villeneuve d'Ascq, France

[2] Institut für Nukleare Entsorgung, Karlsruhe Institute of Technology, P.O. Box 3640, 76021 Karlsruhe, Germany. E-mail: nidhu.banik@kit.edu

[3] Laboratoire de Thermodynamique et Modélisation Moléculaire, Faculté de Chimie, USTHB BP 32 El-Alia, 16111 Bab-Ezzouar, Algeria

[4]Institut für Radioökologie und Strahlenschutz, Leibniz Universität Hannover, Hannover, Germany

[5]Dalton Nuclear Institute, The University of Manchester, Manchester, UK2

Whereas for the tetravalent actinide Th, U, Np, and Pu, an essential basic understanding of their chemistry in aquatic solution was achieved recently, this is not the case for the tetravalent protactinium. Pa(IV) with the simple electronic configuration, $5f^1$, in its ground state enables speciation by optical spectroscopy, and is also of interest for quantum chemical studies to probe the nature of the actinide-water chemical bonds across the actinide series. However, due to constricted availability of Pa, the cascade of its α-emitting daughters, and the low redox potential only few studies have been performed in this field [1].

Our work aims at filling the gap in the understanding of aquatic chemistry of tetravalent actinides by unravelling the properties of Pa(IV) in various media combining not only complementary experimental methods, such as XAFS, TRLFS and UV-Vis spectroscopies, but also state-of-the art quantum chemical methods to systematically explore the characteristic chemical behavior of Pa(IV) and the neighboring tetravalent ions.

The combined results of EXAFS data and quantum chemically optimized structures suggest that the Pa^{4+} aqua ion has an average of nine water molecules in its first hydration sphere at a mean Pa–O distance of 2.43 Å. The data available for the early tetravalent actinide (An) elements from Th4+ to Bk^{4+} show that the An–O bonds have a pronounced electrostatic character, with bond distances following the same monotonic decreasing trend as the An^{4+} ionic radii, with a decrease of the hydration number from nine to eight for the heaviest ions Cm^{4+} and Bk^{4+}, pointing toward a "Curium break". Being the first open-shell tetravalent actinide, Pa^{4+} features a coordination chemistry very similar to its successors. The electronic configuration of all open-shell systems corresponds to occupation of the valence 5f orbitals, without contribution from the 6d orbitals. Our results thus demonstrate that Pa(IV) resembles its early actinide neighbors [2].

References

[1] R. Wilson, *Nat. Chemistry* **4**, 586 (2012).

[2] N. L. Banik, V. Vallet, F. Réal, R. M. Belmécheri, B. Schimmelpfennig, J. Rothe, R. Marsac, P. Lindqvist-Reis, C. Walther, M. A. Denecke and C. M. Marquardt, *Dalton Trans.* **45**, 453–457 (2016).

F5

The U-Nb-Al phase-diagram: a themodynamic investigation and some characterizations of the intermediate phases

C. Moussa, A. Berche, M. Pasturel, J. Barbosa, B. Stepnik and **O. Tougait**
Université de Lille1

The U-Nb-Al phase-diagram was investigated by combining experimental determination of the isothermal sections at 900 K and 1200 K with their thermodynamic assessment by the Calphad method, allowing to evaluate the thermodynamic parameters. At both temperatures, Nb_2Al shows a substantial ternary extension. The substitution mechanism was confirmed by single crystal diffraction experiments. Only two ternary phases, UNb_2Al_{20} and $U_6Nb_4Al_{43}$ were found, they both form by peritectic reaction, at 1200(5) K and at 1262(5) K, respectively. It was confirmed that UNb_2Al_{20} adopts the $CeCr_2Al_{20}$ type and that $U_6Nb_4Al_{43}$ crystallizes with the $Ho_6Mo_4Al_{43}$ type. Their electronic properties were measured in the temperature range 2-300K, revealing for UNb_2Al_{20} an enhanced Pauli paramagnetism and complex magnetic features for $U_6Nb_4Al_{43}$ at low temperature. For the latter compound a composite behavior involving long and short ranges ordering and magnetic frustration is suspected below 12 K.

Email of presenting author: tougait@univ-rennes1.fr

Long abstract: was not submitted

G1

Density Functional Theory Studies of Actinide Oxides

Ping Zhang

Institute of Applied Physics and Computational Mathematics, 100088 Beijing, China, e-mail: zhang_ping@iapcm.ac.cn

Plutonium is very easy to react with oxygen in the environment to form surface oxides, such as PuO_2 and Pu_2O_3, due to its strong chemical activities. It is a crucial research goal in the plutonium community to fully understand the characteristics of these surface plutonium oxides by studying the competitive diversity in 5*f* orbitals, such as delocalization/localization, spin-orbit coupling, directionality and anisotropy in chemical bonding, as well as the corresponding energy spectrum. We have carried out systemic first-principles calculations to study the plutonium oxides and achieved a series of basic research progress, which can be summarized as follows. (1) The electronic structure, mechanical, and thermodynamic properties of the plutonium oxides have been studied by DFT+*U* theory. By comparing with the ground-state electronic structures of ThO_2, UO_2, and NpO_2, it is found that the covalent Pu-O, U-O, and Np-O bonds are all stronger than that of Th-O one, i.e., the ionicity in the Th-O bond is strongest in these difference actinide oxides. (2) The dielectric function and optical properties of PuO_2 and α-Pu_2O_3 have been calculated and compared with each other by using the linear-response theory in the framework of DFT+*U*. The results provide a useful optical criterion to distinguish different plutonium oxides. (3) We have obtained the DFT+*U* phonon dispersion of PuO_2, which was subsequently confirmed by inelastic X-ray scattering measurement from Lawrence Livermore National Laboratory and the Argonne National Laboratory. (4) We have studied the thermodynamic equilibrium and oxidation–reduction transformation between PuO_2 and α-Pu_2O_3. The obtained spontaneous reduction conditions of $PuO_2 \rightarrow \alpha$-Pu_2O_3 are in good agreement with the experiments. (5) The point defects and helium diffusion behavior in PuO_2 have been investigated from first principles. It is revealed that the most stable dissolved sites in PuO_2 are linked to the concentration of oxygen vacancies. Helium atoms tend to occupy the octahedral interstitial sites and oxygen vacancies in intrinsic and oxygen-vacancy pre-existing PuO_2 systems, respectively. These impurity atoms are difficult to diffuse in the intrinsic PuO_2 due to the large migration barriers. One useful manner for helium diffusion is with the help of the oxygen vacancies. (6) Our first-principles molecular dynamic simulations based on DFT+*U*+vdW approach show that it is difficult for H_2 to get close to the PuO_2 surface directly. However, H_2 can penetrate into the α-Pu_2O_3 layer and then reach the plutonium layer while still keeping its molecular state. This theoretical result supports the experimental observation that α-Pu_2O_3 can accelerate the hydrogenation of plutonium with respect to PuO_2. (7) Finally, $PuO_2(111)$ has been found to be the most stable surface, while for $PuO_2(001)$, there is a prominent surface reconstruction phenomenon. These facts are similar to what happened on the UO_2 surfaces that have been previously reported in experiments.

References

[1] B. Sun, P. Zhang, and X.-G. Zhao, *J. Chem. Phys.*, **128**, 084705 (2008).
[2] P. Zhang, B.-T. Wang, and X.-G. Zhao, *Phys. Rev B*, **82**, 144110 (2010).
[3] B.-T. Wang, H. Shi, W. Li, and P. Zhang, *Phys. Rev B*, **81**, 045119 (2010).
[4] H. Shi, M. Chu, and P. Zhang, *J. Nucl. Mater*, **400**, 151 (2010).
[5] H. Shi and P. Zhang, *J. Nucl. Mater*, **420**, 159 (2012).
[6] B. Sun, H. Liu, H. Song, G. Zhang, H. Zheng, X.-G. Zhao, and P. Zhang, *J. Nucl. Mater*, **426**, 139 (2012).
[7] B. Sun, H. Liu, H. Song, G. Zhang, H. Zheng, X.-G. Zhao, and P. Zhang, *Phys. Lett. A*, **376**, 2672 (2012).
[8] B.-T. Wang, P. Zhang, R. Lizárraga, I. D. Marco, O. Eriksson, *Phys. Rev B*, **88**, 104107 (2013).
[9] Y. Lu, Y. Yang, and P. Zhang, *J. Alloys and Compounds* **649**, 544 (2015).
[10] Y. Yang, Y. Lu, and P. Zhang, *J. Nucl. Mater*. **452**, 414 (2014).

G2

Crystal dynamics of neptunium dioxide

L. Paolasini[1], P. Maldonado[2], P. M. Oppeneer[2], T. R. Forrest[1], A. Prodi[3], N. Magnani[4], A. Bosak[1], G. H. Lander[4], R. Caciuffo[4]

[1] *European Synchrotron Radiation Facility (ESRF), B.P.220, F-38043 Grenoble, France*
e-mail: paolasini@esrf.eu
[2] *Department of Physics and Astronomy, Uppsala University, Box 516, S-75120 Uppsala, Sweden*
[3] *Consiglio Nazionale delle Ricerche, ISM, via Salaria km 29.300, Montelibretti, Italy*
[4] *European Commission, JRC-ITU, Postfach 2340, D-76125 Karlsruhe, Germany,*

The energy-wavevector dispersion relation for normal modes of vibration propagating along high-symmetry lines in NpO_2 at room temperature has been determined by measuring the coherent one-phonon scattering of X-rays from a ~1.2 mg single-crystal specimen. The results are compared against ab initio phonon dispersion simulations computed within the first-principle density functional theory in the generalized gradient approximation plus Hubbard U correlation (GGA+U) approach, taking into account third-order anharmonicity effects in the quasi-harmonic approximation. Good agreement with the experiment is obtained for calculations with an on-site Coulomb parameter U = 4 eV and Hund's exchange J = 0.6 eV in line with previous electronic structure calculations. Thermal expansion, heat capacity, thermal conductivity, phonon linewidth, and thermal phonon softening are calculated and compared with available experimental data.

The inelastic X-ray scattering (IXS) experiment was carried out on a high-quality single crystal of NpO_2 using the ID28 beamline at ESRF with an incident energy E=17.794 keV, provided by a flat Si (999) perfect crystal back-scattering monochromators followed by a horizontally focusing multilayer. As severe sample photo-absorption is present, data have been collected in reflection geometry. A beam spot size of 30x80 μm^2 on the sample surface was obtained by using a multilayer focusing configuration. The sample of dimension of 0.4×0.3×0.3 mm^3 was oriented with the specular direction along the (100) crystal axis and the (011) axis in the scattering plane. To avoid contamination of the environment, the crystal was encapsulated between two single crystal diamond slabs of 0.5×5×5 mm^3 at the JRC Institute of Transuranium Elements in Karlsruhe. Examples of typical IXS constant-Q energy scans collected at room temperature are shown in Fig. 1. We have investigated different Brillouin zones in order to optimize the inelastic structure factor for the different optic branches. Optic phonons arise mainly from oxigen vibration modes and are very weak.

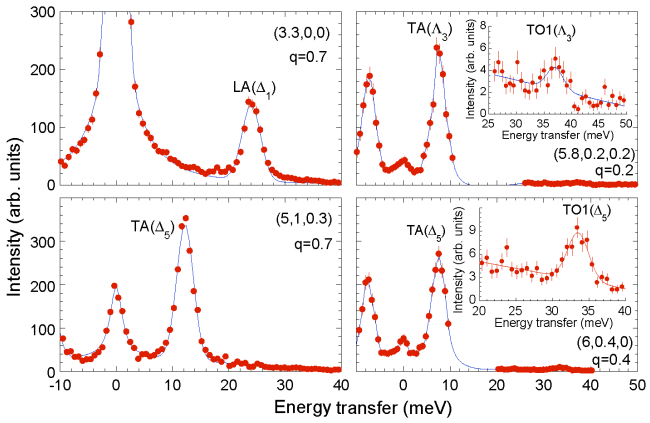

Figure 1. Examples of constant-Q inelastic X-ray scattering energy scans collected at room temperature for NpO_2 around different Brillouin zone centres. The intensity data are in arbitrary units but have been scaled for the same factor. To be noticed is the difference in intensity between acoustic and optic phonon modes.

The good agreement of the experimental results with the ab initio calculated phonon dispersions indicates that the GGA+U approximation provides a good description of the phononic system, and allows for the study of its thermodynamic properties. The calculated heat capacity, bulk modulus, and thermal conductivity are in good agreement with the measured quantities. The failure in the description of the thermal expansion at high temperatures stresses the limitation of the quasi-

harmonic approximation to study actinide oxides beyond ~ 1000 K. We show that optical phonons contribute significantly to the heat transport due mainly to their large velocities and short lifetimes. Compared with UO_2, the main differences in the phonon density of states are a softening of the optical modes and an increase of the peak centered around 55 meV, whereas the acoustic modes in NpO_2 are shifted to higher frequencies. The calculated value at 0 K of the bulk modulus in NpO_2 is in agreement with the experimental value and slightly smaller than the one determined by high-pressure X-ray diffraction for UO_2. NpO_2 has a smaller thermal conductivity than UO_2, at least in the temperature range 600 to 1000 K for which experimental values are available This is accounted for by our simulation, which overestimates the experimental value for NpO_2 by ~20% at 600 K and underestimate it by ~1% at 1000 K [1].

The second part of the experiment was performed at low temperature (10 K) searching for phonon anomalies in the acoustic region below 15 meV. Indeed, according to previous work [2] in NpO_2 the magnetic dipole s are quenched in the ordered phase, and the primary order parameter is the rank-5 (triakontadipole) magnetic multipole. This exotic magnetic order is accompanied by an order of electric quadrupoles that are arranged in a type-I, 3-k longitudinal structure. The ground-state quartet of the Np ions is split in the ordered phase, with a singlet-doublet-singlet sequence. The singlet-doublet and singlet-singlet single-ion transitions give rise to dispersive multipolar excitation branches centred around 6 and 13 meV. Similarly to what observed by inelastic neutron scattering in UO_2 [3], it is expected that a strong interaction between magnetic and vibrational modes occurs through the mediation of electric quadrupole fluctuations. This will affect the phonon acoustic modes centered around 13 meV and at 6 meV.

We have measured the LA (6-ζ, 0, 0), TA (6, ζ, 0) and TA (5, -1, ζ) phonon branches at 10 K. Whereas the LA phonon intensities decreases smoothly from the zone centre to the zone boundary, as expected from the first-principle phonon calculations (that provide an excellent match to the measured dispersion curves), the two measured TA branches present an anomaly at the reduced wavevector ζ = 0.8, reflected in a drastic loss of intensity of the corresponding phonon group, as shown in Fig. 2 for the TA (6, q, 0) branch. This wavevector corresponds to about 13 meV, exactly where the theoretical prediction assumes the existence of dispersive mean-field magnetic modes. This issue will be the subject of further investigations on ID28 in order to check whether the intensity anomaly is an experimental artefact or if it really related to the order of the magnetic triakontadipoles.

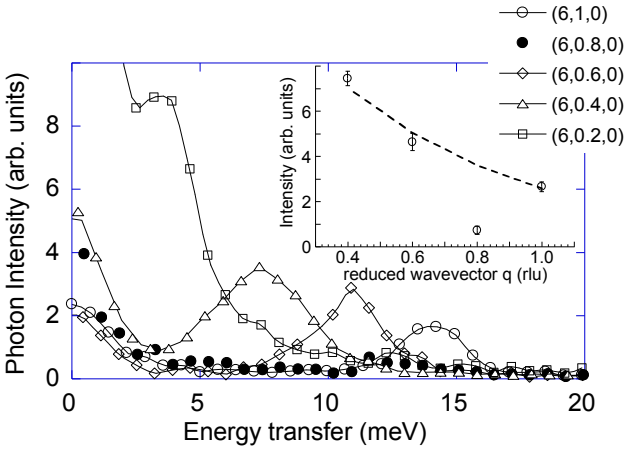

Figure 2. Intensity evolution of the transverse acoustic (6, ζ, 0) branch showing a drastic decrease of the intensity of the phonon group at ζ = 0.8 rlu (black dots). Notice also that the (610) is a Brillouin zone boundary. The inset shows the q dependence of the phonon group integrated intensity.

References

[1] P. Maldonado *et al.*, to be published
[2] P. Santini *et al., Phys. Rev. Lett.* **97**, 207203 (2006)
[3] R. Caciuffo *et al., Phys. Rev. B.* **84**, 104409 (2011)

G3

Ab-initio calculation of oxygen self-diffusion coefficient in uranium dioxide UO_2

Boris Dorado,[1] Philippe Garcia[2], David A. Andersson[3], Chris R. Stanek[3], Marc Torrent[1]

[1] CEA, DAM, DIF, F-91297 Arpajon, France, e-mail: boris.dorado@cea.fr
[2] CEA, DEN, DEC, F-13108 Saint-Paul-Lez-Durance, France
[3] MST Division, Los Alamos National Laboratory, Los Alamos, NM 87545, USA

Uranium dioxide is the most widely used nuclear fuel worldwide and its atomic transport properties are relevant to practically all engineering aspects of the material. Although transport properties have already been studied in UO_2 by means of first-principles calculations [1-5], the *ab-initio* determination of self-diffusion coefficients has up to now remained unreachable because the relevant computational tool were neither available or adapted.

The present work reports our results related to the *ab-initio* calculation of the oxygen self-diffusion coefficient in UO_2. We first determine the Gibbs free energies of formation of oxygen charged defects by calculating both the electronic and vibrational (hence entropic) contributions. Then, we use the transition state theory in order to compute the effective jump frequency of the defects, which in turn provides us with the value of the pre-exponential factor. The results are compared to self-diffusion data obtained experimentally [2,6].

References

[1] B. Dorado *et al.*, *Phys. Rev. B* **79**, 235125 (2009)
[2] B. Dorado *et al.*, *Phys. Rev. B* **83**, 035126 (2011)
[3] D. A. Andersson *et al.*, *Phys. Rev. B* **84**, 054105 (2011)
[4] B. Dorado *et al.*, *Phys. Rev. B* **86**, 035110 (2012)
[5] D. A. Andersson *et al.*, *J. Nucl. Mater.* **451**, 225 (2014)
[6] P. Garcia *et al.*, *J. Nucl. Mater.* **400**, 112 (2010)

G4

Measurements of acoustic phonons in irradiated UO_2 epitaxial films

S. Rennie, J. E. Darnbrough, R. Springell, L. Paolasini, A. Bosak, & G. H. Lander
UoB, ITU, ESRF

A key limitation of using uranium dioxide as a nuclear reactor fuel is the significant reduction in thermal conductivity (κ) that occurs as a function of irradiation damage. This reduction is not understood at a microscopic level. Since κ is related to the frequency and line-width of the phonons, which are the main mechanism for heat transfer in UO2, we have started a programme of measurements of the phonons from thin (~ 500 nm) epitaxial films irradiated with 2.1 MeV He2+ ions. The acoustic phonons in the [110] direction were observed using grazing incidence inelastic x-ray scattering. First results suggest that the longitudinal modes are not affected by the irradiation, but the transverse modes are reduced slightly in frequency and broadened significantly. New measurements this year should significantly improve the signal/noise ratio, these results will be instrumental in corroborating first-principle calculations of phonon properties in damaged UO_2.

Email of presenting author: sophie.rennie@bristol.ac.uk

Long abstract: was not submitted

G5

Thermodynamic stability of the UO2 surfaces: Interplay between over-stoichiometry and polarity compensation

François Bottin,[1] Grégory Geneste[1], Gérald Jomard[2]

[1] *CEA, DAM, DIF, F-91297 Arpajon, France, e-mail: francois.bottin@cea.fr*
[2] *CEA, DEN, DEC, F-13108 Saint-Paul-lez-Durance, France*

The thermodynamic stability of UO_2 surfaces is investigated using *ab initio* calculations in the GGA+*U* framework [1].

Among the seven (100), (110) and (111) terminations studied, we predict that the stoichiometric O-(111) is the most stable one under oxygen-poor or -intermediary environments. At odds with other fluorite surfaces [2], the overstoichiometric and polar O_2-(100) and O_2-(111) terminations become the most stable in oxygen-rich environments with strong modifications of the electronic structure within the upper layers. Some U-*5f* surface states are emptied, leading to higher U^{5+} and U^{6+} oxidation states, but leaving the surface insulating.

This unexpected polarity compensation mechanism [3] is not observed for other charge transfer compounds (such as PuO_2 [4]) and can be related to the *f-f* Mott-Hubbard band gap of the UO_2 material. By considering the most stable stoichiometric and overstoichiometric terminations the Wulff shape of nano-voids in UO_2 crystals can be explained.

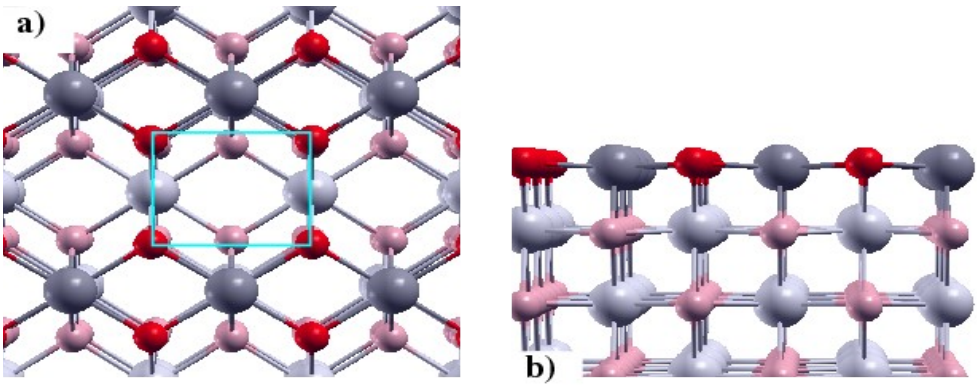

Fig. 1. Left (right) panel: Top (side) view of the UO_2-(110) non-polar and stoichiometric termination.

References

[1] F. Bottin, G. Geneste and G. Jomard, submitted to *Phys. Rev. B.*
[2] Z. Rak, R. Ewing, and U. Becker, *Surf. Sci.* **608**, 180 (2013) .
[3] C. Noguera, J. Phys.:Condens. Matter **12**, R367 (2000); J. Goniakowski, F. Finocchi, and C. Noguera, Rep. Prog. Phys. **71**, 016501 (2008).
[4] G. Jomard, B. Amadon, F. Bottin, and M. Torrent, Phys. Rev. B **78**, 075125 (2008); G. Jomard and F. Bottin, Phys. Rev. B **84**, 195469 (2011).

G6

Trends in rare gases incorporation into uranium dioxide

Haiyan Lu,[1] Bingyun Ao[1]

[1] *Institute of Materials, China Academy of Engineering Physics, P.O. Box 919-71, Postal-code: 621907, Mianyang, China e-mail: hyluphys@163.com*

Abstract: First-principles density functional theory–generalized gradient approximation methods have been used to calculate the energetics (incorporation energy, formation energy and binding energy) of rare gases (He, Ne, Ar, Kr and Xe) at the three point defects (octahedral interstitial, uranium and oxygen vacancies) of uranium dioxide. The Hubbard parameter *U* and van der Waals corrections have been used to describe the strongly correlated electronic behavior of uranium 5*f* electrons and the weak interactions of rare gases, respectively. The results indicate that the energetics of rare gases depend significantly on the incorporation sites and on the atomic properties such as atomic radius. All rare gases considered here are energetically unfavorable at the three incorporation sites. However, rare gases exhibit significant binding ability to both U and O vacancies. The main trends of relative stability of rare gases generally reflect a size effect: the rare gases become more unstable with increasing atomic number. Electronic structures of these systems containing rare gases also exhibit general trends in their relative stability and charge-transfer character.

Key Words: Uranium dioxide; Crystal defect; Rare gases; Density functional theory; Electronic structure

H1

First-principles DFT+*U* investigation of actinide oxides including point defects and fission gases

Lei SHI,[1] Emerson Vathonne,[1] Yaguang Li,[1] Ibrahim Cheik Njifon,[1] Michel Freyss,[1] Marjorie Bertolus,[1] Roland Hayn[2] and Vincent Oison[2]

[1] *CEA, DEN, Centre de Cadarache, Saint-Paul-Lez-Durance, 13108 France, e-mail:lei.shi@cea.fr*
[2]*Aix-Marseille University, IM2NP, 13397 Marseille Cedex 20, France*

We investigate radiation damage in nuclear fuels UO_2 and (U, Pu)O_2 at the atomic scale using electronic structure calculations based on the density functional theory (DFT). A Hubbard-like Coulomb interaction term (DFT+U method) is added to have a proper description of f electron exchange correlation interactions of the cations. To get further insight into the point defect stability and fission gas trapping property, we calculate the defect formation energies and fission gas incorporation energies.

CeO_2 and (U, Ce)O_2 are proposed as low-radioactivity surrogates of UO_2 and mixed actinide oxides, respectively, for the experimental radiation damage study of nuclear fuels. To ensure that the assumption is correct, we also study the similarities between these compounds in terms of bulk properties, point defect and fission gas behaviour. Overall good agreement has been found in our study considering the point defect formation energies (see Fig.1) and fission gas (Xe and Kr) incorporation energies between CeO_2 and UO_2[1-4], which supports the assumption that CeO_2 is capable of simulating UO_2 for experimental radiation damage study. However, further confirmation is required by considering atomic transport properties of defects, grain boundary behaviour and fission gas release in CeO_2 and UO_2 using relevant modelling techniques.

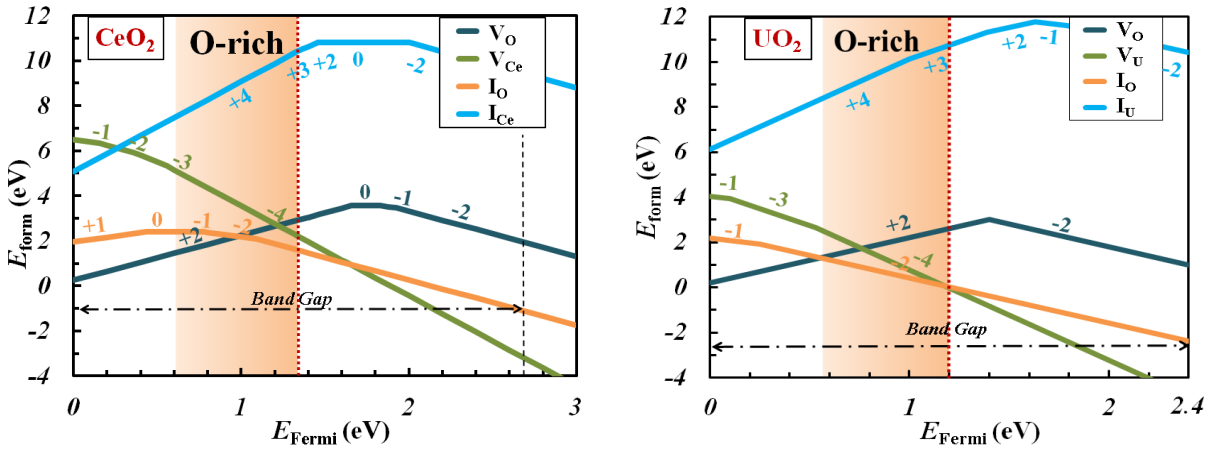

Fig. 1. Formation energies of point defects (O interstitial, O vacancy, cation interstitial and cation vacancy) as a function of Fermi level for CeO_2 and UO_2 under O-rich conditions.

References

[1] E. Vathonne, J. Wiktor, M. Freyss, G. Jomard, and M. Bertolus, J. Phys.: Condens. Mat. 26, 325501 (2014).
[2] E. Vathonne, Ph.D. thesis, Aix Marseille University (2014)
[3] B. Dorado, Ph.D. thesis, Aix Marseille University (2010).
[4] D. A. Andersson, B. P. Uberuaga, P. V. Nerikar, C. Unal, and C. R. Stanek, Phys. Rev. B 84, 054105 (2011).

XRD and XAS investigations of (U,Am)O2 compounds with high Am-content

E. Epifano, R. Belin, R. Vauchy, D. Prieur, F. Lebreton, T. Delahaye, C. Guéneau, Ch. Valot, P. M. Martin
CEA/DEN/SECA/LCC

In the frame of americium transmutation, $(U,Am)O_{2-x}$ are promising fuels. In order to foresee their in-pile behavior, a complete knowledge of their physical/chemical properties is needed.
Here the recent results obtained on $(U,Am)O_{2-x}$ compounds using XRD and XAS are shown. These techniques give access to both long and short range order and cation valence states.
The initial studies, relating to samples with Am-content up to 50 mol.%, showed that the UO_2 fluorine structure is maintained. Nevertheless, a peculiar charge distribution was observed, with Am fully reduced to trivalent state and U partially oxidized, suggesting a charge compensation mechanism [1-4]. However, for stoichiometric compounds with higher Am content the U^{+5}/Am^{+3} charges compensation is no more sufficient and the Am is partially oxidized to the +4 state. The recent investigations performed on samples with Am contents up to 70 mol.% are presented and the effect of the Am on the structural disorder is discussed.

[1] D. Prieur *et al.*, Inorg. Chem., 50 (2011) 12437-12445.
[2] D. Prieur *et al.*, J. Nucl. Mater. 434 (2012) 7-16.
[3] F. Lebreton *et al.*, Inorg. Chem., 53 (2014) 9531-9540
[4] F. Lebreton *et al.*, Inorg. Chem., 54 (2015) 9749-9760

Email of presenting author: enrica.epifano@cea.fr

Long abstract: was not submitted

H3

On the influence of Np incorporation on the redox of UO_2

Mélanie Chollet, Philippe Martin, Renaud Belin, Claude Degueldre, Cristoph Henning
PSI

Due to its long half-life time, attention is brought on Np in the scope of a reasonable nuclear waste management. The ^{237}Np could be produced during in-pile operation by neutron capture by ^{235}U. One of the solutions could be the transmutation in the future fast neutron reactors. Np will be incorporated into the UO_2 fuel or blanket at various contents. The stoichiometry of the $U_{1-y}Np_yO_{2\pm x}$ compound has to be assessed since it affects the thermal, chemical and physical properties of the fuel.
We report Np and U oxidation states in $U_yNp_{1-y}O_2$ and oxidized $U_yNp_{1-y}O_{2+x}$ compounds. XAS spectra obtained at the ROBL beamline (ESRF) prove that Np remains at the +IV oxidation state contrary to U that admits increasing oxidation states +IV, +V and +VI with increasing O stoichiometry.
The experimental observations are completed by thermodynamic calculations including the ideal Gibbs energy of mixing that achieve the same results.
This study confirms the buffering capacity of Uranium.

Email of presenting author: melanie.chollet@psi.ch

Long abstract: was not submitted

Poster abstracts

P1 **Thermal Evolution of Vibrational Properties of α-U**
Johann Bouchet and Francois Bottin
CEA

P2 **Electronic structure of superconducting $ThIr_2Si_2$ and reference systems**
M. Samsel-Czekała, K. Domieracki, A.P. Pikul, D. Kaczorowski
Polish Academy of Sciences

P3 **Atomistic-level model of electronic and magnetic properties of rare-earth adatoms on graphene**
Agnieszka L. Kozub, Jindrich Kolorenc, and Alexander B. Shick
FZU ASCR, GUT

P4 **Instability of itinerant magnetic moments in pure R and in RCo_2 compounds (R=Gd,Tb)**
K. Carva, P.M. Oppeneer, S. Wienholdt, D. Hinzke, and U. Nowak
Charles University in Prague

P5 **Crystal structure and physical properties of $ThPt_{3+x}Be$**
Roman Gumeniuk, Walter Schnelle, Andreas Leithe-Jasper
TU BAF

P6 **Crystallographic, magnetic, electrical and specific heat properties of novel phases in the U-Pt-Si system**
N. Brisset, G. Chajewski, A. Berche, A. Novikova, **M. Pasturel**, A. P. Pikul, O. Tougait, H. Noël
ISCR

P8 **Superconductivity in $ThIr_2Si_2$**
Krzysztof Domieracki and **Dariusz Kaczorowski**
Polish Academy of Sciences

P9 **Magnetic anisotropy of UO_2 via exchange bias studies of UO_2/Fe_3O_4 thin films**
E. A. Tereshina, Z. Bao, L. Havela, S. Danis, T. Gouder, R. Caciuffo
Institute of Physics CAS, ITU

P10 **Magnetism and hydrogen absorption in UNi(Zn,Al) system**
Silvie Maskova, Stanislav Danis, Khrystyna Miliyanchuk, Olha Stelmakhovych, Barbora Vondrackova, Ladislav Havela
Charles University in Prague

P11 **Pressure-Induced Structural Behavior of CeNi**
Vladimir Matvienko, Alexey Mirmelstein, Andrey Podlesnyak, Georg Ehlers, G. Halder
RFNC-VNIITF

P12 **Unusual temperature dependence of Mössbauer isomer shift in NpF_4**
Itzhak Halevy
Nuclear Research Center

P13 **Recent developments in UCx-based spallation targets at C2TN**
S. Chowdhury, M.S. Henriques, A. Cruz,1 T. Stora
C2TN, Institute of Physics, ASCR, CERN Presenter: **A. P. Goncalves**

P14 **Experimental study of shape memory effect in U6.3 wt.%Nb alloy**
A.V. Troshev, A.M. Golunov, D.A. Chentsov, A.V. Baluev, A.V. Shestakov
Russian Federal Nuclear Center

P15 **Localized corrosion behaviour of uranium based materials**
L. Costelle, R. Springell, P. Martin, R. Burrows, T. Scott
IAC

P16 **A novel layer type for the first compound in the Strontium Uranium oxifluoride system**
Laurent Jouffret, Jean-Michel Hiltbrunner, Marc Dubois
ICCF

P17 **Uranium wet oxidation under contained conditions**
Antonios Banos, Tom Scott
University of Bristol

P18 **Synthesis and Characterisation of Accident Tolerant Fuels**
Eleanor Lawrence Bright, Tom Bligh Scott, David Goddard, Ross Springell
UoB, NNL

P19 **Polygonisation of UO_2 high-burn-up fuel investigated by micro-X-ray diffraction**
Mélanie Chollet, Johannes Bertsch, Daniel Grolimund
PSI

P20 **X-ray Magnetic Circular Dichroism and Mössbauer Effect studies of the heavy fermion superconductor $NpPd_5Al_2$**
A. Hen, F. Wilhelm, A. Rogalev, E. Colineau, R. Eloirdi, J.-C. Griveau, N. Magnani, T. Klimczuk, I. Halevy, J.-P. Sanchez, A. B. Shick, and R. Caciuffo
ESRF, ITU, Ben Gurion University, Nuclear Research Center Negev, CEA/UJF-Grenoble, Academy of Sciences Prague

P21 **Syntheses and basic physical properties of ThT_2M_2 compounds (T = d-electron transition metal and M = Si or Ge)**
Krzysztof Domieracki, Małgorzata Samsel-Czekała, **Adam Pikul**, Dariusz Kaczorowski
Polish Academy of Sciences

P1

Thermal Evolution of Vibrational Properties of α-U

Johann Bouchet,[1] Francois Bottin[1]

[1] *CEA, DAM, DIF, 91297 Arpajon Cedex*, France, *e-mail: johann.bouchet@cea.fr*

By means of ab initio molecular dynamic calculations, the thermal evolution of vibrational properties in α-U is studied at low temperature. The phase transition undergone by this material around 50 K was previously studied extensively using ab-initio calculations in the framework of the linear response at 0 K[1]. Although these previous efforts capture successfully the complexity of the experimental phonon spectrum at room temperature, in particular the soft-phonon mode and its pressure dependence, they fail to reproduce the transition to the charge-density wave state at ambient pressure as a function of temperature. In the present work[2], by going beyond the quasi-harmonic approximation and taking into account the temperature effects explicitly, we are able to reproduce the behaviour of both phonon spectrum and elastic constants of α-U as a function of temperature.

References

[1] J. Bouchet, *Phys. Rev. B* **77**, 024113 (2008)
[2] J. Bouchet and F. Bottin, *Phys. Rev. B* **92**, 174108 (2015)

P2

Electronic structure of superconducting $ThIr_2Si_2$ and reference systems

M. Samsel-Czekała, K. Domieracki, A.P. Pikul, D. Kaczorowski

Institute of Low Temperature and Structure Research, Polish Academy of Sciences, P.O. Box 1410, 50-950 Wrocław 2, Poland, e-mail: M.Samsel@int.pan.wroc.pl

Most representatives of the series of thorium-based silicides ThT_2Si_2 with *d*-electron transition-metal atoms *T* crystallize in a common tetragonal structure of the $ThCr_2Si_2$-type (space group *I*4/*mmm*), while only the compound $ThIr_2Si_2$, adopting a different $CaBe_2Ge_2$-type crystal structure (space group *P*4/*nmm*), exhibits bulk superconductivity below T_c = 2.1 K, being probably of the BCS-type. In this contribution, the electronic structure of the $ThIr_2Si_2$ superconductor, calculated employing fully relativistic and full potential FPLO band-structure code, will be presented and discussed in comparison with the results obtained for a few non-superconducting ThT_2Si_2 phases.

P3

Atomistic-level model of electronic and magnetic properties of rare-earth adatoms on graphene

Agnieszka L. Kozub[1,2], Jindřich Kolorenč[1], and Alexander B. Shick[1]

[1] *Institute of Physics, ASCR, Na Slovance 1999/2, 18-221 Prague, Czech Republic, e-mail: kozub@fzu.cz*
[2] *Gdansk University of Technology, Narutowicza 11/12, 80-233 Gdansk, Poland*

The electronic structure of selected rare-earth impurities on a free standing graphene was investigated making use of DFT+U and DFT+ED methods in order to examine the role of the electron correlations and the spin orbit coupling. The Nd and Sm adatoms were considered in an optimized structural geometry. DFT+U predicts both atoms to carry local magnetic moments (spin and orbital). This is expected for Nd, but not for Sm which has a non-magnetic f^6 (J=0) ground state configuration.

To proceed beyond the DFT+U in the electronic structure of the 4f-adatoms on graphene we use DFT+ exact diagonalization (DFT+ED) methodology, which combines LDA with exact diagonalization of the Anderson impurity model. For the Sm adatom, DFT+ED yields a non-magnetic singlet ground state with the 4*f* shell occupation n_f=6.0. The spin S_f, orbital L_f and total J_f angular moments in the ground state are S_f = 2.9, L_f = 2.9, and J_f = 0. The singlet ground state is separated from the first excited triplet state by the gap of 50 meV. Nd-adatom remains magnetic, with n_f=3.7 *f*-electrons. It has degeneracy of nine and the angular moments are S_f = 1.8, L_f = 6, and J_f = 4.2. The ground state is separated from the first excited sixtet state by the gap of 21 meV.

We suggest experimental verification of our conclusions by STM and XAS/XMCD experimets, and provide theoretical predictions for the STM and XAS spectra of the selected adatoms.

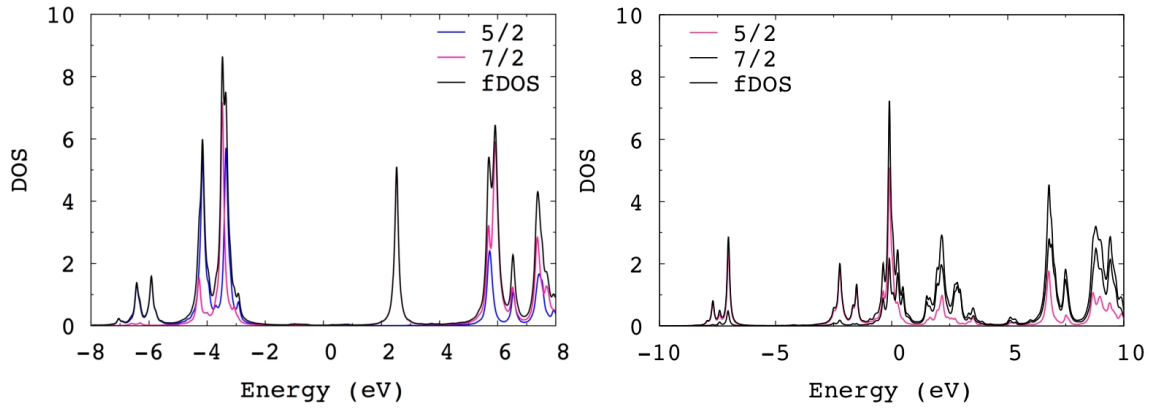

Figure 1: f-electron density of states (fDOS) and j=5/2, 7/2 projected for the Sm adatom on graphene (left), and the Nd adatom on graphene (right).

P4

Instability of itinerant magnetic moments in pure R and in RCo_2 compounds (R=Gd,Tb)

K. Carva, P.M. Oppeneer, S. Wienholdt, D. Hinzke, and U. Nowak
Charles University in Prague, DCMP, Ke Karlovu 5, CZ-12116, Prague, Czech Republic

It is known that the 5*d* moment in Gd or Tb is instable, its magnitude is changing with temperature. However it does not completely vanish when 4*f* moments are completely disordered, hence neither Stoner nor Heisenberg model can be applied here. Recent experiments in ultrafast regime have allowed to decouple this moment from the 4*f* moment on a ps timescale, thus breaking the intraatomic interaction between them. We calculate how does its magnitude depend on the angle between 5*d* and 4*f* moments and find magnetization dynamics in agreement with the experiment. There are also interesting differences between magnetization dynamics of Gd and Tb.
Similarly for RCo_2 compounds, the whole Co moment depends strongly on the order of R moments. Contrary to the continuosly changing partial itinerant part of momentum in R, for Co moment we find several possible discrete values.

Email of presenting author: karel.carva@mff.cuni.cz

Long abstract: was not submitted

P5

Crystal structure and physical properties of $ThPt_{3+x}Be$

Roman Gumeniuk,[1,2] Walter Schnelle[2], Andreas Leithe-Jasper[2]

[1] *Institut für Experimentelle Physik, TU Bergakademie Freiberg, Leipziger Str. 23, 09596 Freiberg, Germany., e-mail: roman.gumeniuk@physik.tu-freiberg.de*
[2] *Max-Planck-Institut für Chemische Physik fester Stoffe, Nöthnitzer Str. 40, 01187 Dresden, Germany.*

$ThPt_{3+x}Be$ was synthesized by arc-melting of the elements with further annealing at 1200 K for one week. It adopts an unique crystal structure with space group *I*4/*mmm* and unit cell parameters *a* = 7.7370(1) Å and *c* = 11.4990(1) Å. $ThPt_{3+x}Be$ shows similar structural motifs as those occurring in crystal structures of cubic Ru_3Sn_7 [1] and $W_2Cr_{21}C_6$ [2] types (Fig. 1). The main characteristic fragment in these structural arrangements is a cube sharing its edges with 4 tetragonal antiprisms. These cubes are partially filled only in $ThPt_{3+x}Be$ type. The fragments are interconnected with each other either by two condensed tetragonal antiprism (Ru_3Sn_7 and $ThPt_{3+x}Be$ types) or by cubooctahedra ($W_2Cr_{21}C_6$ type). Between these main building blocks filled ($RuRu_2Sn_4$) or empty ($@Th_2Pt_4$) octahedra occur in the structures of Ru_3Sn_7 and $ThPt_{3+x}Be$, respectively.

$ThPt_{3+x}Be$ is diamagnetic with $\chi_0 = 3.0 \times 10^{-5}$ emu mol^{-1}. Its electrical resistivity smoothly increases with increasing temperature and low temperature specific heat fits well to $C_p = \gamma T + \beta T^3 + \delta T^3$, with Sommerfeld coefficient $\gamma = 29.5$ mJ mol^{-1} K^{-2}, and phonon contributions $\beta = 2.4$ mJ mol^{-1} K^{-4} and $\delta = 0.05$ mJ mol^{-1} K^{-6}. Sommerfeld coefficient γ corresponds to 13 states eV^{-1} f.u.$^{-1}$ at the Fermi level E_F. All these observations indicate $ThPt_{3+x}Be$ to be a typical metallic system.

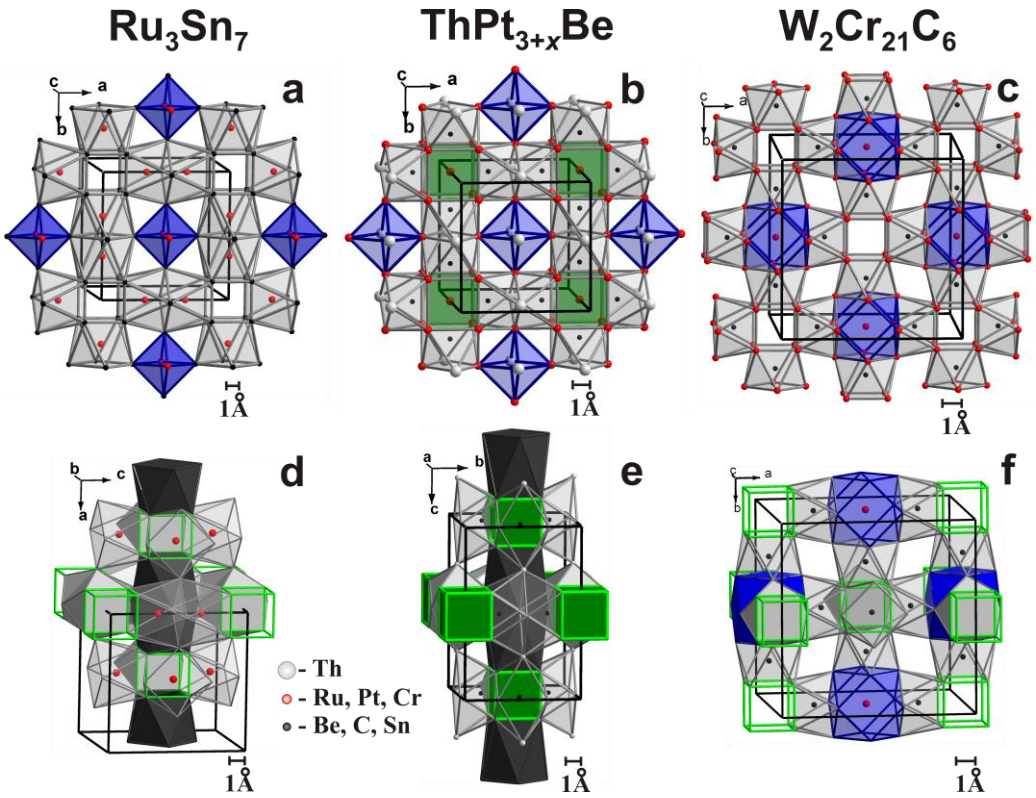

Fig.1. Relationship between crystal structures of Ru_3Sn_7, $ThPt_{3+x}Be$ and $W_2Cr_{21}C_6$ types. Figures a-b show *ab*-projections, while in d-f different projections are shown.

References

[1] H.N. Nowotny, K. Schubert, U.Dettinger, *Metallforsch.* **1**, 137 (1946).
[2] E.I. Gladyshevskii, V.S. Telegus, T.F. Fedorov, Yu.B. Kuz'ma, Russ. Metallurgy 1967, 97 (1967)

P6

Crystallographic, magnetic, electrical and specific heat properties of novel phases in the U-Pt-Si system

N. Brisset[1], G. Chajewski[2], A. Berche[1,3], A. Novikova[1], M. Pasturel[1], A. P. Pikul[2], O. Tougait[1,4], H. Noël[1]

[1] *Institut des Sciences Chimiques de Rennes, Chimie du Solide et Matériaux, UMR CNRS 6226, Université Rennes 1, Campus de Beaulieu bât. 10A, 35042 Rennes Cedex, France*
e-mail: mathieu.pasturel@univ-rennes1.fr
[2] *W. Trzebiatowski Institute of Low Temperature and Structure Research, Polish Academy of Sciences in Wrocław, ul. Okólna 2, 50-422 Wrocław, Poland*
[4]*Unité de Catalyse et de Chimie du Solide, UMR CNRS 8181, Université de Lille1, 59695 Villeneuve d'Ascq, France*

UPt_3 [1] and URu_2Si_2 [2] were the first two magnetically ordered superconductors discovered and are, more than 30 years later, still not fully understood and attracting a considerable scientific interest [3]. The investigation of systems associating uranium and a noble metal such as U-Pt-Si might thus be of interest to discover new phases with exotic physical properties. The seven ternaries already known in this system cover a wide range of magnetic behaviours, from paramagnetism ($U_3Pt_{23}Si_{11}$ [4]) to ferromagnetism ($UPtSi_2$ [5]) via more or less complex antiferromagnetism (UPtSi [6], UPt_2Si_2 [7], U_3Pt_5Si [4]) or spin-glass features (U_2PtSi_3 [8]). No magnetic data are available for $U_6Pt_{30}Si_{19}$ [4].

Our preliminary investigations [9, 10] of this U-Pt-Si system reveal an avalanche of at least 17 new ternary silicides in the isothermal section at 1173 K. On the one hand, it hampers the preparation of single-phase samples required to investigate their physical properties. On the other hand, it opens a wide range of possible behaviours, and will allow drawing some correlations between the physical properties and the crystallochemistry.

This presentation will focus on the first three intermetallics prepared with a satisfying purity for magnetic, electrical and specific heat characterizations: $UPtSi_2$, $UPtSi_3$ and $U_3Pt_{12}Si_4$.

$UPtSi_2$ was reported in 1992 by Sato et al. [5] but only roughly characterized. It crystallizes in the orthorhombic $CeNiSi_2$ structure-type (*Cmcm* space group, no. 63) with cell parameters a = 4.119 Å, b = 21.256 Å and c = 4.163 Å. A ferromagnetic ordering is observed below T_C = 89 K, with the characteristics of a hard anisotropic ferromagnet (fig. 1(a)). The calculated effective moment $\mu_{eff} = 2.5\ \mu_B$ carried by uranium atoms is in line with usual observations on U-based intermetallics and highlights a significant delocalization of the *5f* electrons in this compound. The electrical resistivity (fig. 1(b)) is dominated by a –logT temperature dependence above T_C characteristic of Kondo interactions while a sharp decrease occurs below T_C leading to a RRR ratio of about 40. The specific heat measurements (fig. 1(b)) only evidence moderate electron correlations with a Sommerfeld coefficient smaller than 50 mJ mol^{-1} K^{-2}. The overall physical behavior strongly resembles to that of the isostructural and isoelectronic $UNiSi_2$ [11].

$UPtSi_3$ adopts the orthorhombic $SmNiGe_3$ structure-type (*Cmmm* space-group, no. 65) with cell parameters a = 4.05 Å, b = 21.39 Å and c = 4.05 Å [4]. A very small contamination of the samples by the $UPtSi_2$ ferromagnet disturbs the magnetic measurements, but the absence of extra transition on the χ(T) curves, as well as the absence of peak on the specific heat data suggest a paramagnetic behaviour for this silicide. The Sommerfeld coefficient is strongly enhanced (> 100 mJ mol^{-1} K^{-2}) in comparison to $UPtSi_2$.

Finally, a platinum rich compound, $U_3Pt_{12}Si_4$, was found to crystallize in the anti-$Gd_3Ru_4Al_{12}$ structure-type (space-group *P6₃/mmc*, no. 194, a = 8.77 Å, c = 9.4 Å), similarly to $U_3Co_{12}Si_4$ [12] or $U_3Ni_{11.7}Si_{4.3}$ [13]. The magnetic and specific heat data agree with a Curie-Weiss paramagnetism of this phase, with a rather large effective moment (μ_{eff} = 3.2 μ_B) carried by uranium atoms. The ρ(T) curve is dominated by a Kondo like –logT shape above 25 K and the presence of a broad maximum around this temperature.

A discussion will be undertaken over the relation between the chemical composition, the crystal structure and the physical properties of the characterized phases in this system.

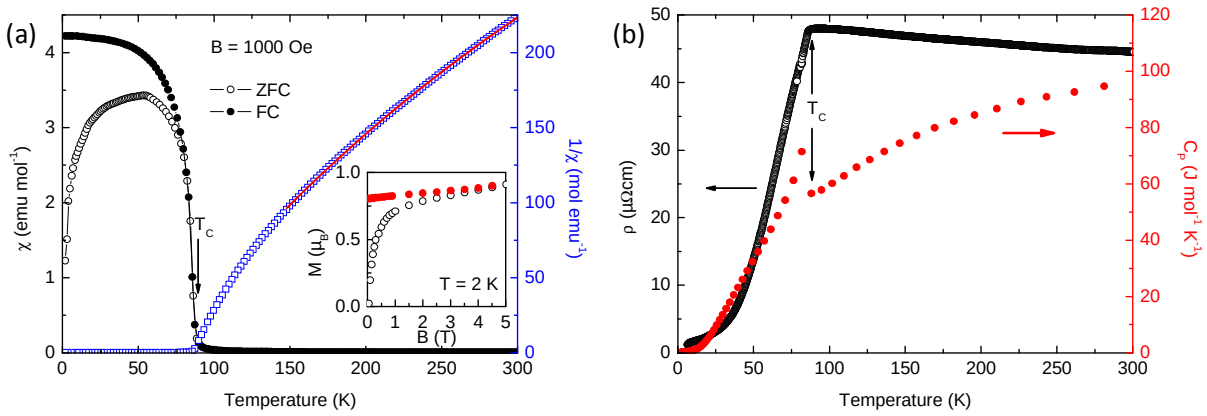

Fig. 1. (a) Thermal dependence of $UPtSi_2$ magnetic susceptibility (left axis) measured in the ZFC (open symbols) and FC (full symbols) modes and its inverse (right axis). The red solid line corresponds to the fit of the data to a modified Curie-Weiss law. The inset shows the magnetization isotherm measured at 2 K with increasing (open) and decreasing (full symbols) the magnetic field. (b) Thermal dependence of the electrical resistivity (left axis) and specific heat (right axis) of this silicide.

References

[1] G. R. Stewart et al., *Phys. Rev. Lett.*, **52**, 679 (1984) .
[2] T. T. M. Palstra et al., *Phys. Rev. Lett.*, **55**, 2727 (1985).
[3] Thomson Reuters Web of Science
[4] J.-N. Chotard et al., *J. Alloys Compd.*, **407**, 36 (2006).
[5] N. Sato et al., *J. Magn. Magn. Mater.*, **104-107**, 31 (1992).
[6] K. Prokes et al., *Physica B*, **225**, 166 (1996).
[7] H. Ptasiewiczbak et al., *Solid State Commun.*, **55**, 601 (1985).
[8] D. X. Li et al., *J. Magn. Magn. Mater.*, **176**, 261 (1997).
[9] J.-N. Chotard, Master thesis, Université Rennes 1 (2003).
[10] N. Brisset, PhD. Thesis, *in progress*.
[11] A. P. Pikul et al., *Phys. Rev. B*, **85**, 045113 (2012).
[12] A. Soudé et al., *J. Solid State Chem.*, **183**, 1180 (2010).
[13] A. Perricone, PhD. Thesis, Université Rennes 1 (2002).

P8

Superconductivity in $ThIr_2Si_2$

Krzysztof Domieracki and **Dariusz Kaczorowski**
Institute of Low Temperature and Structure Research, Polish Academy of Sciences

The compound $ThIr_2Si_2$ crystalizes with a tetragonal crystal structure of the $CaBe_2Ge_2$-type (space group *P*4/*nmm*). Its low-temperature physical properties were investigated by means of magnetization, electrical resistivity and heat capacity measurements, performed down to 0.35 K. The experiments revealed bulk superconductivity below T_c = 2 K. The obtained data indicate that $ThIr_2Si_2$ is a weakly-coupled type-II BCS superconductor.

Email of presenting author: d.kaczorowski@int.pan.wroc.pl

Long abstract: was not submitted

P9

Magnetic anisotropy of UO_2 via exchange bias studies of UO_2/Fe_3O_4 thin films

E. A. Tereshina[1], Z. Bao[2], L. Havela[3], S. Daniš[3], T. Gouder[2], R. Caciuffo[2]

[1]*Institute of Physics ASCR, Na Slovance 2, 18221 Prague, Czech Republic*
[2]*European Commission, Joint Research Centre (JRC), Institute for Transuranium Elements (ITU), Postfach 2340, DE-76125 Karlsruhe, Germany*
[3]*Faculty of Mathematics and Physics, Charles University, Ke Karlovu 5, 12116 Prague, Czech Republic*

Large magnetic anisotropy (MA) is essential for high-density magnetic storage. Control over MA can be carried out via pinning of a ferromagnetic (F) layer by an antiferromagnet (AF) in exchange bias (EB) [1] systems [2]. Evaluation of the exchange coupling in the AF/F bilayers enables to determine anisotropy constants of antiferromagnetic thin films [3]. We studied MA of UO_2 (bulk T_N is 30.8 K) using UO_2/Fe_3O_4 films prepared by dc sputter deposition. The thickness of UO_2 was varied from 40 to 300 Å while the thickness of Fe_3O_4 has been kept constant. Large EB ~2.5 kOe has been observed in $CaF_2/UO_2/Fe_3O_4$ (Fig. 1). The dependence of EB on the thickness of UO_2 showed that the exchange coupling and hence, the magnetic anisotropy in the CaF_2-based samples is nearly an order of magnitude stronger (10^7 erg/cm3) compared to that of a $LaAlO_3$-based system. This can be due to appearance of a magnetically dead [4] part of the LAO-based UO_2 layer whereas UO_2 grown on CaF_2 substrates is fully ordered.

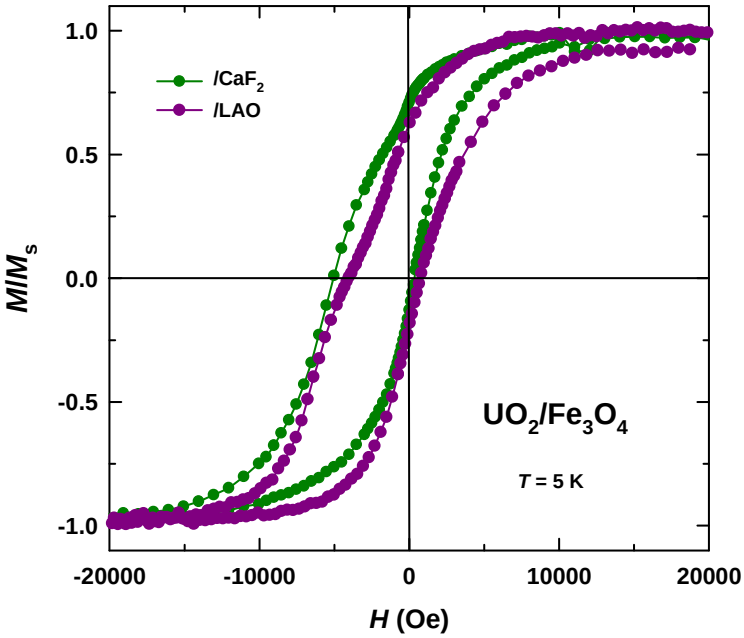

Fig. 1. Magnetization data for the UO_2/Fe_3O_4 bilayers on CaF_2 (001) and $LaAlO_3$ (001) substrates with a 150-Å thick layer of magnetite at 5 K after field cooling in 1 T.

References

[1] WH Meiklejohn and CP Bean, Phys. Rev. B, 102 1413, (1956).
[2] S. M. Zhou et al., Phys. Rev. B 69, 024408 (2004).
[3] D. Mauri et al., J. Appl. Phys. 57, 3047 (1987).
[4] Bao et al., Phys. Rev. B 88, 134426 (2013).

P10

Magnetism and hydrogen absorption in UNi(Zn,Al) system

S. Mašková[1], S. Daniš[1], K. Miliyanchuk[2], O. Stelmakhovych[3], B. Vondráčková[1], L. Havela[1]

[1] *Department of Condensed Matter Physics, Faculty of Mathematics and Physics, Charles University, Prague 2, The Czech Republic, e-mail: maskova@mag.mff.cuni.cz*
[2] *Faculty of Chemistry, Ivan Franko National University of Lviv, 79005 Lviv, Ukraine*
[3] *Department of Life Safety, Ivan Franko National University of Lviv, 79005 Lviv, Ukraine*

UNiZn is the first Zn containing UTX ternary with the ZrNiAl structure type. UNiZn polycrystalline sample was prepared by placing pure elements with the stoichiometry 1-1-1.02 into the quartz tube, which was sealed under argon atmosphere and subsequently inserted into the oven and heated fast to 500 °C, where it was held for 1 hour. After that the sample was heated fast to 1100 °C, where it was held for 26 min and subsequently cooled down at the rate 1 °C/min to 700 °C. At this temperature it was removed from the furnace.

XRD showed that UNiZn crystallizes in the hexagonal ZrNiAl type of structure (*P*-62*m*). The crystal structure parameters are summarized in table 1. The shortest inter-uranium distance (d_{U-U} = 3.43 Å) is in the basal plane, similar to most of other U-compounds with the same structure type.

The temperature dependence of magnetic susceptibility indicates that UNiZn has a paramagnetic ground state [1]. Magnetic susceptibility is low (≈ 10^{-8} m^3/mol) but temperature dependent (Fig. 1). Almost identical values in the field of 3 and 6 T evidence the absence of any ferromagnetic impurity. The shape of magnetic susceptibility does not allow us to speculate about any real Curie-Weiss contribution, the temperature variations are simply too weak. UNiZn can be considered as a spin fluctuator with its magnetic properties between two limiting cases, Pauli paramagnet and magnetically ordered material.

The non-magnetic ground state of UNiZn is corroborated by the results of the specific heat studies, which do not reveal any anomaly originating from magnetic order. As the low-temperature data (up to 20 K) exhibit linearity in the C/T vs. T^2 plot, we determined the value of the Sommerfeld coefficient γ using the relation $C = \gamma T + \beta T^3$. We obtained the parameters γ = 94 mJ/mol K^2 and β = 0.579 mJ/mol K^4 (corresponding to Debye temperature Θ_D = 220 K).

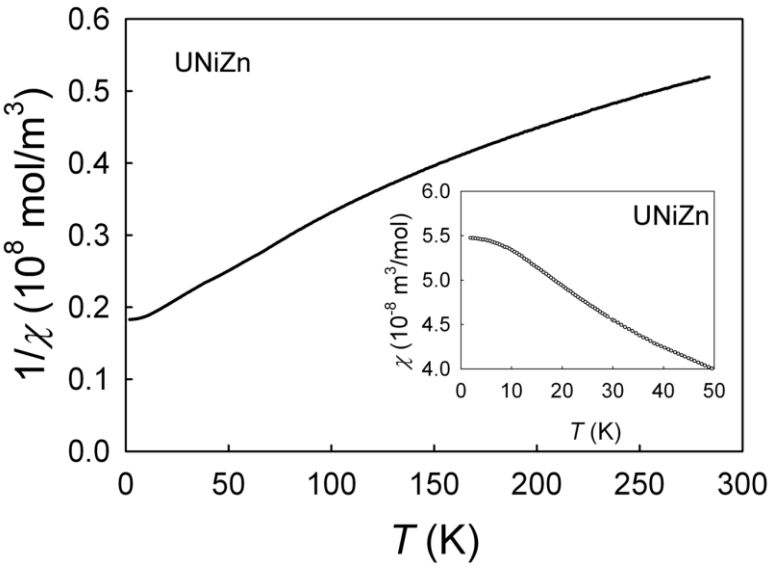

Fig. 1. Temperature dependence of inverse magnetic susceptibility measured in external magnetic field $\mu_0 H$ = 3 T. The inset shows the low temperature part of magnetic susceptibility of UNiZn measured in $\mu_0 H$ = 3 T.

As UNiZn properties seem to be close to the onset of magnetism we decided to perform the hydrogen absorption experiment. The hydrogenation of UNiZn was performed at hydrogen pressure 120 bar by heating up to T = 473 K and subsequent cooling with the rate 0.5 K/min. The amount of absorbed hydrogen estimated from the weight change was found out to be 2.3 H/f.u. The value of absorbed hydrogen is identical to the value for the γ-hydride of UNiAl, namely $UNiAlH_{2.3}$, which points to a similarity to this hydride studied in the past [2,3].

The crystal lattice is expanded in such way that the shortest U-U distance is now higher than the Hill limit what allows magnetic ordering in the hydride. $UNiZnH_{2.3}$ exhibits a cusp in $\chi(T)$ indicating AF ordering around 55 K. The γ-value increases from 94 mJ/mol K^2 in UNiZn to 100 mJ/mol K^2 in the hydride. This tendency is opposite than for UNiAl (164 mJ/mol K^2 in UNiAl and 60 mJ/mol K^2 in $UNiAlD_{2.1}$ [4]). The variation of the γ–coefficient of electronic specific heat is in general expected to culminate somewhere close to the onset of magnetism, which is placed between non-magnetic UNiZn and antiferromagnetic UNiAl (green line in fig.2).

We have synthesized the series of $UNiZn_{1-x}Al_x$ compounds to prove this statement. We have found that the magnetic order sets in between 10 and 30 at.% Al. We have analyzed the Sommerfeld coefficient of specific heat in the paramagnetic state (reaching 360 mJ/mol.K^2) and for T = 0, where reduced values up to 190 mJ/mol.K^2 reflect the band splitting. The results of our study show that indeed the value of γ–coefficient of electronic specific heat culminates somewhere close to the onset of magnetism (fig.2). This tendency cannot be explained by the variation of the lattice parameters within the series as a-parameter increases and c-parameter decreases almost linearly with increasing Al concentration (fig. 3).

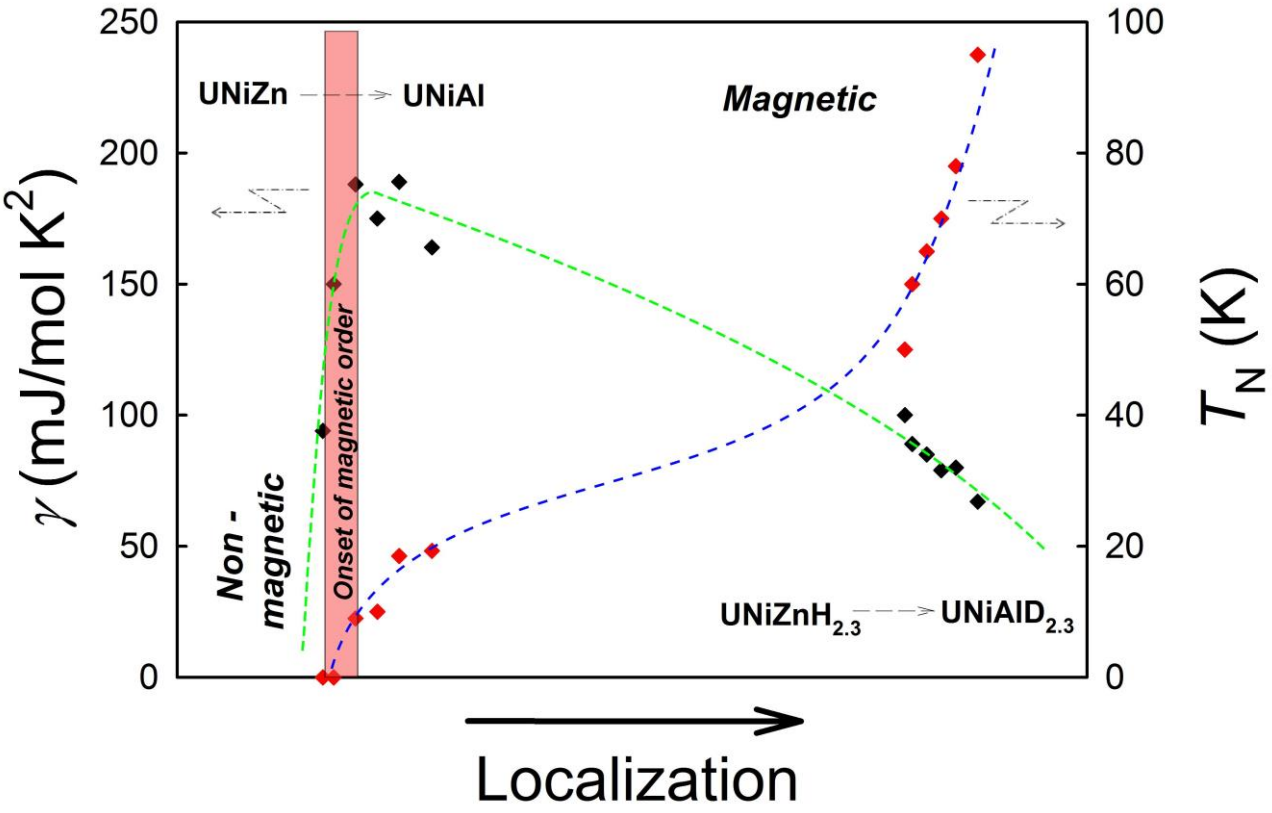

Fig. 2. Schematic representation of localization variations affecting the γ-coefficient (black diamonds) and ordering temperatures (red diamonds). Individual compounds were placed rather arbitrarily on the Localization axis, being inspired by the respective distances between the precursor compounds proportional to the Al concentration and between the precursor and its hydride.

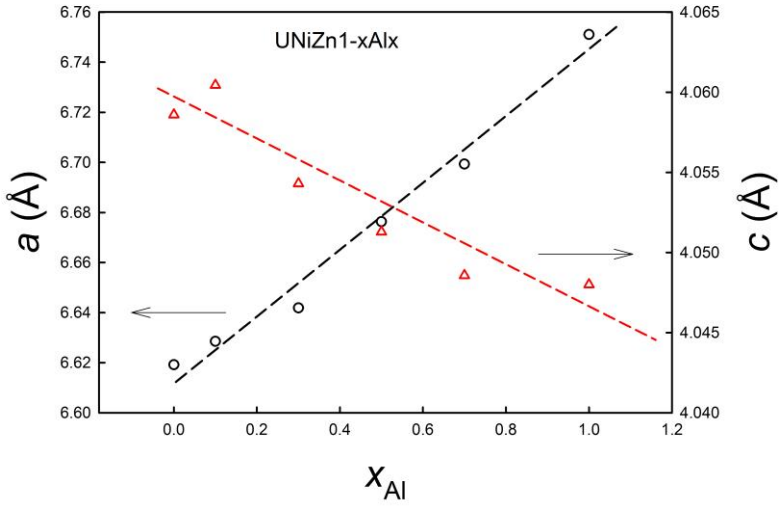

Fig. 3. Concentration dependence of the lattice parameters of $UNiZn_{1-x}Al_x$.

The hydrogenation of all compounds from the series was performed at hydrogen pressure 100 bar by heating up to T = 473 K and subsequent cooling with the rate 0.1 K/min. The amount of absorbed hydrogen estimated from the desorption experiment was found out to be around 2.3 H/f.u. similar to the amount of H absorbed by the terminal phases. Upon hydrogenation the Néel temperature is shifted to higher temperatures (fig. 4). For the non-magnetic $UNiZn_{0.9}Al_{0.1}$ antiferromagnetic order is induced by the hydrogen absorption. The value of Sommerfeld coefficient of specific heat for the hydrides is decreasing with increasing Al-concentration which is relevant for the presented scenario.

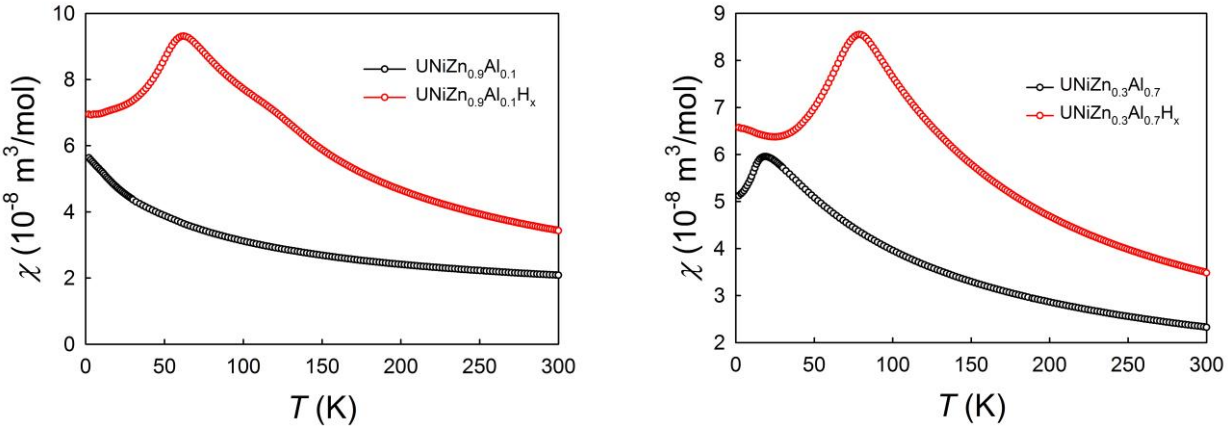

Fig. 4. Temperature dependence of magnetic susceptibility measured in external magnetic field $\mu_0 H$ = 3 T for $UNiZn_{0.9}Al_{0.1}$ (left) and $UNiZn_{0.3}Al_{0.7}$ (right) and their hydrides.

Acknowledgements

This work was supported by the Czech Grant Agency under the Grant No. 14-28190P. Experiments were performed at MLTL (http://mltl.eu/), which is supported within the program of Czech Research Infrastructures (Project No. LM2011025).

References

[1] S. Mašková, S. Daniš, K. Miliyanchuk, O. Stelmakhovych, B. Vondráčková, A.V. Kolomiets, L. Havela, *J. Alloys Compd.* **646**, 885-892 (2015).
[2] H.N. Bordallo, H. Nakotte, A.V. Kolomiets, A. Christianson, L. Havela, A.J. Schultz, H. Drulis, W. Iwasieczko, *Physica* B **276-278**,706 (2000).
[3] T. Yamamoto et al., *J. Alloys Compd.* **269**, 162 (1998).
[4] L. Havela,K. Miliyanchuk, A. Kolomiets: *Int. J. Mat. Res.* **100**, 1182-1186 (2009).

P11

Pressure-Induced Structural Behavior of CeNi

Vladimir Matvienko, Alexey Mirmelstein, Andrey Podlesnyak, Georg Ehlers, G. Halder
RFNC-VNIITF

Pressure-induced volume-collapse structural phase transition in the intermediate-valence compound CeNi is investigated by x-ray and neutron powder diffraction techniques. The structure of pressure-induced CeNi phase is shown to belong to the *Pnma* space group. Equations of state for CeNi before and after the transition are derived and an approximate *P-T* phase diagram is suggested. The observed *Cmcm* - *Pnma* structural transition is analyzed using density functional theory calculations which successfully reproduce the ground state volume, phase transition pressure, and the volume jump due to the transition.

Email of presenting author: mvn1969@mail.ru

Long abstract: was not submitted

P12

Unusual temperature dependence of Mössbauer isomer shift in NpF4

Itzhak Halevy.
Physics Department, Nuclear Research Center – Negev, P.O.Box 9001, Beer-Sheva, ISRAEL

We report on unusual temperature dependent Mössbauer isomer shift in the monoclinic NpF_4. The crystallographic parameters from the fitted spectra utilizing Rietveld analysis are a=12.7234(5)Å, b=10.8840(5)Å, c=8.3621(5)Å with β=126.15°. There are 8 fluorides nearest neighbors in anti-prism structure.
Since the low symmetry of the NpF_4 we can be sure from the X-Ray diffraction that no NpO_2 is present.
When lowering temperature from 44 to 4.2K the center of gravity of the Mössbauer spectra of the 60 keV, shifts positively by 1±0.05 mm/sec, indicating a decrease of the *s* electrons density at the Np nucleus. This behavior of NpF_4 hints an increase in the volume when reaching low temperature, in a surprising agreement with Neutron inelastic scattering on other AnF_4. The Mössbauer spectra show asymmetry. Susceptibility measurements indicate that this compound is paramagnetic down to 4.2K. Thus paramagnetic relaxation phenomena within the ground Kramers doublet could explain this asymmetry.

Email of presenting author: halevy.itzhak.dr@gmail.com

Long abstract: was not submitted

P13

Recent developments in UCx-based spallation targets at C^2TN

S. Chowdhury,1 M.S. Henriques,1,2 A. Cruz,1 T. Stora,3
1 C2TN, IST, Univ. Lisboa, Bobadela LRS, Portugal, 2 Institute of Physics, ASCR, Prague, Czech Republic, 3 CERN, Genève, Switzerland

Radioactive ion beams at ISOLDE, CERN, are produced by the interaction between an intense proton beam with a thick target material. The target should operate at high temperatures and must instantly release the new isotopes. Bulk, micrometric, UC_x-based targets are the current reference at ISOLDE, but a significant increase on the release and yields of exotic isotopes can be obtained on submicron and nanostructured porous materials. Recently we succeed in producing submicron structured UC_x by electrospinning at C^2TN. However, improved set-up facilities are needed for a better control of the parameters that affect the electrospinning process.

Here we present the recent advances at C^2TN for the production of UC_x-based materials for spallation targets. A new electrospinning system, with controlled atmosphere, was developed and mounted. The system was tested by the preparation of nanostructured lanthanide carbides. Different precursors, as acetates, acetylacetonates and citrates, were used.

Email of presenting author: apg@ctn.ist.utl.pt

Long abstract: was not submitted

EXPERIMENTAL STUDY of SHAPE MEMORY EFFECT in U6.3wgt.%Nb ALLOY

A.V.Troshev, A.M.Golunov, D.A. Chentsov, A.V. Baluev, A.E. Shestakov

Federal State Unitary Enterprise
"Russian Federal Nuclear Center -
Zababakhin All-Russia Research Institute of technical Physics
(FSUE "Zababakhin RFNC-VNIITF")
atroshev@mail.ru

The work presents the results of investigation into the shape memory effect (SME) in U-6.3wgt.%Nb alloy (α″-phase). In order to change samples shape, compression deformation was used. The samples were compressed at a room temperature with a velocity ~10^{-3} s^{-1}. The value of plastic deformation was from 2.5 up to 17%. The samples in the initial state and after deformation were heated in dilatometer and in a high-temperature attachment of diffractometer. The result of investigation showed that with the heating, the shape of deformed samples is recovered completely or partially. The work gives comparison of the results with foreign literature data on the study of SME in uranium-niobium alloy and discussion of SME mechanism in the alloy under study.

Introduction

The shape memory effect (SME) is a phenomenon typical of some materials and consisting of returning to initial shape under the heating after preliminary plastic deformation. The alloys with martensitic structure demonstrate the best results on deformation returning. Elementary act of plasticity in such alloys is performed at the cost of reversible martenssitic transformation, elastic twinning and reorientation of martensitic crystals. Today, many alloys with SME are used in the devices of automatics, medicine, aeor-space industry etc. The most bright example of an alloy with SME is the alloy TiNi ("Nitinol"), in which plastic deformation from 6 up to 8% under the heating via the region of reversible martensitic transformation can be recovered completely.

Alloy of uranium with niobium have several features that are appropriate of the materials with SME. In particular, the alloy U-6.3wgt.%Nb under quenching undergoes the following sequence $\gamma_1 \rightarrow \gamma^\circ \rightarrow \alpha''$ of martensitic transformations, the latter is accompanied by reaction of ordering, and the main mechanism of the alloy deformation in the process of phase transitions is mechanical twinnning.

The first information about SME in the range of the alloys of uranium with niobium appeared in the end of 70-s. But today, it is possible to firnd only several publications devoted to experimental study of SME in the alloys of uranium with niobium with martensitic structure [1,2]. According to [2], ~5% of deformation of the alloy U-6wgt.%Nb can be practically completely recovered as the result of heating up to 800°C. High value of deformation recovery, which comparable to SME of the alloys that are widely used (TiNi), transfers the results of SME investigation in the alloys of uranium with niobium from scientific plane to practical one.

The aim of this work is to continue investigation of SME in the alloy U-6.3wgt.%Nb in the state of martensitic α″-phase.

While setting the studies, the same approach was used that was mentioned in [1,2]. It consists in deforming the samples at a room temperature and their subsequent heating in dilatometer in order to determine the value of deformation recovery by the change of the sample linear size. Deformation of the samples was made at a room temperature at the same rate as in [1,2], i.e. ~10^{-3} s^{-1}. The difference of this

work consisted of the direction of the sample deforming and the rate of heating in dilatometer. Thus, in [1,2], the samples were deformed by tensile, and in our work, it was made by compression. Besides, in our work, the heating rate of deformed samples was ~600 times lower than in [2], and made ~2°C/min.

Experimental equipment and samples

The samples of cylindrical shape with diameter 6 mm, length 25 and 12 mm were cut from a massive blank of alloy U-6.3wgt.%Nb that was subjected to special heat processing in order to obtain an alloy in the state of martensitic α′′-phase. Deformation of the samples was performed on universal test machine LFM-50, dilatometric measurements – on dilatometer NETZSCH DIL-402C, and X-ray diffraction analysis – on diffractometer ARL′XTRA.

The result of studies

Fig. 1 shows the alloy σ-ε diagrams that were obtained under samples deformation by compression. As the result of mechanical tests, a set of samples was obtained. These samples differed by the degree of deformation (residual deformation was: ~1.7; ~4.7; ~8.3; ~10.8 and ~15.3%).

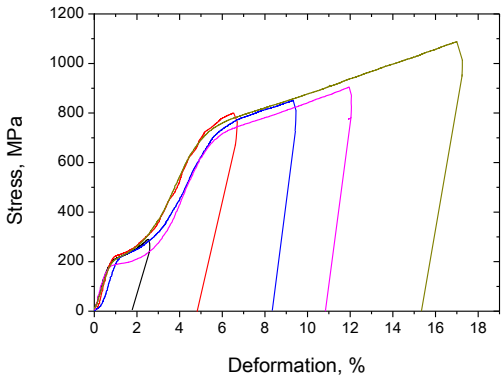

Fig. 1 Deformation curves obtained under compression of samples out of U-6.3wgt.%Nb.

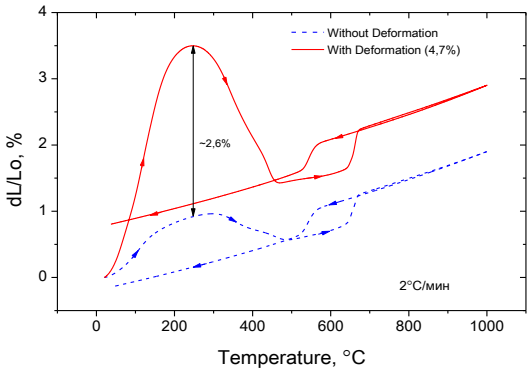

Fig. 2 Dilatograms of the samples out of U-6.3wgt.%Nb (without deformation and with deformation on 4.7%).

Under testing of one sample out of the alloy (with residual deformation ~4.7%), it was revealed that the heating in the interval from 25 up to ~250°C is accompanied by abnormally high (in comparison with the samples without deformation) elongation (Fig. 2).The heating higher than ~250°C causes the sample compression that continues up to the alloy transition in equilibrium state (at T~500°C). As far as the direction of the sample size change in this case appeared to be opposite to the direction that was expected, i.e. not related to deformation recovery by compression, the further experiments on dilatometer were optimized in order to reduce experiment duration. At a later stage, the sample heating was made in a narrower interval of temperatures – from 25 up to 250°C.

Fig. 3 shows dilatometric curves obtained under the heating of the samples with different degree of the sample elongation, and a portion of recovered deformation was calculated by the following formula:

$$\eta\,(\%) = \frac{\left(\frac{dL}{L_0}\right)^T_д - \left(\frac{dL}{L_0}\right)^T}{\varepsilon} \cdot 100, \qquad (1)$$

where $\left(\frac{dL}{L_0}\right)^T_д$, % – maximum elongation of deformed sample; $\left(\frac{dL}{L_0}\right)^T$, % – maximum elongation of the sample without deformation; T – temperature of achieving maximum elongation; ε, % – residual deformation of the sample.

Fig. 4 shows the results of calculation according to the formula (1) for a portion of recovered deformation depending on the degree of the sample deformation. Fig. 4 shows that with increasing the deformation, the portion of deformation, which was recovered under heating, quickly decreases. The portion of deformation recovery close to ~100% can be obtained only in case, if residual deformation does not exceed ~2%.

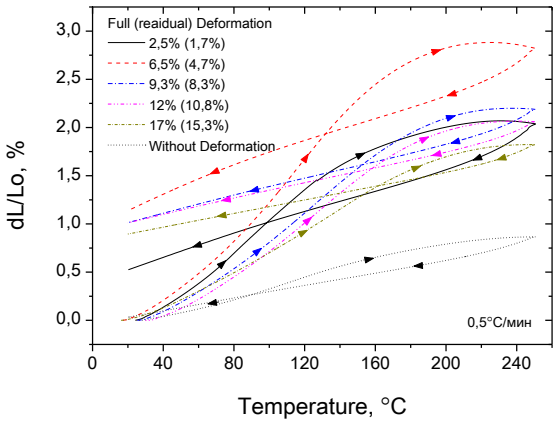

Fig. 3 Dilatograms of the samples out of U-6.3wgt.%Nb deformed by compression with various degree.

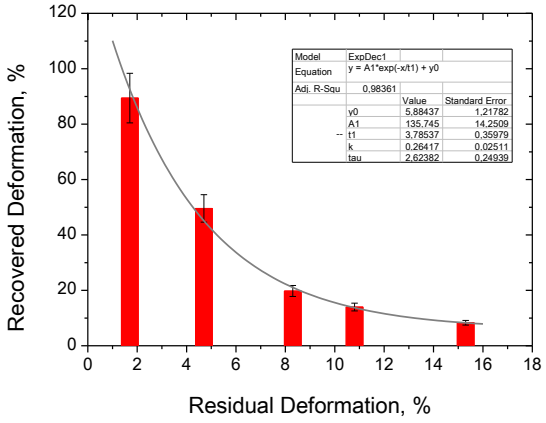

Fig. 4 Deformation portion recovered under heating up to the temperature 230…250°C.

Using the same formula (1), experimental data that were presented in [2] were processed. For calculation, we took the sample elongation corresponding to the temperature ~240°C, like it is shown in Fig. 5. Fig. 6 shows correlation of the data obtained in our work and in [2]. Fig. 6 shows that despite existing differences in experiment set-up, compared data have good agreement. This points to a single mechanism of deformation recovery under the alloy heating in the interval of the temperatures from 25 up to ~250°C, regardless of deformation direction and heating rate.

In [2] ~40% of deformation introduced in the sample (~5.2%) was recovered additionally as the result of the alloy heating in the interval of the temperatures from ~250 up to 800°C. In our experiments, we did not observe that. The samples were compressed under the heating in this temperature interval (Fig. 2).

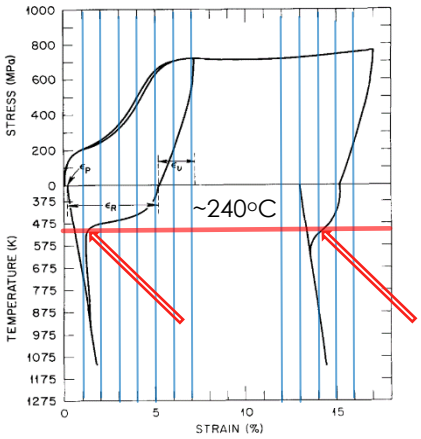

Fig. 5 Deformation curves obtained by stretching and annealing of the samples out of α′′-alloy U-6at.%Nb [2].

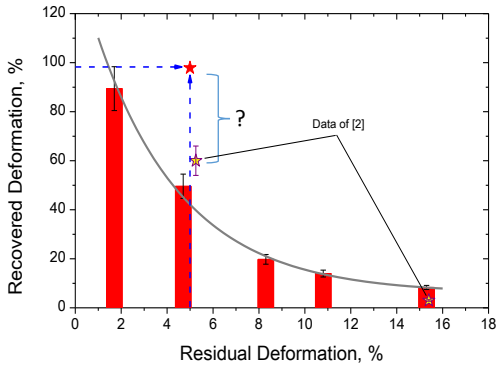

Fig. 6 Comparison of the results obtained in our work and in [2].

Investigations performed in high-temperature attachment to diffractometer (Fig. 7) showed that beginning from ~150°C, the alloy undergoes α′′→γ°-phase transition, which is accompanied, as it is seen in Fig. 8, by the sample compression (in both cases, the samples were used without deformation). It follows that in [2], where the samples were deformed by tensile, the direction of the sample size change under the impact of deformation recovery mechanism coincided with the direction of size change under phase transition. That is why, it is quite possible that the value of SME declared in [2] is the sum of the sample size change both at the cost of deformation recovery mechanism, and at the cost of the alloy phase transition.

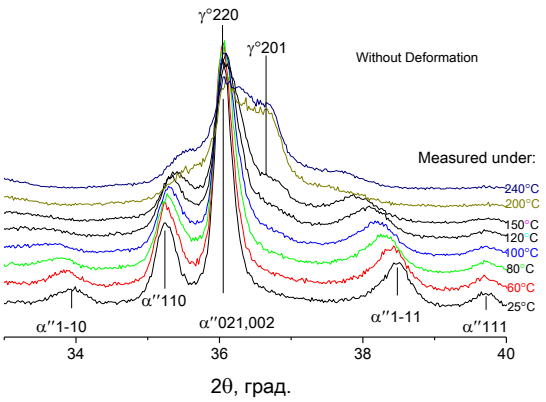

Fig. 7 The results of X-ray diffraction analysis for U-6.3wgt.%Nb in high-temperature diffractometer attachment.

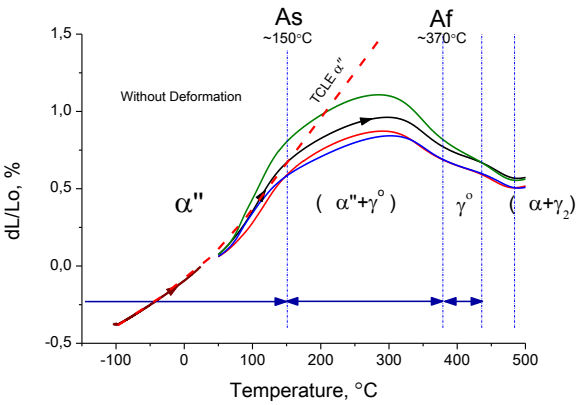

Fig. 8 Elongation of the samples out of U-6.3wgt.%Nb in the interval of α′′→γ°-transition (TCLE – temperature coefficient of linear expansion).

About SME mechanism

The majority of investigators suppose that the basis of SME mechanism is reversible reorientation of martensitic crystals under the impact of applied stress. As a rule, the boundaries of crystals, which are generated as the result of crystal martensitic transformation, are coherent and hence mobile. They easily displace both under the impact of stresses, and under temperature impact. But this does not mean that martensitic crystals can rearrange endlessly. At a certain level of applied stress,

in a crystal lattice of the alloy, the process of plastic deformation begins to dominate dislocation mechanism. Dislocations impede displacement of crystal boundaries and in the long run, block them.

Fig. 9 shows deformation curves (obtained by tensile) for the alloy Ti-50.6at.%Ni, which is in martensitic state [3]. Here, one can see data on deformation recovery as the result of heating up to 373K (higher than the temperature of austenitic transformation start). Investigation of the samples of Ti-50.6at.%Ni in electron microscope permitted to determine several mechanisms of the alloy deformation (Stages I, II, III).

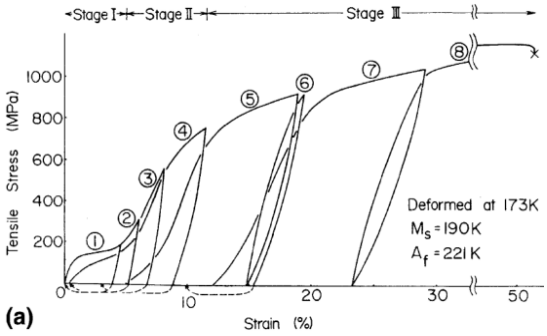

Fig. 9 Deformation curve for Ti-50.6 at.%Ni [3]. Dashes show deformation recovery under the sample heating up to 373K.

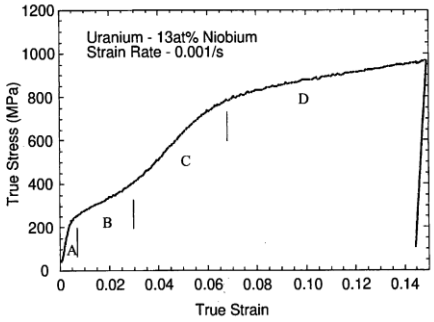

Fig. 10 Typical sections on the deformation curve of U-5.5wgt.%Nb [4].

Fig. 9 shows that complete deformation recovery under heating is possible only after the alloy deformation by the value enclosed in the boundaries of the first stage (Stage I). Deformation by higher value (Stage II, III) led to decreasing recovered deformation under heating.

Similar approach was used in [4], while studying an alloy U-5.5wgt.%Nb. The alloy samples without deformation and in deformed state (deformation by compression by a value ~2.5 and ~4.5%) were examined in electronic microscope. As the result, several stages of deformation were revealed. They are shown in Fig.10, as sections A, B, C and D. To opinion of authors in [4], section A corresponds to elastic deformation of martensite, section B – to deformation caused by reorientation of martensitic crystals, section C – to elastic deformation of crystals (mono domains) oriented to the direction of applied stress, and section D – to the alloy deformation by dislocation mechanism. Fig. 10 shows that extension of section B, which is related to reorientation of martensitic crystals, is limited by deformation value~3%. Following the logics of [3], this is deformation value, which can be completely recovered under heating.

By analogy, deformation curves obtained in our work (Fig. 1) can be split in typical sections A, B, C and D. Fig. 11 shows the typical curve of the alloy deformation indicating these sections. Section B in this case is limited by the value ~2,6% (complete deformation).

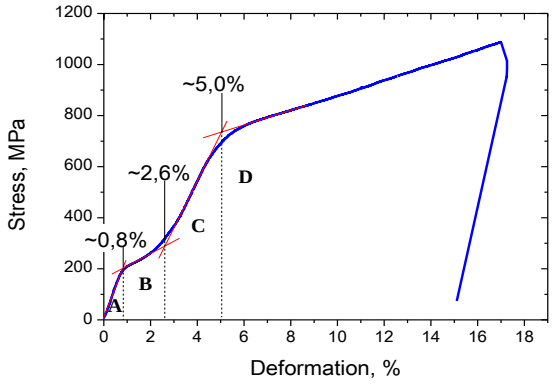

Fig. 11 Typical deformation of U-6.3wgt.%Nb obtained in our work.

As it is seen in Fig. 4, this value almost coincides with the value of maximum recovery of deformation obtained in the current work.

CONCLUSION

It was shown experimentally that alloy U-6.3wgt.%Nb in the state of martensitic α′′-phase has SME. The value of plastic deformation, which can be practically completely recovered under heating, does not exceed 2…3%. With increasing the degree of deformation, the value of deformation recovery quickly decreases. This is related to the change of deformation mechanisms. If the alloy deformation up to ~3% is related mainly to reorientation of martensitic crystals, then deformation by a big value is conditioned by such irreversible processes as formation and sliding of dislocations.

Two-fold difference between the value of deformation, which is recovered under heating in our work and in [2], is explained by codirectional (in work [2]) change of the sample size as the result of reverse reorientation of martensitic crystals (deformation recovery) and alloy $\alpha'' \rightarrow \gamma^{\circ}$ phase transition.

1. R.A. Vandermeer, J.C. Ogle, and W.B. Snyder. Shape Memory Effect In A U-14at.%Nb Alloy. Scripta Metallurgica. Vol.12, 1978, p. 243-248.
2. R.A. Vandermeer, J.C. Ogle, and W.G. Nortcutt. A Phenomenological Study of the Shape Memory Effect in Polycrystalline Uranium-Niobium Alloys. Metallurgical Transactions A. Vol. 12A, 1981, p. 733-741.
3. K. Otsuka, X. Ren. Physical metallurgy of Ti–Ni-based shape memory alloys. Progress in Materials Science 50 (2005), p. 511-678.
4. R.D. Field, D.J. Thoma, P.S. Dunn, D.W. Brown and C.M. Cady. Martensitic Structures and Deformation Twinning in the U-Nb Shape-Memory Alloys. Philosophical Magazine A, 2001, Vol. 81, No. 7, p. 1691-1724.

P15

Localized corrosion behaviour of uranium based materials

L. Costelle,[1] R. Springell[1], P. Martin[1], R. Burrows[2], T. Scott[1]

[1] *Interface Analysis Centre, School of Physics, University of Bristol, Bristol BS8 1TL, United Kingdom, e-mail: leila.costelle@bristol.ac.uk*

[2] *National Nuclear Laboratory, Chadwick House, Warrington Cheshire WA3 6AE, United Kingdom*

The corrosion of uranium by hydrogen is a destructive process. The principal reaction involves the formation of a metal hydride precipitate which has a lower mass density than that of the parent metal and has been observed to follow a localized, spatially heterogeneous, and random pattern of initiation on uranium surfaces. However, electrochemically, there is a lack of understanding of these localized processes in uranium, because of the difficulty associated with the tiny current from the nucleated pits, which is always swamped by the overall passive current from the surface, and the difficulty to identify the time of initiation or the location of a single attack among many.

Conventional macro-electrodes are not suited for the study of these mechanisms as they tend to dilute the responses evident in the localised processes. However, the use of microelectrodes, based on uranium thin films, enabled us to isolate the effect and investigate it without the parallel response of a surface undergoing an entirely different reaction.

P16

A novel layer type for the first compound in the Strontium Uranium oxifluoride system

Laurent Jouffret, Jean-Michel Hiltbrunner, Marc Dubois
ICCF

Before its isotopic enrichment, uranium is chemically treated in order to produce uranium hexafluoride. This uranium contains some impurities that can lead to the formation of mixed compounds. Any addition of oxygen in the system will lead to the presence of uranium or mixed oxifluoride compounds. However, very few of the simple uranium fluorides and oxifluorides have been crystallographicaly described in the literature. Most were described during and after the Manhattan project by Zachariasen, and few after. Several oxifluoride compounds have been described with other monovalent or divalent cations but none with Sr. Here we will describe the first Strontium uranium oxifluoride compound that exhibits a novel layer type. We will demonstrate its novelty through crystallographic and spectroscopic characterizations (FTIR and NMR) on the compound, as well as its thermal behavior.

Email of presenting author: laurent.jouffret@univ-bpclermont.fr

Long abstract: was not submitted

P17

Uranium wet oxidation under contained conditions

Antonios Banos, Tom Scott
University of Bristol, Interface Analysis Centre, School of Physics, HH Wills Physics Laboratory, Tyndall Avenue, Bristol, BS8 1TL, United Kingdom

Uranium hydride has been identified as a potential reaction product of H_2O corrosion. The highly pyrophoric and unstable nature of UH_3 in air poses considerable environmental risks, due to potential radionuclide release. In this work we try to simulate the corrosion conditions by immersing an initially polished U-sample in H_2O under vacuum contained conditions. The binary system is being investigated in different temperatures with two main questions awaiting to be answered: 1. Is UH_3 identified? For this reason post-examination of the reacted surface is being conducted using SIMS and FIB milling and sectioning. 2. If UH_3 is identified, on which part of corrosion period is it produced? Kinetics of the reaction is being monitored using a specifically designed set-up comprised from a stainless steel pot and a data log pressure controller. Temperature programmed desorption is being conducted on the reacted samples in order to analyze the emerging gases and validate our results.

Email of presenting author: ab13306@bristol.ac.uk

Long abstract: was not submitted

P18

Synthesis and Characterisation of Accident Tolerant Fuels

Eleanor Lawrence Bright, Tom Bligh Scott, David Goddard, Ross Springell
UoB, NNL

Accident tolerant fuels (ATFs) are being developed with the motivation of having an improved safety response to accidents compared to UO_2 as well the economic benefit of increased uranium density, allowing for either higher burnup or lower enrichment. The standout potential ATFs are UN and U_3Si_2, both having higher thermal conductivity and uranium density than UO_2. UN is the better of the two in these categories, but the large cross-section of ^{14}N and issues due to ^{14}C formation could require ^{15}N enrichment. The lower melting point of U_3Si_2 compared to UO_2 and UN is offset by the relatively high thermal conductivity which increases with temperature. Both are known to be more reactive with water compared to UO_2 but a better understanding of the fuel-water interaction is required to assess their potential as ATFs. Here, we will present our first results on the synthesis and characterisation of uranium nitride.

Email of presenting author: e.lawrencebright@bristol.ac.uk

Long abstract: was not submitted

P19

Polygonisation of UO_2 high-burn-up fuel investigated by micro-X-ray diffraction

Mélanie Chollet,[1] Johannes Bertsch[1], Daniel Grolimund[2]

[1] *Paul Scherrer Institute, NES, 5232 Villigen, Switzerland, e-mail: Melanie.Chollet@psi.ch*
[2] *Paul Scherrer Institute, Swiss Light Source, 5232 Villigen, Switzerland*

During operation, uranium dioxide fuel undergoes consequent microstructural changes due to irradiation processes and fission element production that have to be accommodated in the matrix. This induces consequently many lattice defects including dislocations, porosity formation *via* fission gas accumulation, and grain subdivision. Above a certain burn-up threshold, commonly accepted to be around 55-65 GWd/tU, the accumulation of such lattice defect leads to the formation of the so-called high-burn up structures (HBS). They developed at the rim of the fuel pellet favored by the lower prevailing temperatures that prevent thermal healing like it is assumes to be the case in the center of the pellet. Those HBS are nowadays well characterized by electronic microscopy means however their mechanisms of formation are still not fully understood. Concerning small grain formation for example, it is not clear yet if the tangled-up dislocations act as nucleation sites for new grain growth or if the dislocations reorganize forming new subgrains, also called the polygonization process. The first case gives rise high-angle recrystallized grain shape, whereas the later produce low angle grain shape. Both types of grains are generally observed in HBS [1].
Mieszczynski *et al.* [2, 3] have shown that micro-X-ray diffraction (XRD) is a powerful tool to investigate UO_2 fuels or derivative (chromia-doped and MOX) polygonization. Indeed, as long as the grain is ideal, reflections appear as well defined Laue spots, grain size being larger than the micro-focused beam size. These spots start to deform into elongated or even more streaking spots when the grain is strained or start to devise into small sub-crystallites under the effect of dislocations. With this method, the authors were able to evaluate the number of subgrains per grain as a function of burn-up. If a tendency could be obtained from their results, the variety of the investigated samples renders a clear interpretation not straightforward. The Nuclear Fuel group of PSI tackled the project of investigated a coherent series of UO_2 fuel irradiated at various burn-up. We report here the results obtained by micro-X-ray diffraction (XRD) performed at the microXAS beamline of the Swiss Light Source (SLS) on the two end-members of the series, i.e. a fresh non-irradiated UO_2, or reference sample and a 9 cycle sample which constitute the starting point of the study.

The UO_2 fuel series were manufactured by Westinghouse and irradiated at the Leibstadt boiling water reactor (Switzerland). The high-burn sample irradiated during 9 cycles reaches a burn-up of 78.8 GWd/tU. The rod was cut and the slice selected at the hotlab facility of PSI (Figure 1(a)). Because of its high radioactivity, sub-samples have been prepared to respect the microXAS beamline activity limit. In this purpose, the pellet surface was carefully grinding and freed particles were collected on an adhesive kapton foil (Figure 1 (b)). In this replicate method, the microstructure could be investigated along the pellet radius and the effect of temperature evaluated.
The fresh non-irradiated sample was prepared by Focused Ion Beam (FIB) method to reach the suitable window thickness of 23 μm optimized for transmission measurement.

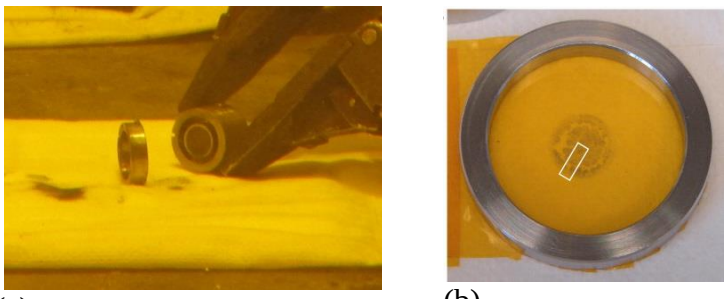

(a) (b)

Figure 1: (a) Irradiated rod cut in the shielded cell of PSI hotlab. (b) Freed particles of the UO_2 pellet surface collected on a kapton foil.

The XRD measurements were performed in the transmission mode on the microXAS beamline of the Swiss Light Source. The beam was focused to 1 x 2 μm^2 size by Kirkpatrick-Baez mirrors. The energy was chosen at 17.5 keV, just above the L_{III} absorption edge of Uranium (17.166 keV). Irradiated fuel particles were localized by X-ray fluorescence mapping of the kapton adhesive. The biggest particles, from 5 to 50 μm size were selected along the whole pellet diameter to be finely investigated by microXRD mapping. Maps were generally measured with 1 μm step in both X and Y direction using the marCCD. Calibration of sample-detector distance and other experimental parameters were fitted using standard Al_2O_3 powder patterns measured in the same experimental geometry. Standard deviations are ranged between 0.001 and 0.004 Å for d-spacing varying from 1.0 to 3.5 Å.

Figure 2 exposes typical examples of 2D patterns obtained from the non-irradiated UO_2, from the center of the irradiated pellet and from the periphery region (Figure 2a, b and c respectively). As expected according to the given grain sizes of 10 μm size, well-defined diffraction spots (Laue-type) appear on the 2-D pattern of the pristine UO_2. On the contrary, powder-like signal is coming from the irradiated periphery and center zone sample. This indicates that grains are well smaller than the beam, i.e. nanometric-magnitude size. Thus, at this high-burn up, polygonisation processes in the whole pellet even in the center, where it was not expected. Indeed, higher temperatures prevailing in the center zone than in the periphery of the pellet should heal the defects and favor large grain size. For further analysis, central pellet temperature has to be defined. However, our observation of a fully-restructured pellet is supported by the previous study of Ledergerber *et al.* [4] in which sub-micrometric grains in cavities were revealed by SEM imaging for a $r/r_0 = 0.05$ (r being the position along the radius) in a sample coming from the same rod.

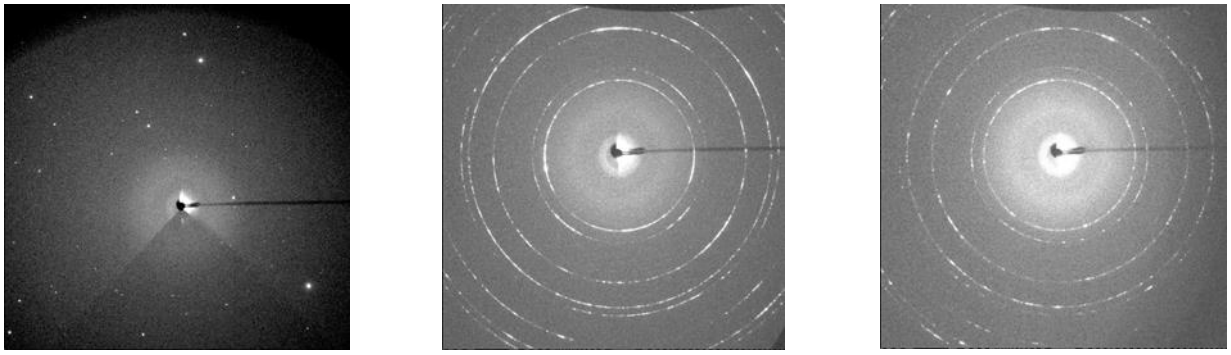

(a) (b) (c)

Figure 2: 2D-XRD typical patterns of (a) fresh non-irradiated UO_2, (b) the irradiated pellet center and (c) the irradiated pellet periphery.

To quantify the evolution of the microstructure as a function of the radius pellet, in other words, as a function of temperature, peak-fitting of selected peaks, (111), (311), (200) and (220) using a

pseudo-Voigt profile function, was performed individually with the peak deconvolution mode of the XRDUA software [5]. Several patterns of twelve representative particles were finely analysed with pellet radial positions r/r_0 varying from 0.01 to 0.78. The evolution of the d-spacing are represented in the figure 3.

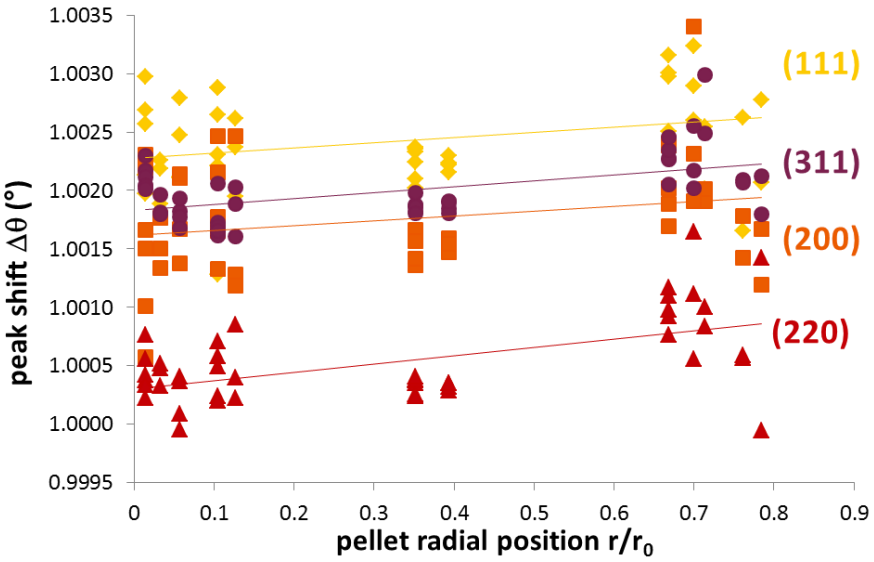

Figure 3: Evolution of the d-spacings of the (111), (311), (200) and (220) peaks normalized to reference sample values as a function of the pellet radial position.

The d-spacing values were normalized to the reference values to facilitate the comparison in between peaks. For all the studied reflections, there is a general increase of the d-spacing values towards the periphery of the pellet up to an r/r_0 value of 0.78. This certainly indicates, although it was not obvious from qualitative analysis that defects accumulate at the periphery zone of the pellet. This constant increase of the lattice constant was already observed by Spino *et al.* [6] and is generally attributed to the accumulation of point defects, especially frenkel pair and / or dislocation accumulation. Some thermal healing has happened notwithstanding in the center of the pellet *via* defect recombination thermally activated.

From the broadening analysis of the same shape-fitted peaks, the evolution of the microstrain or lattice strain and the crystallite size has been evaluated as a function of the pellet radius (Figure 4).

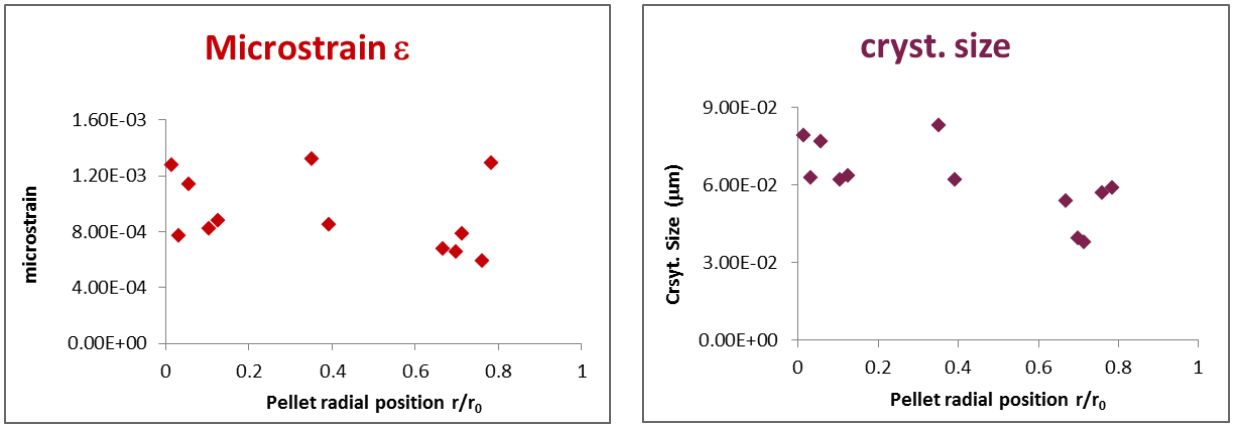

Figure 4: Evolution of the microstrain and crystallite size for selected particles along the pellet radius of the 9-cycles irradiated UO_2 fuel.

The microstrain of this 9-cycle fuel is constant along the pellet radius. This is consistent with the full re-structuring of the whole pellet that should arise as a stress release after strain accumulation. Indeed, the values we obtained varying from 8. 10^{-4} to 12. 10^{-4} are below the ones reported for

lower burn-up by Amaya *et al*. [7] and Mieszczynski *et al*. [3]. This observation supports the polygonisation process at the origin of the re-structuring, in which the stress induced by dislocation buildup is released by sub-grain formation and tangle-up of the dislocations. The crystallite size of the 9 cycle fuel is in the same order of the one found in the literature, varying from 5. 10^{-2} μm to 17. 10^{-2} μm for burn up of 60 and 72 GWd/tU respectively [7].

In the near future, the evolution of d-spacing, microstrain and crystallite sizes of the high-burn-up sample will be compared to lower burn-up samples (5 and 7 cycles) fabricated, irradiated and characterized in the same way to assess the polygonisation hypothesis. Also, temperature effect has to be more precisely defined. Temperature and burn-up value threshold for HBS formation could be then evaluated.

References

1. J. Noirot, L. Desgranges, J. Lamontagne, Detailed characterisations of high burn-up structures in oxide fuels. *J. Nucl. Mater.* **372**, 318–339 (2008).
2. C. Mieszczynski, C. Degueldre, G. Kuri, J. Bertsch, C. N. Borca, Investigation of irradiated uranium-plutonium mixed oxide fuel by synchrotron based micro X-ray diffraction. *Nucl. Mater. Sel. Artic. E-MRS 2011 Spring Meet.* **57**, 130–137 (2012).
3. C. Mieszczynski *et al.*, Irradiation effects and micro-structural changes in large grain uranium dioxide fuel investigated by micro-beam X-ray diffraction. *J. Nucl. Mater.* **444**, 274–282 (2014).
4. G. Ledergerber *et al.*, in *Proceedings of the LWR Fuel Performance Meeting/Top Fuel/WRFPM* (2010), pp. 513–524.
5. W. De Nolf, F. Vanmeert, K. Janssens, XRDUA: crystalline phase distribution maps by two-dimensional scanning and tomographic (micro) X-ray powder diffraction. *J. Appl. Crystallogr.* **47**, 1107–1117 (2014).
6. J. Spino, D. Papaioannou, Lattice parameter changes associated with the rim-structure formation in high burn-up UO2 fuels by micro X-ray diffraction. *J. Nucl. Mater.* **281**, 146–162 (2000).
7. M. Amaya, J. Nakamura, T. Fuketa, Measurements of Crystal Lattice Strain and Crystallite Size in Irradiated UO_2 Pellet by X-ray Diffractometry. *J. Nucl. Sci. Technol.* **45**, 244–250 (2008).

P20

X-ray Magnetic Circular Dichroism and Mössbauer Effect studies of the heavy fermion superconductor $NpPd_5Al_2$.

A. Hen,[1,2,3] F. Wilhelm,[1] A. Rogalev,[1] E. Colineau,[2] R. Eloirdi,[2] J.-C. Griveau,[2] N. Magnani,[2] T. Klimczuk,[2] I. Halevy,[3,4] J.-P. Sanchez,[5] A. B. Shick,[2,6] and R. Caciuffo[2]

[1]*European Synchrotron Radiation Facility (ESRF), B.P.220, F-38043 Grenoble, France*
E-mail: amir.hen@mail.huji.ac.il
[2]*European Commission, Joint Research Centre (JRC), Institute for Transuranium Elements (ITU), Postfach 2340, D-76125 Karlsruhe, Germany*
[3]*Nuclear Engineering Department, Ben Gurion University, IL84105 Beer-Sheva, Israel*
[4]*Physics Department, Nuclear Research Center Negev, P.O. Box 9001, IL84190 Beer-Sheva, Israel*
[5]*SPSMS, UMR-E CEA/UJF-Grenoble 1, INAC, FR-38054 Grenoble, France*
[6]*Institute of Physics, Academy of Sciences of the Czech Republic, Na Slovance 2, CZ-182 21 Prague, Czech Republic*

Discovered more than 100 years ago [1], and 50 years after the BCS theory [2], Superconductivity still remains one the main challenges of condensed matter physics. In particular, the existence of heavy fermions superconductivity and its coexistence or proximity with magnetic order suggests that the conventional mechanism of phonon-mediated superconductivity is inappropriate for describing these systems. Therefore, alternative mechanisms, such as spin fluctuations, should be considered for Cooper pairing. Actinide materials with their *5f* electrons are the main players in this important field, with a large number of uranium heavy fermions magnetic superconductors reported in the last three decades [3] and, more recently, transuranium unconventional superconductors: $PuCoGa_5$ [4], $PuRhGa_5$ [5], $PuCoIn_5$ [6] and $NpPd_5Al_2$ [7].

Mössbauer effect [8] has been used for more than 50 years as a unique tool for probing individual ions within compounds giving an insight on the chemical, electronic and magnetic properties of compounds. Mössbauer spectroscopy is a powerful tool in solid state physics. However, its use in superconductivity on one hand and in actinide materials on the other hand, has been limited [9] mainly due to the fact that only the 60 keV electric dipole (E1) transition of the ^{237}Np isotope is suitable for systematic investigations, combining reasonable experimental constraints and exploitable output parameters [10]. X-ray Magnetic Circular Dichroism (XMCD) is yet another unique characteristic tool, not only element specific, but also shell specific and capable of discerning contributions of the different elements in a complex sample. In the last 25 years, XMCD has become one of the leading experimental tools in materials research with many applications in solid state physics, and, successful implementation on actinides and their compounds [11-13]

A recent novel model for superconductivity [14] has predicted a possible temperature-dependence with an extremum of the charge density in several superconductors, which may apply to the heavy fermion Np-based superconductor $NpPd_5Al_2$ (T_c = 4.9K and γ= 200 mJ mole^{-1} K^{-2}). This is a unique opportunity to utilize the excellent Mössbauer resonance of the ^{237}Np nucleus and its high resolution spectroscopy ($1.986\cdot10^{-7}$ eV for 1 mm/s in ^{237}Np) to test the proposed model. The Isomer-Shift (δ_{IS}), measured by the ^{237}Np Mössbauer spectroscopy is directly related to the charge density at the Np nuclei [15], hence, the Mössbauer spectroscopy allows a direct testing of the suggested model by measuring the temperature dependence of the δ_{IS} in $NpPd_5Al_2$. First Mössbauer measurements suggested just a small increase in both δ_{IS} and the quadrupolar interaction parameter e^2qQ below the critical temperature T_c, indicating that both the electronic density at the Np nuclei and the electric field gradient due to the *5f* electrons are affected by the formation of Cooper pairs but with no extremum around T_c [16]. A second set of measurements, taken with higher temperature resolution revealed a small minimum, however, the measured values fell within the experimental errors and no

clear conclusion could have been drawn [17]. A new set of measurements, which were taken with an improved spectrometer supports the previously observed minimum of the δ_{IS} around T_c, however the effect remained very subtle.

In an attempt to confirm these findings, we have performed XANES and XMCD measurements at the $M_{4,5}$-edges of Np above and below the superconducting transition temperature in order to evaluate the relative change in charge density as a function of temperature. From XANES measurements we did not observe sizable changes, neither in the number of *5f* holes nor in the branching ratio at the superconducting transition. From the XMCD measurements, we were able to determine the *5f* spin and orbital magnetic moment of Np. The results of XANES, XMCD and Mössbauer spectroscopy will be reported and compared along with their connection to the theoretical prediction.

Acknowledgements
The high purity Np metals required for the fabrication of the compound were made available through a loan agreement between Lawrence Livermore National Laboratory and ITU, in the frame of a collaboration involving LLNL, Los Alamos National Laboratory and the US Department of Energy.

References

[1] H. K. Onnes, Commun. Phys. Lab. Univ. Leiden 120b, 122b, 124c (1911).
[2] J. Bardeen et al. , Phys. Rev. **108**, 1175 (1957).
[3] P.S. Riseborough et al, in: Superconductivity, Springer, Ed. K.H. Bennemann and J.B. Ketterson pp 1031-1154 (2008).
[4] J.L. Sarrao et al., Nature **420**, 297 (2002).
[5] F. Wastin et al., J. Phys.: Condens. Matter **15**, S2279 (2003).
[6] E.D. Bauer et al., J. Phys.: Condens. Matter **24**, 052206 (2012).
[7] D. Aoki et al., J. Phys. Soc. Jpn. **76**, 063701 (2007).
[8] R.L. Mössbauer, Zeitschrift für Physik, Bd. **151**, S. 124-143 (1958).
[9] E. Colineau et al., Hyperfine Interact. **207**, 113 (2012)].
[10] G.M. Kalvius, J. Nucl. Mater. 166 (1989) 5.
[11] V. N. Antonov et al., *Phys. Rev. B* **68**, 214424 (2003);
ibid 214425, A. N. Yaresko et al., *Phys. Rev. B* **68**, 214426 (2003).
[12] F. Wilhelm et al., *Phys. Rev. B* **88**, 024424 (2013).
[13] I. Halevy, A. Hen et al., *Phys. Rev. B* **85**, 014434 (2012).
[14] R. Flint et al., Phys. Rev. B **84**, 064514 (2011).
[15] J.-P. Sanchez et al., J. Alloys Comp. 275 (1998) 154.
[16] K. Gofryk et al., Phys. Rev. **B 79**, 134525 (2009).
[17] A. Hen et al., III-O12, 43èmes Journées des Actinides, Sestri Levante, April 6-9th 2013.

P21

Syntheses and basic physical properties of ThT_2M_2 compounds (T = d-electron transition metal and M = Si or Ge)

Krzysztof Domieracki, Małgorzata Samsel–Czekała, Adam Pikul, Dariusz Kaczorowski

Institute of Low Temperature and Structure Research, Polish Academy of Sciences, P Nr 1410, 50–950 Wrocław 2, Poland, e-mail: A.Pikul@int.pan.wroc.pl

Motivated by the recent discovery of exotic superconductivity in YFe_2Ge_2 [1], we have undertaken comprehensive reinvestigation of the formation and the physical properties of thorium-based 1:2:2 silicides and germanides. In this contribution, we report on the syntheses and the crystal structures of the ThT_2M_2 compounds, where T is a d-electron transition metal and M = Si or Ge, supplemented by the results of low-temperature physical properties measurements. We show that most of the members of the family crystallize in a tetragonal $ThCr_2Si_2$-type structure (space group I4/mmm), while only a few of them form with a closely-related tetragonal $CaBe_2Ge_2$-type unit cell (space group P4/nmm). The physical properties studies have revealed that superconductivity is observed (if any) only in the phases possesing the latter structure type, in line with the findings reported in the literature [2].

References

[1] Zou et al., Phys. Stat. Sol. RRL **8**, 928 (2014).
[2] Shelton et al., Solid State Commun. **52**, 797 (1984).

List of participants

Name	Laboratory	Country	Email
Antonios BANOS	University of Bristol	UNITED KINGDOM	ab13306@bristol.ac.uk
Francois BOTTIN	CEA - DAM Ile-de-France	FRANCE	francois.bottin@cea.fr
Johann BOUCHET	CEA - Bruyeres Le Chatel	FRANCE	johann.bouchet@cea.fr
Daniel BRAITHWAITE	CEA Grenoble - INAC	FRANCE	daniel.braithwaite@cea.fr
Jean-Pascal BRISON	CEA Grenoble - INAC	FRANCE	jean-pascal.brison@cea.fr
Nicolas BRISSET	CNRS UMR 6226 - Universite Rennes 1	FRANCE	nicolas.brisset@univ-rennes1.fr
Thomas BUSLAPS	ESRF	FRANCE	buslaps@esrf.fr
Roberto G.M. CACIUFFO	European Commission	GERMANY	roberto.caciuffo@ec.europa.eu
Karel CARVA	Charles University	CZECH REPUBLIC	karel.carva@mff.cuni.cz
Melanie CHOLLET	Paul Scherrer Institute	SWITZERLAND	melanie.chollet@psi.ch
Eric COLINEAU	European Commission	GERMANY	eric.colineau@ec.europa.eu
James DARNBROUGH	University of Bristol	UNITED KINGDOM	j.e.darnbrough@bris.ac.uk
Stefan DOEGE	Institute Laue-Langevin	FRANCE	doeges@ill.fr
Krzysztof DOMIERACKI	Polish Academy of Sciences	POLAND	k.domieracki@int.pan.wroc.pl
Boris DORADO	CEA DAM Ile de France	FRANCE	boris.dorado@cea.fr
Andrea DZUBINSKA	Presov University, FHNS	SLOVAKIA	adzubinska@gmail.com
Rachel ELOIRDI	European Commission	GERMANY	rachel.eloirdi@ec.europa.eu
Enrica EPIFANO	CEA Cadarache	FRANCE	enrica.epifano@cea.fr
Henry FISCHER	Institut Laue-Langevin - ILL	FRANCE	fischer@ill.fr
Giovanna FRAGNETO	Institut Laue-Langevin - ILL	FRANCE	fragneto@ill.fr
Izaak FRYER-KANSSEN	Lancaster Univeristy	UNITED KINGDOM	i.fryer-kanssen@lancaster.ac.uk
Gaston GARBARINO	ESRF	FRANCE	gaston.garbarino@esrf.fr
David GEESON	AWE Aldermaston	UNITED KINGDOM	David.Geeson@awe.co.uk
Platon GKAMALETSOS	Technical University of Denmark	DENMARK	plagka@dtu.dk

Name	Laboratory	Country	Email
Francois GUILLOU	ESRF	FRANCE	francois.guillou@esrf.fr
Roman GUMENIUK	MPI	GERMANY	gumeniuk@cpfs.mpg.de
Itzhak HALEVY	Nuclear Research Center - Negev	ISRAEL	halevy.itzhak.dr@gmail.com
Nicholas HARKER	ESRF	FRANCE	nicholas.harker@esrf.fr
Ladislav HAVELA	Charles University	CZECH REPUBLIC	havela@mag.mff.cuni.cz
Amir HEN	ESRF	FRANCE	amir.hen@esrf.fr
Arno HIESS	European Spallation Source ESS AB	SWEDEN	arno.hiess@esss.se
Jean-Michel HILTBRUNNER	Institut de Chimie de Clermont Ferrand (ICCF)	FRANCE	jean-michel.hiltbrunner@areva.com
Igor IZOSIMOV	Joint Institute for Nuclear Research	RUSSIA	izig@mail.ru
Christopher JONES	University of Bristol	UNITED KINGDOM	cj0810@bristol.ac.uk
Laurent JOUFFRET	Institut de Chimie de Clermont Ferrand (ICCF)	FRANCE	laurent.jouffret@univ-bpclermont.fr
Dariusz KACZOROWSKI	Polish Academy of Science	POLAND	D.Kaczorowski@int.pan.wroc.pl
Milan KLICPERA	Charles University	CZECH REPUBLIC	mi.klicpera@seznam.cz
Agnieszka KOZUB	Institute of Physics ASCR	CZECH REPUBLIC	akozub@mif.pg.gda.pl
Kristina KVASHNINA	ESRF	FRANCE	kristina.kvashnina@esrf.fr
Gerard LANDER	European Commission	GERMANY	lander@ill.fr
Eleanor LAWRENCE BRIGHT	University of Bristol	UNITED KINGDOM	e.lawrencebright@bristol.ac.uk
Dominik LEGUT	IT4Innovations Center	CZECH REPUBLIC	dominik.legut@vsb.cz
Haiyan LU	Institute of Materials	CHINA	hyluphys@163.com
Olivia LYNES	Lancaster University	UNITED KINGDOM	o.lynes@lancaster.ac.uk
Maria Do Sameiro MARQUES FERNANDES	Paul Scherrer Institute	SWITZERLAND	maria.marques@psi.ch
Silvie MASKOVA	Charles University	CZECH REPUBLIC	maskova@mag.mff.cuni.cz
Vladimir MATVIENKO	RFNC-VNIITF	RUSSIA	mvn1969@mail.ru

Name	Laboratory	Country	Email
Natalia MAYORDOMO	CIEMAT	SPAIN	natalia.mayordomo@ ciemat.es
Arianna MINELLI	ESRF	FRANCE	arianna.minelli@esrf.fr
Alexey MIRMELSTEIN	RFNC-VNIITF	RUSSIA	mirmelstein@mail.ru
Luigi PAOLASINI	ESRF	FRANCE	paolasin@esrf.fr
Mathieu PASTUREL	CNRS UMR 6226 - Universite Rennes 1	FRANCE	mathieu.pasturel@univ-rennes1.fr
Antonio PEREIRA GONCALVES	Instituto Superior Tecnico	PORTUGAL	apg@ctn.ist.utl.pt
Ivan PIDCHENKO	Karlsruhe Institute of Technology	GERMANY	ivan.pidchenko@gmail.com
Adam PIKUL	Polish Academy of Sciences	POLAND	A.Pikul@int.pan.wroc.pl
Ruizhi QIU	Institute of Materials	CHINA	qiuruizhi@itp.ac.cn
Florent REAL	CNRS UMR 8523 - USTL	FRANCE	florent.real@univ-lille1.fr
Marian REIFFERS	Presov University, FHNS	SLOVAKIA	reiffers@unipo.sk
Sophie RENNIE	University of Bristol	UNITED KINGDOM	sr9716@bristol.ac.uk
Andrei ROGALEV	ESRF	FRANCE	rogalev@esrf.fr
Claudine ROMERO	ESRF	FRANCE	claudine.romero@esrf.fr
Malgorzata SAMSEL-CZEKALA	Polish Academy of Sciences	POLAND	m.samsel@int.pan.wroc.pl
Jean-Pierre SANCHEZ	CEA Grenoble - INAC	FRANCE	jean-pierre.sanchez1@ orange.fr
Andreas SCHEINOST	ROBL - CRG	FRANCE	scheinost@esrf.fr
Victor SHAPOVALOV	ESRF	FRANCE	victor.shapovalov@esrf.fr
Samuel SHAW	University of Manchester	UNITED KINGDOM	sam.shaw@manchester.ac.uk
Lei SHI	CEA Cadarache	FRANCE	lei.shi@cea.fr
Alexander SHIK	Czech Academy of Science	CZECH REPUBLIC	shick@fzu.cz
Anna SMITH	Delft University of Technology	NETHERLANDS	a.l.smith@tudelft.nl
Ross SPRINGELL	University of Bristol	UNITED KINGDOM	ross.springell@gmail.com
William G. STIRLING	ESRF	FRANCE	stirling@ill.fr

Name	Laboratory	Country	Email
Joseph SUTCLIFFE	University of Bristol	UNITED KINGDOM	joseph.sutcliffe@bristol.ac.uk
Laurence TELLIER	Institut Laue-Langevin - ILL	FRANCE	tellier@ill.fr
Evgeniya TERESHINA	Institute of Physics ASCR	CZECH REPUBLIC	teresh@fzu.cz
Olivier TOUGAIT	CNRS UMR 6226 - Universite Rennes 1	FRANCE	tougait@univ-rennes1.fr
Aleksandr TROSHEV	RFNC-VNIITF	RUSSIA	atroshev@mail.ru
Valerie VALLET	CNRS	FRANCE	valerie.vallet@univ-lille1.fr
Ikuo WAKAIDA	Japan Atomic Energu Agency	JAPAN	wakaida.ikuo@jaea.go.jp
Andrew Colin WALTERS	Diamond Light Source Ltd	UNITED KINGDOM	andrew.walters@diamond.ac.uk
Xin WANG	Institute of Materials	CHINA	wangxin@alum.imr.ac.cn
Fabrice WILHELM	ESRF	FRANCE	wilhelm@esrf.fr
Eyal YAHEL	Nuclear Research Center - Negev	ISRAEL	eyalyahel@gmail.com
Yu YANG	IAPCM	CHINA	yang_yu@iapcm.ac.cn
Ping ZHANG	IAPCM	CHINA	zhang_ping@iapcm.ac.cn

Index


HOTEL
LE
PIC BLANC
★★★

11th SPCA			46th JdA		
Monday 14 March	**Tuesday 15 March**	**Wednesday 16 March**	**Thursday 17 March**	**Friday 18 March**	**Saturday 19 March**
8:15 Welcome **W. G. Stirling**					
08:30-10:00 **L. Paolasini**	08:30-09:30 **D. Braithwaite**	09:00-10:00 **R. Springell**	08:30-08:50 Welcome 08:50-10:30 **A. B. Shick** **N. Brisset** **D. Braithwaite** **M. Samsel-Czekala** **D. Kaczorowski**	08:30-10:30 **E. Yahel** **N. Harker** **J.-M. Hiltbrunner** **C. P. Jones** **K. Kvashnina** **A. Walters**	08:30-10:30 **P. Zhang** **L. Paolasini** **B. Dorado** **S. Rennie** **F. Bottin** **H. Lu**
10:00-10:30 Coffee break	09:30-10:30 **H. Fischer**	10:00-11:00 **S. Shaw**	10:30-11:00 Coffee break	10:30-11:00 Coffee break	10:30-11:00 Coffee break
10:30-12:00 **A. Rogalev** **& F. Wilhelm**	10:30-11:00 Coffee break	11:00-11:30 Coffee break	11:00-13:00 **I. Fryer-Kanssen** **Y. Yang** **M. Reiffers** **I. Izosimov** **I. Wakaida** **D. Legut**	11:00-13:00 **N. Mayordomo** **F. Réal** **M. Marques Fernandes** **V. Vallet** **O. Tougait**	11:00-12:00 **L. Shi** **E. Epifano** **M. Chollet** 12:00-13:00 **Summary** **&** **Perspectives**
12:00-13:15 LUNCH ESRF/ILL restaurant	11:00-12:00 **A. Scheinost**	11:30-12:30 **R. Caciuffo**	13:00-14:30 LUNCH	13:00-14:30 LUNCH	13:00-14:30 LUNCH
13:15-15:00 **Tour** **(1/2 ILL - 1/2 ESRF)**	12:00-13:15 LUNCH ESRF/ILL restaurant	12:30-13:30 LUNCH ESRF/ILL restaurant	14:30-16:30 **R. Qiu** **G. H. Lander** **L. Havela** **J. E. Darnbrough** **X. Wang** **A. Mirmelstein**	14:30-18:00 **Social Afternoon**	14:30-18:00 **Social Afternoon**
15:00-16:00 **K. Kvashnina**	13:15-15:00 **Tour** **(1/2 ILL - 1/2 ESRF)**	14:00 Bus to 46th JdA	16:30-17:00 Tea break		
16:00-16:30 Tea break	15:00-16:00 **G. Garbarino**		17:00-18:40 **J.-P. Brison** **E. Colineau** **R. Eloirdi** **F. Wilhelm**		
16:30-17:30 **G. Fragneto**	16:00-16:30 Tea break			18:00-19:00 **Poster Session**	
17:30-18:30 **A. Hiess**	16:30-17:30 **T. Buslaps**				
19:00-20:30 DINNER onsite	17:30-18:30 **G. Lander**	18:00-22:00 JdA registration and Welcome Reception	19:00-20:30 DINNER	19:00-20:30 DINNER	19:00-22:00 CONFERENCE DINNER
	19:00-21:30 WINE & CHEESE ESRF/ILL cafeteria			20:30-21:30 **Poster Session**	